

**UCLA**

**UCLA Electronic Theses and Dissertations**

**Title**

Variation of Pore Metrics in Metal-Organic Frameworks for Enhanced Storage and Catalytic Applications

**Permalink**

<https://escholarship.org/uc/item/8w38j7sp>

**Author**

Brown, Jonathan Ward

**Publication Date**

2015

Peer reviewed|Thesis/dissertation

UNIVERSITY OF CALIFORNIA

Los Angeles

**Variation of Pore Metrics in Metal-Organic  
Frameworks for Enhanced Storage and Catalytic  
Applications**

A dissertation submitted in partial satisfaction

of the requirements for the degree

Doctor of Philosophy in Chemistry

by

**Jonathan Ward Brown**

2015



© Copyright by  
Jonathan Ward Brown  
2015

ABSTRACT OF THE DISSERTATION

**Variation of Pore Metrics in Metal-Organic Frameworks for Enhanced Storage and Catalytic Applications**

by

**Jonathan Ward Brown**

Doctor of Philosophy in Chemistry

University of California, Los Angeles, 2015

Professor Louis-Serge Bouchard, Chair

With the principles of reticular chemistry, metal-organic frameworks (MOFs) with enhanced storage and catalytic capabilities have been prepared. This dissertation presents the synthesis of azo-IRMOF-74-III for controllable release of cargo molecules as well as the catalytic testing of MOF-525-Mn and an isorecticular series of MOFs based on the MOF-5 framework. The variation of pore metrics in these frameworks show the versatility of reticular chemistry and their application in catalytic reactions.

First, an azobenzene containing MOF-74 analogue was prepared by incorporating the azobenzene moiety into the organic linker used to prepare MOF-74. Cargo molecules were trapped inside the structure based on size constraints and controllably released via modulation of UV irradiation to induce a trans to cis isomerization on the organic linker. The variation in the linker length shows that specific cargo molecules can be trapped by changing the size of the one-dimensional pore in reticular frameworks.

In addition to changing pore size, density of catalytic sites inside a pore was investigated through the isorecticular synthesis of a series of MOFs, modeled after

MOF-5 but containing various amounts of 2-aminoterephthalic acid. These amine groups were post-synthetically modified to contain catalytically active Pd sites and heterogeneous Heck coupling was performed. An inverse relationship was observed between the amount of framework metalation and reaction yield and selectivity. This is attributed to pore blocking from post-synthetic modification at higher metal loadings.

Finally, a manganese porphyrin containing MOF, MOF-525-Mn, was synthesized and its activity tested through the epoxidation of alkenes using molecular oxygen. High catalytic activity was observed for all alkenes and this is the first instance of MOF epoxidation using molecular oxygen, a ubiquitous industrial oxidant. Another MOF containing the same catalytically active porphyrin but in a different topology, MOF-545-Mn, was also tested for catalytic activity to determine the effect of MOF topology on heterogeneous catalysis.

The variation of pore metrics is demonstrated through each chapter and shows how powerful and useful reticular chemistry is through variation of structural elements for specific uses. While catalytic MOFs are in their infancy, the future is bright for catalytically active MOFs to come to the forefront of chemical industry.

The dissertation of Jonathan Ward Brown is approved.

Xiangfeng Duan

Paula L. Diaconescu

Dante Simonetti

Louis-Serge Bouchard, Committee Chair

University of California, Los Angeles

2015

For my parents, Nelson and Debbie Brown

# TABLE OF CONTENTS

<b>1</b>	<b>Introduction . . . . .</b>	<b>1</b>
<b>2</b>	<b>Photophysical pore control and trapping of cargo in azo-IRMOF-74-III . . . . .</b>	<b>9</b>
2.1	Experimental Detail . . . . .	12
2.2	Results and Discussion . . . . .	15
2.3	Conclusions . . . . .	23
2.4	Supporting Information . . . . .	24
2.4.1	Materials and general procedures . . . . .	24
2.4.2	Synthesis of azo-IRMOF-74-III . . . . .	24
2.4.3	Structure resolution of azo-IRMOF-74-III from Powder X-Ray Diffractrometry (PXRD) . . . . .	24
2.4.4	Crystal structure modeling . . . . .	25
2.4.5	Comparison of Propidium Iodide to azo-IRMOF-74-III aperture . . . . .	28
2.4.6	Thermal gravimetric analysis of azo-IRMOF-74-III . . . . .	30
2.4.7	Solid-state $^{13}\text{C}$ CP/MAS nuclear magnetic resonance spectroscopy. . . . .	30
2.4.8	Fluorescence monitoring of wavelength specific release experiment . . . . .	32
2.4.9	UV-vis determination of loading efficiency of propidium iodide into azo-IRMOF-74-III . . . . .	33

2.4.10	UV-vis spectra of an ethanol solution of the azo-linker and magnesium chloride . . . . .	34
<b>3</b>	<b>Heterogeneous Heck Coupling in Multivariate Metal-Organic Frameworks for Enhanced Selectivity . . . . .</b>	<b>35</b>
3.1	Supporting Information . . . . .	41
3.1.1	Materials and general procedures . . . . .	41
3.1.2	Synthesis of all $\text{Zn}_4\text{O}(\text{BDC-NH}_2)_n(\text{BDC})_{(3-n)}$ ( $n = 3, 2.4, 1.8, 1.2, 0.9, 0.75, 0.6, 0.3$ and $0.15$ ) samples . . . . .	41
3.1.3	Metalation of $\text{Zn}_4\text{O}(\text{BDC-NH}_2)_n(\text{BDC})_{(3-n)}$ ( $n = 3, 2.4, 1.8, 1.2, 0.9, 0.75, 0.6, 0.3$ and $0.15$ ) . . . . .	44
3.1.4	Powder X-ray diffraction data . . . . .	46
3.1.5	Gas adsorption at 77 K . . . . .	47
3.1.6	$^{15}\text{N}$ and $^1\text{H}$ solution NMR spectra and ICP-AES analysis . . . . .	49
3.1.7	Solid-state $^{15}\text{N}$ CP/MAS NMR spectroscopy . . . . .	60
3.1.8	Optical microscopy . . . . .	63
3.1.9	Catalytic Testing: Experimental Setup . . . . .	63
3.1.10	Determination of Catalytic Activity: GC-MS . . . . .	64
3.1.11	Catalyst Results and Recycling Experiments . . . . .	69
3.1.12	Catalyst control and poisoning results . . . . .	71
3.1.13	ICP-AES of reaction product . . . . .	75
3.1.14	X-ray photoelectron spectroscopy (XPS) . . . . .	75
<b>4</b>	<b>Epoxidation of Alkenes with Molecular Oxygen Catalyzed by a Manganese Porphyrin-Based Metal-Organic Framework . . . . .</b>	<b>77</b>
4.1	Supporting Information . . . . .	86

4.1.1	Materials and general procedures . . . . .	86
4.1.2	Synthetic procedure for MOF-525-Mn . . . . .	86
4.1.3	Powder X-ray diffraction data . . . . .	86
4.1.4	Gas adsorption at 77 K . . . . .	87
4.1.5	ICP-AES results for metalation . . . . .	87
4.1.6	UV-Vis spectroscopy . . . . .	88
4.1.7	X-ray photoelectron spectroscopy (XPS) . . . . .	90
4.1.8	Catalytic Testing: Experimental Setup . . . . .	90
4.1.9	Determination of Catalytic Activity: GC-MS . . . . .	90
4.1.10	Catalyst control results . . . . .	96
4.1.11	Elemental analysis and ICP-AES of reaction product . . .	97
4.1.12	Reaction Rate Kinetics and Fitting of GC-MS data in MAT- LAB . . . . .	98
<b>5</b>	<b>Conclusions and Future Directions . . . . .</b>	<b>100</b>
5.1	Attempts to Immobilize Crabtree's Catalyst in IRMOF-74-III for Heterogeneous NMR Signal Enhancement . . . . .	101
5.2	The Effect of Topologically Distinct MOFs on Alkene Epoxidation Yield . . . . .	105
5.3	Bimetallic Porphyrin-based MOFs for Propylene Epoxidation . . .	109
5.4	Effect of MOF Topology on Oligomerization of Propylene . . . . .	111
5.5	Cascade Catalysis in MOF Systems . . . . .	114
	<b>References . . . . .</b>	<b>116</b>



## LIST OF FIGURES

1.1	A) Synthesis of prototypical MOF-5. B) Reaction of carboxylate linker and metal salt yields different SBUs and by extension different topologies . . . . .	3
1.2	Synthetic representation of idealized azo-IRMOF-74-III. The yellow balls represent largest free volume in idealized azo-IRMOF-74-III when azobenzene functionalities are entirely in cis conformation.	5
1.3	Structure of $\text{Zn}_4\text{O}(\text{BDC-NH}_2)_n(\text{BDC})_{(3-n)}$ ( $n = 3, 2.4, 1.8, 1.2, 0.9, 0.75, 0.6, 0.3$ and $0.15$ ) and chart showing catalytic conversion for the synthesis of resveratrol trimethyl ether as a function of framework metalation. . . . .	6
1.4	Epoxidation of styrene using MOF-525-Mn and molecular oxygen.	7
2.1	Synthesis of Azobenzene-Functionalized MOF Struts . . . . .	11
2.2	Viewing idealized azo-IRMOF-74-III down the c-axis displays one-dimensional pores and azobenzene functional groups projecting into the pores. The yellow and orange balls represent pore aperture in idealized azo-IRMOF-74-III, when the azobenzene functional groups are in trans and cis conformation, respectively. . . . .	13
2.3	Indexed experimental (red) and refined (black) PXRD patterns of azo-IRMOF-74-III after Rietveld refinement. The difference plot is indicated in green. Blue ticks indicate the positions of Bragg reflections. . . . .	14
2.4	Nitrogen isotherm of azo-IRMOF-74-III carried out on activated sample at 77 K. Adsorption and desorption branches are represented by solid and open circles respectively. A surface area of 2410 $\text{m}^2/\text{g}$ was calculated from Brunauer-Emmett-Teller (BET) analysis.	15

2.5	Pre- (black trace) and post- (cyan trace) irradiation UV-vis absorption spectra of <b>5</b> (a) and cis (red trace) and trans (blue trace) spectra calculated from Equation 7.1 using relative cis and trans peak integrations from $^1\text{H}$ NMR spectra (b). Spectra for (a) (20 M in DMSO) were irradiated with 15 mW of light from a 377 nm diode laser for 30 minutes. . . . .	16
2.6	Comparison of absorption spectra of <b>5</b> (solid trace) with the absorption spectrum of azo-IRMOF-74-III (dotted trace). The transition seen at 315 nm shifts to 337 nm upon coordination of the linker with the magnesium atoms is attributed to a $\pi$ - $\pi^*$ transition involving the C=O functionalities on the outer rings. . . . .	18
2.7	Change in absorbance of the azobenzene linker with (a) 377 nm irradiation followed by (b) 457 nm irradiation. Each trace represents 15 seconds of irradiation. The first trace is plotted in black for clarity.	19
2.8	(a) Typical release of propidium dye from azo-IRMOF-74-III as a function of time, (b) detailed view of the baseline and start of laser irradiation (marked by the sharp line), and (c) an on/off trial, where the excitation beam was temporarily removed mid-release. The dye continues to diffuse away from the MOF, but the rate of release is drastically reduced. . . . .	21
2.9	Propidium Iodide size without counterion in three dimensions. . .	28
2.10	Space filling model of non-idealized azo-IRMOF-74-III. . . . .	28
2.11	Dye diffusion with different orientation through MOF structure. .	29
2.12	Thermal gravimetric analysis of azo-IRMOF-74-III while heating sample from 20-800°C. . . . .	30
2.13	$^{13}\text{C}$ NMR of azobenzene link and azo-IRMOF-74-III in the solid state. . . . .	31

2.14	Time-dependent concentration of propidium iodide released from azo-IRMOF-74-III under sequential exposure to 647 nm and 403 nm lasers. . . . .	32
2.15	UV-vis spectra of a propidium iodide solution before and after loading a 100 mg sample of azo-IRMOF-74-III for three days. The 6% difference in concentration corresponds to the amount of dye uptaken by the particles. . . . .	33
2.16	Absorption spectra of a 0.2 mM azo-linker and 0.8 mM $\text{MgCl}_2$ solution in ethanol before and after exposure to 377 nm light for 15 s intervals. An isosbestic point at 403 nm is observed. . . . .	34
3.1	Schematic representation of post-synthetic modification and metalation of $\text{Zn}_4\text{O}(\text{BDC-NH}_2)_3$ , X and Y are Cl and $\text{CH}_3\text{CN}$ , respectively.	37
3.2	MOF performance as catalyst in a Heck coupling reaction. (A) Reaction of 4-vinylanisole and 1-bromo-3,5-methoxybenzene catalysed by MOF to form resveratrol trimethyl ether (B) Catalytic conversion as a function of increasing metalation. Indicated specific surface areas ( $\text{m}^2/\text{g}$ ) were calculated from Brunauer-Emmett-Teller (BET) analysis of isotherms, as shown in the SI section. (C) Selectivity of Heck coupling for each MOF. As metalation decreases, we see higher selectivity for the trans isomer until a plateau is reached below $n = 0.6$ (trans : cis product ratio approximately 106 : 1). .	39
3.3	PXRD analysis for $\text{Zn}_4\text{O}(\text{BDC-NH}_2)_3\text{-Pd}$ indicate crystallinity is maintained after multiple catalytic cycles. PXRD spectra of calculated $\text{Zn}_4\text{O}(\text{BDC-NH}_2)_3$ (black), activated $\text{Zn}_4\text{O}(\text{BDC-NH}_2)_3\text{-Pd}$ (blue), $\text{Zn}_4\text{O}(\text{BDC-NH}_2)_3\text{-Pd}$ after one catalytic cycle (red), after five catalytic cycles (green), and after ten catalytic cycles (purple). Dark blue ticks indicate the positions of Bragg reflections. . . . .	40

3.4	PXRD patterns of unfunctionalized (A, D), imine functionalized (B, E), and metalated frameworks (C, F). . . . .	46
3.5	Nitrogen isotherms of all $\text{Zn}_4\text{O}(\text{BDC-NH}_2)_n(\text{BDC})_{(3-n)}$ -Pd samples. . . . .	48
3.6	Percentage and degree of functionalization of amino-BDC in MTV-MOFs . . . . .	49
3.7	Digestion NMR spectrum of $\text{Zn}_4\text{O}(\text{BDC-NH}_2)_{0.15}(\text{BDC})_{2.85}$ . . . . .	50
3.8	Digestion NMR spectrum of $\text{Zn}_4\text{O}(\text{BDC-NH}_2)_{0.3}(\text{BDC})_{2.7}$ . . . . .	50
3.9	Digestion NMR spectrum of $\text{Zn}_4\text{O}(\text{BDC-NH}_2)_{0.6}(\text{BDC})_{2.4}$ . . . . .	51
3.10	Digestion NMR spectrum of $\text{Zn}_4\text{O}(\text{BDC-NH}_2)_{0.75}(\text{BDC})_{2.25}$ . . . . .	51
3.11	Digestion NMR spectrum of $\text{Zn}_4\text{O}(\text{BDC-NH}_2)_{0.9}(\text{BDC})_{2.1}$ . . . . .	52
3.12	Digestion NMR spectrum of $\text{Zn}_4\text{O}(\text{BDC-NH}_2)_{1.2}(\text{BDC})_{1.8}$ . . . . .	52
3.13	Digestion NMR spectrum of $\text{Zn}_4\text{O}(\text{BDC-NH}_2)_{1.8}(\text{BDC})_{1.2}$ . . . . .	53
3.14	Digestion NMR spectrum of $\text{Zn}_4\text{O}(\text{BDC-NH}_2)_{2.4}(\text{BDC})_{0.6}$ . . . . .	53
3.15	Digestion NMR spectrum of $\text{Zn}_4\text{O}(\text{BDC-NH}_2)_3$ . . . . .	54
3.16	Digestion NMR spectrum of $\text{Zn}_4\text{O}(\text{BDC-NH}_2)_{0.15}(\text{BDC})_{2.85}$ -Pd. . . . .	55
3.17	Digestion NMR spectrum of $\text{Zn}_4\text{O}(\text{BDC-NH}_2)_{0.3}(\text{BDC})_{2.7}$ -Pd. . . . .	55
3.18	Digestion NMR spectrum of $\text{Zn}_4\text{O}(\text{BDC-NH}_2)_{0.6}(\text{BDC})_{2.4}$ -Pd. . . . .	56
3.19	Digestion NMR spectrum of $\text{Zn}_4\text{O}(\text{BDC-NH}_2)_{0.75}(\text{BDC})_{2.25}$ -Pd. . . . .	56
3.20	Digestion NMR spectrum of $\text{Zn}_4\text{O}(\text{BDC-NH}_2)_{0.9}(\text{BDC})_{2.1}$ -Pd. . . . .	57
3.21	Digestion NMR spectrum of $\text{Zn}_4\text{O}(\text{BDC-NH}_2)_{1.2}(\text{BDC})_{1.8}$ -Pd. . . . .	57
3.22	Digestion NMR spectrum of $\text{Zn}_4\text{O}(\text{BDC-NH}_2)_{1.8}(\text{BDC})_{1.2}$ -Pd. . . . .	58
3.23	Digestion NMR spectrum of $\text{Zn}_4\text{O}(\text{BDC-NH}_2)_{2.4}(\text{BDC})_{0.6}$ -Pd. . . . .	58
3.24	Digestion NMR spectrum of $\text{Zn}_4\text{O}(\text{BDC-NH}_2)_3$ -Pd. . . . .	59
3.25	$^{15}\text{N}$ solution spectrum of a model compound $\text{Pd}(\text{C}_{13}\text{H}_{10}\text{NO})_2$ used to confirm the metal binding in the solid state NMR experiments. . . . .	60

3.26	$^{15}\text{N}$ CP/MAS NMR spectrum of $\text{Zn}_4\text{O}(\text{BDC-NH}_2)_{1.2}(\text{BDC})_{1.8}$ . . .	61
3.27	$^{15}\text{N}$ CP/MAS NMR spectrum of $\text{Zn}_4\text{O}(\text{BDC-NH}_2)_{1.2}(\text{BDC})_{1.8}$ -Imine. . .	62
3.28	$^{15}\text{N}$ CP/MAS NMR spectrum of $\text{Zn}_4\text{O}(\text{BDC-NH}_2)_{1.2}(\text{BDC})_{1.8}$ -Pd. . .	62
3.29	Optical microscopy of $\text{Zn}_4\text{O}(\text{BDC-NH}_2)_{1.2}(\text{BDC})_{1.8}$ , $\text{Zn}_4\text{O}(\text{BDC-NH}_2)_{1.2}(\text{BDC})_{1.8}$ -Imine, $\text{Zn}_4\text{O}(\text{BDC-NH}_2)_{1.2}(\text{BDC})_{1.8}$ -Pd, from left to right. . . . .	63
3.30	GC-MS of pure reactants and product for Heck coupling to establish retention times. . . . .	65
3.31	GC-MS of resveratrol trimethyl ether before U.V. irradiation (294 nm for 60 min). . . . .	66
3.32	GC-MS of resveratrol trimethyl ether after U.V. irradiation. . . .	67
3.33	GC-MS of Heck coupling reaction to synthesize resveratrol trimethyl ether. . . . .	68
3.34	Yield and selectivity for MOF and homogeneous catalysts. . . . .	69
3.35	Average yield and trans to cis ratio of product for two MOFs after 10 catalytic cycles. . . . .	70
3.36	Reaction yields of Heck coupling after omission of MOF or using unmetalated MOF. All measurements have an uncertainty of 1 % . . . . .	72
3.37	Reaction progress shows no change after $\text{Hg}(0)$ is added to reaction mixture. . . . .	73
3.38	Reaction progress shows loss of catalytic activity after $\text{PPh}_3$ is added to reaction mixture. . . . .	74
3.39	XPS Spectra of $\text{Zn}_4\text{O}(\text{BDC-NH}_2)_3$ -Pd and $\text{Zn}_4\text{O}(\text{BDC-NH}_2)_{1.2}(\text{BDC})_{1.8}$ -Pd. . . . .	76
4.1	Epoxidation of styrene using MOF-525-Mn and molecular oxygen. . . .	78

4.2	Epoxidation of alkenes catalyzed by MOF-525-Mn and free TCPP-Mn with molecular oxygen and isobutyraldehyde. . . . .	80
4.3	Reaction pathway for the epoxidation of styrene to styrene oxide including side products. Relative yields of each species measured at equilibrium are shown as percentages. . . . .	81
4.4	Arrhenius plot of the rate constants $k'_1$ over the temperature range 293—329 K. . . . .	83
4.5	Catalytic recycling of MOF-525-Mn (a) PXRD of MOF-525-Mn after multiple catalytic runs indicates crystallinity is maintained after 6 catalytic cycles (b) XPS spectra for Mn 3s of TCPP-Mn linker and MOF-525-Mn. The data has been fit to the sum of two Gaussian, splitting is indicative of Mn(III) and does not change after catalysis (c) Product yield after multiple catalytic runs by MOF-525-Mn. High activity is maintained for all alkenes for 6 catalytic cycles. . . . .	84
4.6	PXRD patterns of as synthesized and activated MOF-525-Mn . . .	87
4.7	N <sub>2</sub> isotherm of MOF-525-Mn. . . . .	88
4.8	UV-Vis spectra of TCPP-Mn link and MOF-525-Mn show absorbance peaks at 468, 562, 596 nm, confirming the presence of manganese. . . . .	89
4.9	GC-MS spectrum of styrene epoxidation reaction. . . . .	92
4.10	GC-MS spectrum of cyclohexene epoxidation reaction. . . . .	93
4.11	GC-MS spectrum of cyclooctene epoxidation reaction. . . . .	94
4.12	GC-MS spectrum of trans-stilbene epoxidation reaction. . . . .	95
4.13	GC-MS spectrum of decene epoxidation reaction. . . . .	96
4.14	Reaction yields of epoxidation after omission of MOF-525-Mn and isobutyraldehyde or using unmetalated MOF-525 . . . . .	97

4.15	Temperature dependence of the pseudo kinetic rate constant $k_1'(T)$ of MOF-525-Mn. . . . .	99
5.1	A) Schematic representation of open and closed pore azo-IRMOF-74-III B) Epoxidation of styrene by MOF-525-Mn C) Heterogeneous Heck coupling inside a Pd containing MOF with varying number of catalytic active sites. . . . .	101
5.2	A) PSM scheme for attaching Crabtree catalyst to IRMOF-74-III B) PXRD after PSM shows loss of crystallinity in framework. . .	103
5.3	A) Synthetic scheme for NHC linker and MOP-28 analogue B) MOP-28 structure C) MOP-28 structure with yellow ball indicating free space. . . . .	104
5.4	Synthesis and catalytic testing of MOF-525-Mn, MOF-545-Mn and PCN-224 for epoxidation of long chain alkenes. . . . .	106
5.5	Epoxidation of alkenes using molecular oxygen in MOF-525-Mn and MOF-545-Mn. . . . .	107
5.6	PXRD of simulated and activated A) MOF-525-Mn B) PCN-224-Mn and C) MOF-545-Mn. . . . .	108
5.7	Schematic representation of 2D layered Cu-porphyrin MOF joined by axial Ru-porphyrins to make a bimetallic 3D MOF. . . . .	110
5.8	Synthesis and catalytic testing for oligomerization of propylene by nickel analogues of MOF-253, MOF-199 and MOF-74. . . . .	112

## LIST OF TABLES

2.1	Fractional atomic coordinates for azo-IRMOF-74-III.	
	Space Group = R 3, a = b= 46.771(46)Å, c=6.869(83)Å	
	Volume = 15028 Å <sup>3</sup> , $\alpha = \beta = 90$ , $\gamma = 120$ . . . . .	26



## ACKNOWLEDGMENTS

There are so many people who have contributed to my scientific education and this dissertation it is staggering. Without them, none of this would have been possible. First, I would like to thank Cynthia Hummel who taught me chemistry in high school and was, I believe, my first advisor. I would like to thank Professor Omar Yaghi for allowing me to work in his lab and helping me become the scientist I am today. From the Yaghi group, I would like to thank all the lab members who helped me in more ways than I can count but specifically Drs. Hiroyasu Furukawa, Will Morris, Felipe Gandara, Mohamad Hmadeh, Carolyn Knobler as well as Peter Klonowski, Rong Ye, Kyle Cordova, and Lisa Wang. From the Bouchard group I would also like to thank all the lab members but specifically Dr. Stefan Glogler, Nanette Jarenwatananon, Trenton Otto, and Jeff McCormick. In addition to all my labmates I would like to thank Boris Voloskiy, Belinda Leung, Dr. Angela Hwang, Colin Holmes, Emily Chin, John Conroy, Dr. Andrew Felder and Dr. Henry Sillin for helping keep me sane after all these years. Finally, without the support of my family I would not be in the position I am today and for that I want to acknowledge and thank, from the bottom of my heart, Andrew, Katie, Nelson and Debbie Brown.

## VITA

- 2009                      University of Southern California  
B.A. in Chemistry
- Publications          Photophysical Pore Control in an Azobenzene-Containing Metal-Organic Framework, Jonathan W. Brown, Bryana L. Henderson, Matthew D. Kiesz, Adam C. Whalley, William Morris, Sergio Grunder, Hexiang Deng, Hiroyasu Furukawa, Jeffrey I. Zink, J. Fraser Stoddart, Omar M. Yaghi. *Chemical Science*, **2013**, 4, 2858-2864.
- Effects of Multivariate Linker Substitution, Metal Binding, and Reactor Conditions on the Catalytic Activity of a Pd-functionalized MOF for Olefin Hydrogenation, Trenton Otto, Nanette N. Jarenwattananon, Stefan Glogglar, Jonathan W. Brown, Arek Melkonian, Yavuz Ertas, Louis-S. Bouchard *Applied Catalysis A: General*, **2014**, 488, 248-255.
- Epoxidation of Alkenes with Molecular Oxygen Catalyzed by a Manganese Porphyrin-Based Metal-Organic Framework, Jonathan W. Brown, Quyen T. Nguyen, Trenton Otto, Nanette N. Jarenwattananon, Stefan Glogglar, Louis-S. Bouchard *Catalysis Communications*, **2014**, 59, 50-54.

Heterogeneous Heck Coupling in Multivariate MetalOrganic Frameworks for Enhanced Selectivity, Jonathan W. Brown, Nanette N. Jarenwattananon, Trenton Otto, James L. Wang, Stefan Glogler, Louis-S. Bouchard *Catalysis Communications*, **2015**, 65, 105-107.

Posters

Controllable Metalation of Multivariate Metal-Organic Frameworks with Retention of Porosity and Crystallinity. **ACS National Meeting**, Anaheim CA, March 2011.

# CHAPTER 1

## Introduction

Metal-organic frameworks (MOFs) are made by joining metal-oxide clusters with organic linker molecules to produce extended, crystalline structures [1–4]. These frameworks are structurally defined due to the rigidity of organic linkers and defined geometries of the metal oxide units. MOFs exhibit several hallmark properties including high porosity as well as chemical and thermal stability [5]. Framework integrity remains intact even after all guests have been removed from the pores and the material has been heated to 450° C [6, 7]. Due to this high framework integrity, MOFs often have very high permanent porosity [8, 9]. In addition to these hallmark properties, the ability to vary functional groups on the organic links combined with the choice of metal-oxide secondary building units (SBUs) gives MOFs a large degree of flexibility in terms of topology, pore size and geometry. Due to their large surface area and variable pore environment, MOFs have been receiving much attention for applications such as heterogeneous catalysis [10, 11], gas storage/separation and purification [12, 13], high-sensitivity sensors [14, 15], porous electrodes [16, 17] and magnets [18–21], size-, shape- and enantio-selective chromatography [22–24], and drug storage/delivery [25, 26].

Reticular chemistry provides the blueprint for building MOFs. This means that we can predict the structural outcome of a chemical reaction. Reticular chemistry is defined as, “Logical construction of chemical structures that are held together by strong bonds” [1]. This enables us to predetermine the topology and structure and, utilizing rational design, synthesize MOFs with a desired topology,

periodicity and functionality for a desired structural outcome. One of the most ubiquitous MOFs, MOF-5 [ $\text{Zn}_4\text{O}(\text{C}_8\text{H}_4\text{O}_4)_3$ ] [27] is constructed by connecting  $\text{Zn}_4\text{O}(\text{CO}_2)_6$  with the linear molecule 1,4-benzenedicarboxylic acid as the linker bridging two metal oxide units to form a primitive cubic structure, Figure 1.1. Utilizing the principles of reticular chemistry, this MOF can be expanded or altered to include different functionalities [28]. We know that reactions of carboxylic acids and selected transition metals under specific conditions form octahedral ( $\text{M}_4\text{O}(\text{CO}_2)_6$ ), square planar ( $\text{M}_2(\text{CO}_2)_4$ ), or triangular ( $\text{M}_3(\text{CO}_2)_6$ ) SBUs [29] (Figure 1.1B), and these provide points of extension. The directionality (linear, trigonal, etc.) of the linker that will connect the points of extension helps determine the overall framework topology and allows us to predict the overall structure. Thus, utilizing a  $\text{Zn}_4\text{O}(\text{CO}_2)_6$  cluster that has six points of extension, and connecting those points with 1,4-benzenedicarboxylate links, a cubic topology is obtained where an octahedral  $\text{Zn}_4\text{O}(\text{CO}_2)_6$  cluster is connected by six 1,4-benzenedicarboxylate links that can be shared by six different  $\text{Zn}_4\text{O}(\text{CO}_2)_6$  clusters, thereby forming an extended simple cubic network.

Varying the link type or altering functional groups on the link can drastically change the pore metrics of the structure without disturbing the underlying topology. The multivariate (MTV) principle showed that different organic linkers of similar size and geometry can be used in the synthesis of one MOF, allowing for the fine tuning within MOF structures. Furthermore, the MTV principle has allowed for links incompatible with MOF synthesis to be incorporated in smaller quantities into a MOF framework [30]. Some links were unable to form crystalline structures via solvothermal synthesis either due to steric constraints or unfavorable electronic properties, yet the MTV principle circumvented these problems by mixing multiple types of linkers in a single pot and producing MOFs with several functionalities in the final framework [31]. This opened up new possibilities for frameworks in terms of both functionalities inherent to the MOF and its result-

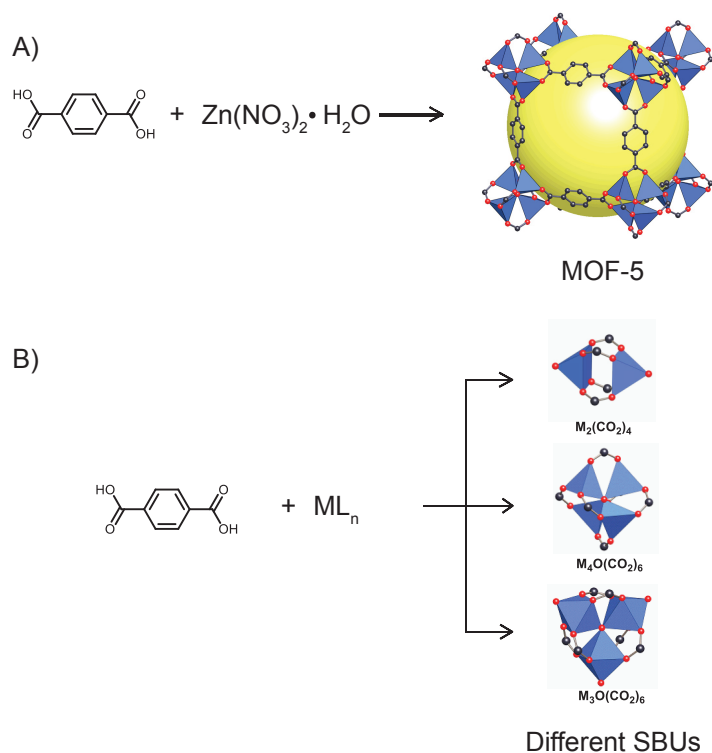


Figure 1.1: A) Synthesis of prototypical MOF-5. B) Reaction of carboxylate linker and metal salt yields different SBUs and by extension different topologies

ing properties, such as introduction of hydrophobic or hydrophilic links, Lewis acid and base pairs, and alteration of pore geometry through steric hindrance [11, 32–35].

Another tool for MOF chemists, postsynthetic modification (PSM), allows for introduction of functionalities into a MOF following solvothermal synthesis [36]. PSM works by first forming a framework then performing chemical reactions on that structure to insert a desired functional group or catalytically active site [37–40]. This allows one to take an unreactive framework with specific properties or desired topology and modifies it to take on new and interesting properties such as improved gas sorption, catalytic activity, and more robust physical properties [41].

Both the MTV principle and PSM have been used to introduce new function-

alities or catalytically active sites into a framework, giving the MOF field two important tools to expand the use of MOFs in heterogeneous catalysis. These tools allow for the modification of pore environment and geometry. My research described herein has used both as a way of designing higher order materials that have desirable properties such as enhanced catalytic activity and selectivity or the ability to trap and controllably release molecules of interest.

The objective of this dissertation is to explore catalytic applications of MOFs by altering pore metrics such as geometry and environment. Some of the most common catalytic reactions that have been seen in MOFs are hydrogenation, oxidation, and epoxidations [42–45]. While MOF catalysis is relatively new, the field is rapidly expanding as more and more catalytically active structures are synthesized [46,47]. One major advantage of using a MOF in heterogeneous catalysis is the ability to vary the organic link in the framework. This opens up many possibilities for lining the pore cavity with catalytic active species and also allows us to control the density of active sites. Both PSM and the MTV principle have been crucial in the development of MOFs as catalysts as many MOFs were viewed as both unreactive and unsuitable for catalysis, either due to instability of the framework or lack of catalytically active sites. While the field of MOF catalysis is growing, many papers report catalytic yields that are unoptimized. My research has sought to fill this gap by optimizing reaction yield and selectivity for a number of different heterogeneous catalyst. Another interesting development in MOF catalysis is the rise of chemically and thermally stable SBUs that are rapidly expanding the types of reactions available for MOFs [48–50]. The synthesis of MOFs utilizing a Zr (the UiO-66 series), Cr or Fe (MIL-101 series), or Al (MIL-53 series) backbone have helped in terms increase the number of frameworks which are chemically or thermally stable enough to withstand rigorous catalytic conditions [51–53].

One of the first goals in my research was to determine whether a molecule

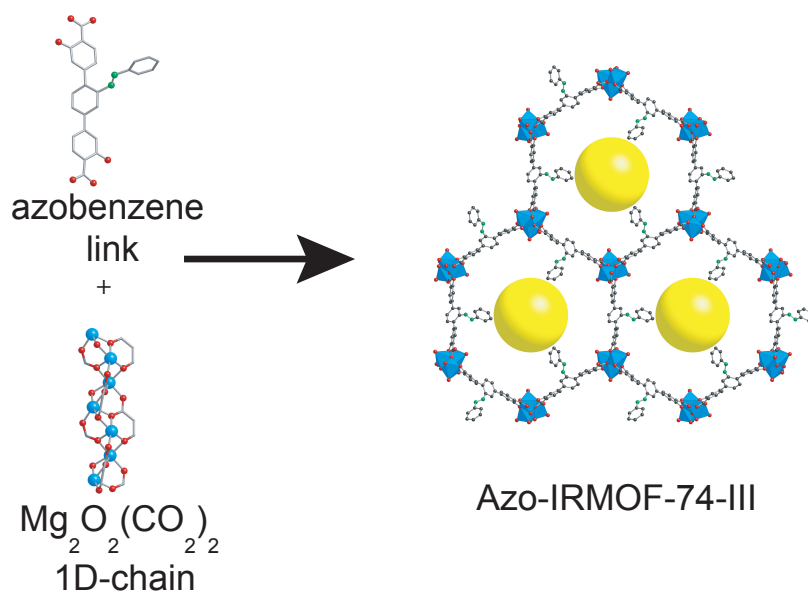


Figure 1.2: Synthetic representation of idealized azo-IRMOF-74-III. The yellow balls represent largest free volume in idealized azo-IRMOF-74-III when azobenzene functionalities are entirely in cis conformation.

could be trapped within a MOF pore without being chemically bonded to the framework. In chapter 2 this idea is explored by the synthesis of a MOF-74 derivative that contains azobenzene units (Figure 1.2).

By choosing a framework with one-dimensional pore structure, we can use the azobenzene functionality, projecting toward the middle of the pore to capture and controllably release cargo molecules based on size exclusion. While the framework itself is not catalytically active, this MOF shows proof of principle that molecules of interest can be controllably captured based on size selection, introduced into the pores of a structure and then controllably released. This idea could be easily extended to trapping molecules based on properties other than simply size constraints and allows for greater control over pore geometry and environment in known MOFs.



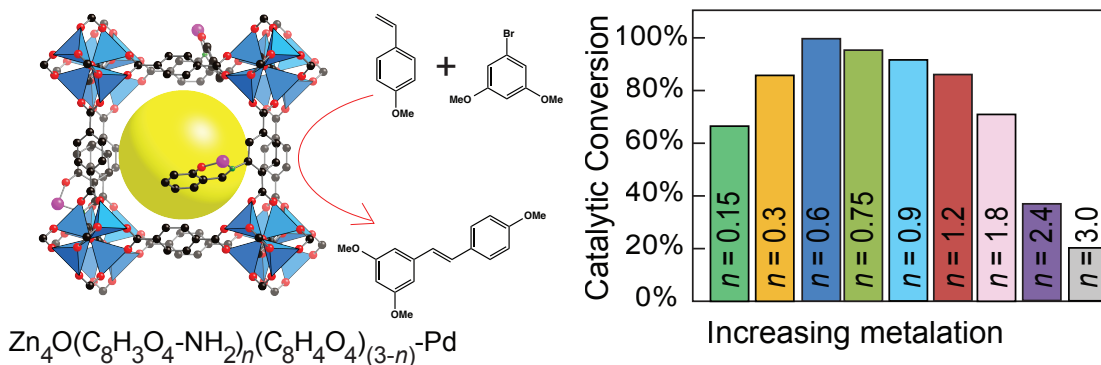


Figure 1.3: Structure of  $\text{Zn}_4\text{O}(\text{BDC-NH}_2)_n(\text{BDC})_{(3-n)}$  ( $n = 3, 2.4, 1.8, 1.2, 0.9, 0.75, 0.6, 0.3$  and  $0.15$ ) and chart showing catalytic conversion for the synthesis of resveratrol trimethyl ether as a function of framework metalation.

Another major component of catalytically active MOFs is synthesis of the catalytic sites themselves. While many MOFs are capable of having active sites introduced into the framework, there have been relatively few examples where functional catalysts are embedded into known frameworks. Chapter 3 discusses the synthesis and optimization of a catalytically active MOF, which contains catalytically active Pd sites. Using both the MTV principle and PSM to optimize the density of catalytically active sites, we show that metalation and porosity of a framework (Figure 1.3) play an integral role in finding optimal catalytic conversion for Heck coupling to synthesize resveratrol trimethyl ether, a pharmaceutically relevant precursor.

Surprisingly, the highest density of catalytic sites in our framework does not show the highest catalytic conversion. In fact, during our Heck coupling experiments we found that the lowest amount of catalytic loading provided both the highest catalytic yield and selectivity. We have seen that by varying the percentages of available functionality within a structure and by extension the number

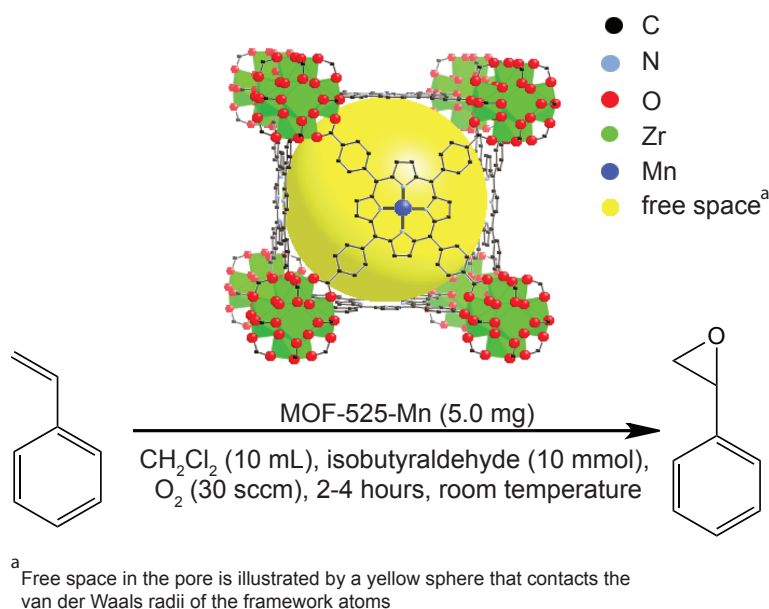


Figure 1.4: Epoxidation of styrene using MOF-525-Mn and molecular oxygen.

and density of catalytic sites, we can test many different frameworks for catalytic activity and find optimal metal loading and activity for a given framework. This seemingly counterintuitive finding that fewer catalytic sites give higher catalytic conversion brings up interesting questions in regards to framework design as well as the density of catalytically active sites and provides valuable background into future research in rational design of new MOFs for catalytic applications.

In chapter 4, the idea of exploring new methods of catalysis is shown by way of a Zr-MOF containing a manganese metalloporphyrin for the epoxidation of alkenes (Figure 1.4).

There have been other published accounts of MOFs that catalyze epoxidations but none that use molecular oxygen as the oxygen source [24, 45, 54]. Molecular oxygen is regularly used in industry due to it being inexpensive, less corrosive and easier to handle on a large scale than liquid peroxides [55]. The epoxidation of alkenes is particularly attractive to industrial chemical companies as propylene

and ethylene oxide are produced in millions of tons per year and are precursors for widely used chemicals [56,57]. While this study examines the epoxidation of styrene instead of propylene or ethylene epoxidation, the use of molecular oxygen makes it an interesting beginning to the search for an industrially relevant MOF catalyst. In addition to seeing high yields and good selectivity for our heterogeneous system, we also elucidated the reaction rates and activation energies associated with this particular reaction, being the first group to show this information in reference to MOF catalysis.

Finally in chapter 5, future direction for this work is explored and discussed. The framework topology in catalysis and reaction optimization plays a major role in MOF catalysis yet there have been very few studies [58] exploring this aspect of reaction engineering. In addition, epoxidation of long chain alkenes is of major interest to chemical industry and exploration of more open structures could lend itself to high yield and selectivity for industrially relevant molecules.

Catalytically active MOFs are still in their infancy, especially with respect to optimization of reactor and catalytic efficiency. Increasing control over pore metrics holds the key to synthesis of new and more efficient catalytic frameworks, expanding both the types of reactions available for MOF catalysis and the catalytic yield of existing structures. The MTV principle and PSM are indispensable tools in the design of new, higher order MOFs and subsequent control over pore metrics. As is demonstrated here, there are many factors that can affect the catalytic ability of MOFs such as framework design and selection of topology, chemical and thermal stability of MOFs and the density of active sites within the framework. Though MOF catalysis is a nascent field, its future is bright and the discovery of new frameworks with interesting catalytic applications is simply a matter of time.

## CHAPTER 2

### Photophysical pore control and trapping of cargo in azo-IRMOF-74-III

Reproduced from Ref. Chemical Science, 2013, 4, 2858-2864 with permission from the Centre National de la Recherche Scientifique (CNRS) and The Royal Society of Chemistry

MOFs are extended crystalline structures containing metal oxide units bridged by organic linkers. They are highly porous and typically exhibit large surface areas. A wide variety of organic linkers have been incorporated into MOFs, highlighting the isorecticular principle whereby the organic linkers can be changed, yet analogous structural types can be synthesized. [48, 59–61] Variation of the functional groups present in MOFs have led to applications in chemical sensing, [62, 63] gas separation, [64] gas storage, [65, 66] catalysis, [23] and drug delivery. [67] Despite the large library of MOFs reported in the literature, to date the storage and release of guest molecules has relied [68] solely on the uncontrolled diffusion of cargo into and out of the extended structures of the MOFs. Although many MOFs have been synthesized, none have demonstrated on-command release of stored guest molecules using a controllable external stimulus.

One such functionality, which demonstrated promise for the controlled release of cargo from the pores of a MOF, is the azobenzene unit. Azobenzene provides a source of reversible and photo-controllable cis/trans isomerizations [69–71]. This conformational switching results in significant changes in the length of the molecule (9 Å in the trans form to 5.5 Å in the cis form) [72] and, as a result,

this photoswitchable system has been incorporated into a variety of rigid materials including films and nano-structures. [73–86] Furthermore, the integration of azobenzene units has been employed recently in the one-dimensional (1-D) pores of mesoporous silica nanoparticles where it was demonstrated [87, 88] that the on-command release of cargo molecules from the pores is possible. Photoactive linkers have been incorporated into MOFs and shown interesting adsorption and storage properties that have been directly linked to the photoactivity of those frameworks [89–93]. Recently two MOFs were synthesized [94, 95] containing azobenzene units, however, the nature of the pores in these MOFs produced steric restrictions that limited photoswitching applications. We chose to incorporate the photoswitch into a MOF-74 based structure, to combat these steric limitations. Due to a unique binding motif inherent to MOF-74, the inorganic clusters and organic struts form linear stacks producing large, non-interpenetrated 1-D hexagonal pores. This unique architecture will force the azobenzene units directly into the channels where the isomerization of each unit will have a direct impact on the aperture size of a single 1-D channel. Therefore, the photodynamic switching of azobenzene combined with the 1-D structure of this MOF has the potential to allow for controlled cargo delivery from a MOF.

Here, we report the synthesis and photoisomerization studies of an azobenzene-derivatized MOF, azo-IRMOF-74-III, which contains 1-D pores. In this particular MOF, the size and shape of the apertures are controlled by the conformational changes in the azobenzenes, which can be reversibly switched from trans to cis or cis to trans using UV or visible irradiation, respectively. When all of the azobenzene units are in the trans conformation the pore apertures are 8.3 Å in diameter, but upon switching to the cis conformation the size of the aperture is increased significantly (10.3 Å).

This photodynamic MOF exhibits improved photoswitching over previously synthesized azobenzene-derivatized structures because the azobenzenes are evenly

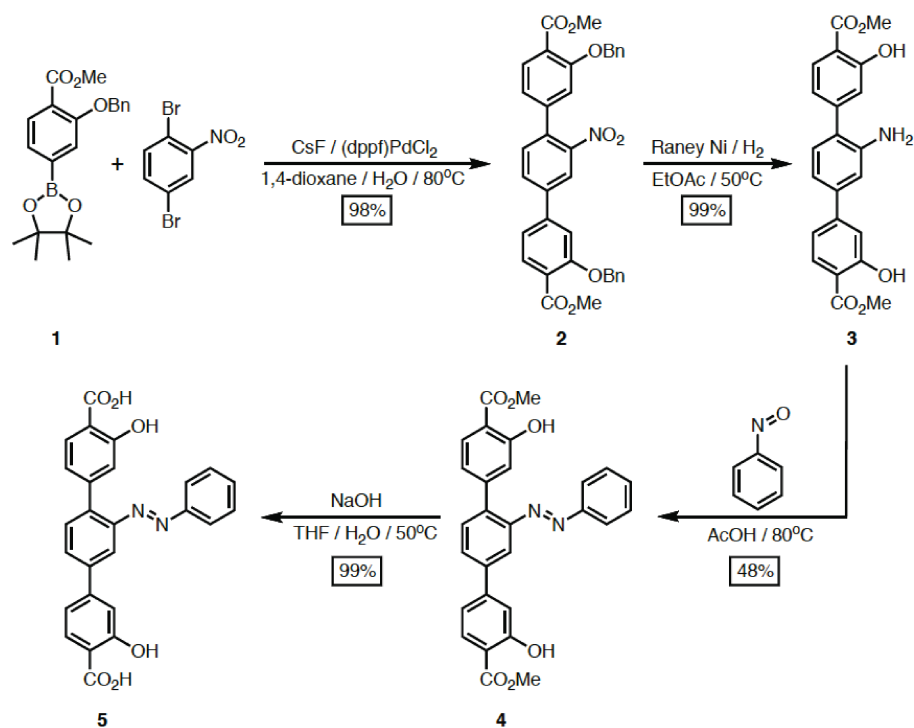


Figure 2.1: Synthesis of Azobenzene-Functionalized MOF Struts

spaced within the crystalline framework. The photophysical properties of the MOF have been investigated by  $^1\text{H}$  NMR and UV-Vis spectroscopy, and information obtained from these techniques has been used to choose a wavelength of light capable of isomerizing the azobenzene units back and forth between their two possible conformations. Spectroscopic monitoring of the release of a fluorescent guest molecule reveals that the dye remains contained in the MOF until irradiation at an appropriate wavelength. This successful containment and on-command release demonstrates the utility of self-contained photo-active switches in highly porous MOFs.

## 2.1 Experimental Detail

The synthesis of the azobenzene-functionalized linkers involves (Figure 2.1) a palladium-catalyzed Suzuki-Miyaura cross-coupling reaction between 2,5-dibromonitrobenzene and the phenylboronic ester 1 in a degassed 1,4-dioxane/H<sub>2</sub>O mixture employing PdCl<sub>2</sub>(dppf) as the catalyst and CsF as the base to yield the nitro derivative 2. Treatment of 2 with Raney Ni and H<sub>2</sub> gas in EtOAc at 50°C, serves to facilitate both the removal of the benzyl protecting groups and reduce the nitro group to produce the aniline derivative 3 in nearly quantitative yield. Subjecting 3 to excess of nitrosobenzene in acetic acid at 80°C yielded the azobenzene 4, which could be converted to the dicarboxylic acid 5, by saponification of the methyl esters.

Azo-IRMOF-74-III was synthesized by combining Mg(NO<sub>3</sub>)<sub>2</sub>·6H<sub>2</sub>O (80 mg, 0.315 mmol) and the azobenzene-functionalized linker (42.5 mg, 0.09 mmol) in a solution of N,N-dimethylformamide (DMF) (7.5 mL), EtOH (0.5 mL) and H<sub>2</sub>O (0.5 mL) for 24 h at 120°C. After 24 h, the red crystals were collected by filtration.

Powder X-ray diffraction was used for structural determination as the microcrystalline material produced from the MOF synthesis did not diffract sufficiently for single crystal elucidation. Since a higher level of characterization is achieved by producing a solvent and guest free framework, the crystals were sequentially washed with DMF (3 times, 10 mL) and methanol (3 times, 10 mL) and then evacuated on a supercritical CO<sub>2</sub> dryer over the course of 12 hours. Following this activation process, thermal gravimetric analysis (TGA) was used to confirm that all of the solvent had been removed from the pores of the framework; i.e., there was no significant weight loss up to 275°C (Figure 3.12).

Azo-IRMOF-74-III is an isorecticular expansion of MOF-74, in which helical MgOC rods are constructed from hexacoordinate Mg(II) centers. The rods are connected via azobenzene functionalized terphenylene unit 5 to produce one-

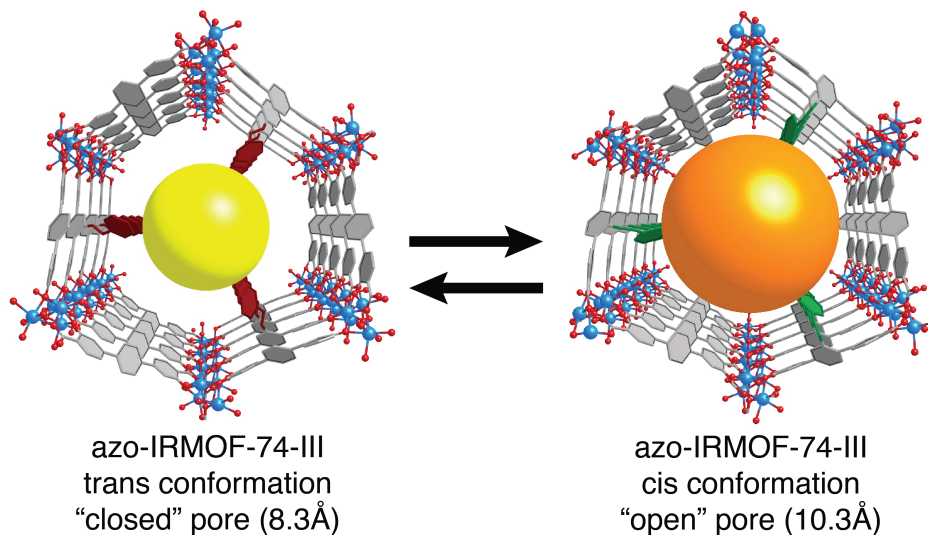


Figure 2.2: Viewing idealized azo-IRMOF-74-III down the  $c$ -axis displays one-dimensional pores and azobenzene functional groups projecting into the pores. The yellow and orange balls represent pore aperture in idealized azo-IRMOF-74-III, when the azobenzene functional groups are in trans and cis conformation, respectively.

dimensional pores, which have a diameter of 19.5 Å. This structure was simulated using the Forcite module of Materials Studio and was confirmed with the Rietveld method. Because the one-dimensional pores in azo-IRMOF-74-III are lined with azobenzene groups that project toward the middle of the pore, the size and shape of the pore aperture directly depend on the cis or trans configuration. With all azobenzene functionalities in the trans configuration the idealized pore aperture is 8.3 Å but if all functionalities are cis, the aperture is larger 10.3 Å (Figure 2.2). The PXRD pattern for azo-IRMOF-74-III was indexed on a trigonal unit cell and refined using the Rietveld method in the Reflex module of Materials Studio, yielding cell parameters  $a = 46.771(26)$  Å,  $b = 46.771(26)$  Å and  $c = 6.869(83)$  Å (residuals:  $R_p = 12.08$  %,  $R_{wp} = 17.68$  %) (Figure 2.3).

Azo-IRMOF-74-III was further characterized by cross-polarization magic-angle



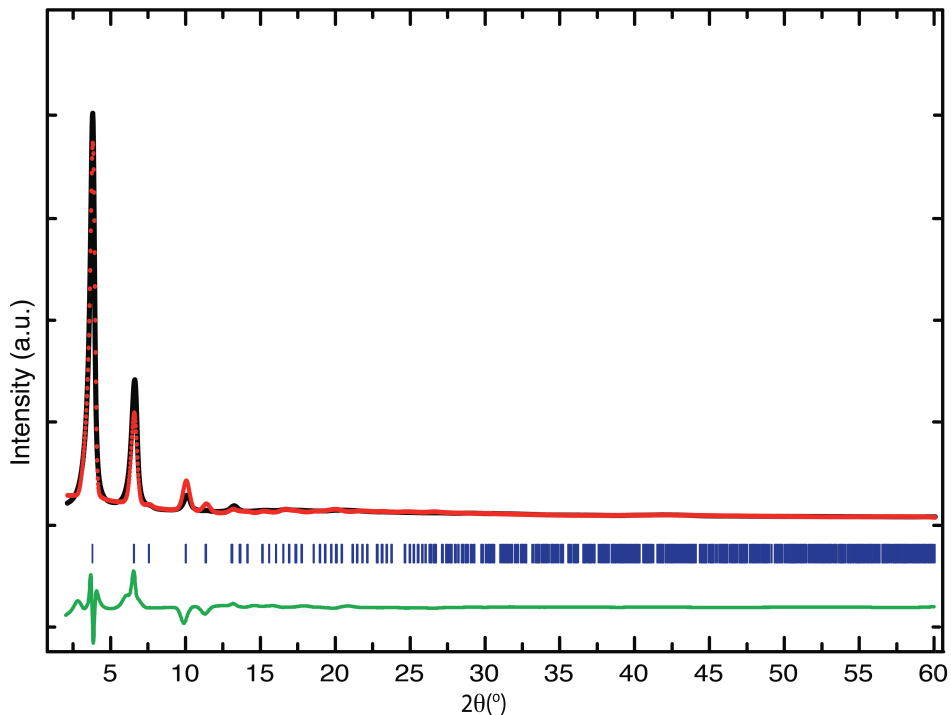


Figure 2.3: Indexed experimental (red) and refined (black) PXRD patterns of azo-IRMOF-74-III after Rietveld refinement. The difference plot is indicated in green. Blue ticks indicate the positions of Bragg reflections.

spinning (CP/MAS)  $^{13}\text{C}$  NMR spectra (Figure 2.13). From experiments on the activated material, the expected resonances at 174 ppm for the carbonyl carbon atoms and 166 and 114 ppm for the aromatic carbon atoms of incorporated **5** were found. No free **5** was observed in the MOF spectra, confirmed by a lack of peaks at 176, 160, and 108 ppm.

To confirm the porosity of azo-IRMOF-74-III,  $\text{N}_2$  isotherms at 77 K were measured on activated samples. From the Brunauer-Emmett-Teller (BET) analysis a surface area of  $2410 \text{ m}^2/\text{g}$  was calculated (Figure 2.4). To date, this is the highest recorded surface area of a MOF containing photoswitchable units.

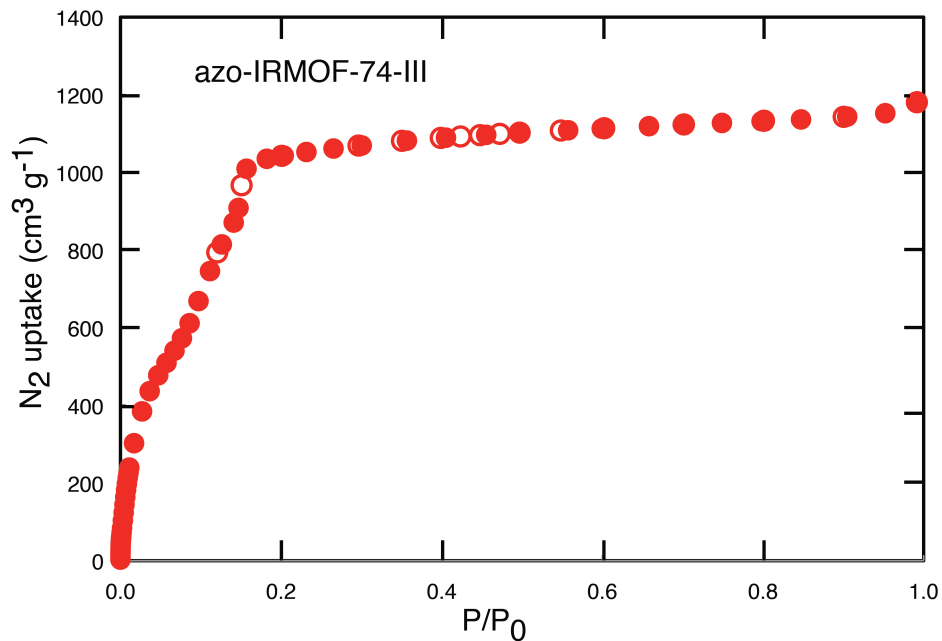


Figure 2.4: Nitrogen isotherm of azo-IRMOF-74-III carried out on activated sample at 77 K. Adsorption and desorption branches are represented by solid and open circles respectively. A surface area of 2410 m<sup>2</sup>/g was calculated from Brunauer-Emmett-Teller (BET) analysis.

## 2.2 Results and Discussion

The azobenzene functionalized linker used to synthesize azo-IRMOF-74-III exhibits the expected isomerization when exposed to UV and visible light. While previous studies of azobenzene and its derivatives have examined the photophysical properties in solution and various molecular environments, incorporation to a new platform warrants investigation of its photochromic properties. The UV-vis absorption experiments discussed in this section will thus demonstrate the performance of the azobenzene moiety within the rigid confines of a MOF.

The UV-vis absorption spectrum of non-irradiated 5 exhibits two prominent

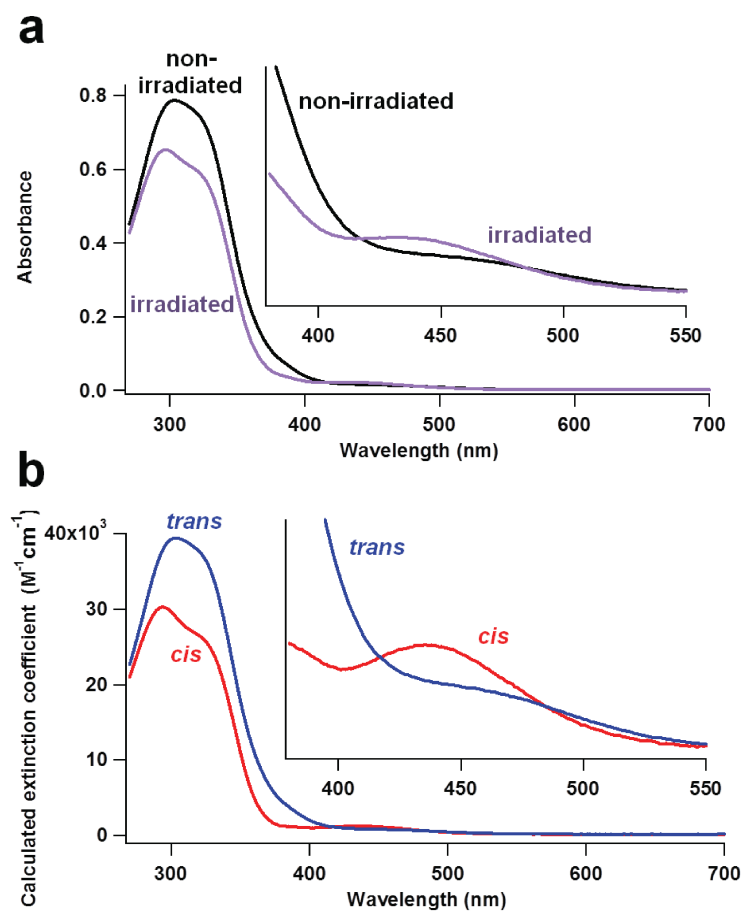


Figure 2.5: Pre- (black trace) and post- (cyan trace) irradiation UV-vis absorption spectra of 5 (a) and cis (red trace) and trans (blue trace) spectra calculated from Equation 7.1 using relative cis and trans peak integrations from  $^1H$  NMR spectra (b). Spectra for (a) (20 M in DMSO) were irradiated with 15 mW of light from a 377 nm diode laser for 30 minutes.

peaks, close in energy, in the near UV (Figure 2.5 A). Irradiation of 5 with UV light (which typically induces a trans-to-cis isomerization for azobenzene) results in dramatic changes in the absorption spectrum; i.e. the emergence of a new absorption band in the visible region. Although the photoisomerization process is evident, transitions due to the terphenyl moiety overshadow those of the azoben-

zene functional group in both the pre- and post-irradiation absorption spectra. In addition, the fact that the absorption spectra of the photostationary states are not necessarily purely those of the trans or cis isomers, respectively, further complicates analysis. Correlation of absorption spectra with  $^1\text{H}$ -NMR data elucidated spectral assignments and will be discussed in more detail below.

Relative concentration ratios of the isomers were determined with  $^1\text{H}$  NMR and combined with UV-vis spectroscopy to calculate pure cis and trans spectra. Examination of the NMR data for a pre-irradiated solution of azobenzene in DMSO (5 mM for NMR experiments, but diluted to 20 M for absorption spectra) stored in the dark at room temperature revealed the absence of the cis isomer. In contrast, the NMR spectrum of the photostationary state achieved after 30 minutes of irradiation with near-UV light (377 nm, 15 mW) contained peaks from both the cis and trans isomers. Integration of the cis and trans peaks in the irradiated solution yielded a trans/cis ratio of 0.43 (70% of trans-azobenzenes had converted to the cis configuration). Pre- and post-irradiation absorption data were correlated with the relative isomer concentrations to calculate a pure cis absorption spectrum according to the following equation:

$$\epsilon_c = \frac{\frac{1}{cl}[A_2(\frac{1}{r_2} + 1) - A_1(\frac{1}{r_1} + 1)]}{\frac{1}{r_2} - \frac{1}{r_1}} \quad (2.1)$$

where  $\epsilon_c$  is the calculated cis extinction coefficient ( $\text{M}^{-1}\text{cm}^{-1}$ ),  $c$  is the concentration of 5 (M),  $l$  is the path-length of the cuvette (cm),  $A_1$  and  $A_2$  are the pre- and post-irradiation absorbances, respectively, and  $r_1$  and  $r_2$  are the pre- and post-irradiation trans/cis isomer ratios, respectively. The resulting pure cis and trans spectra (Figure 2.5 B) reveal a clearer representation of the transitions of 5. While each of the calculated cis and trans spectra contain appreciable absorption in the UV region due to the inherent absorption from the ter-phenylene structure, the trans isomer absorbs more than the cis isomer in the UV and the cis isomer absorbs more than the trans in the visible region as expected.

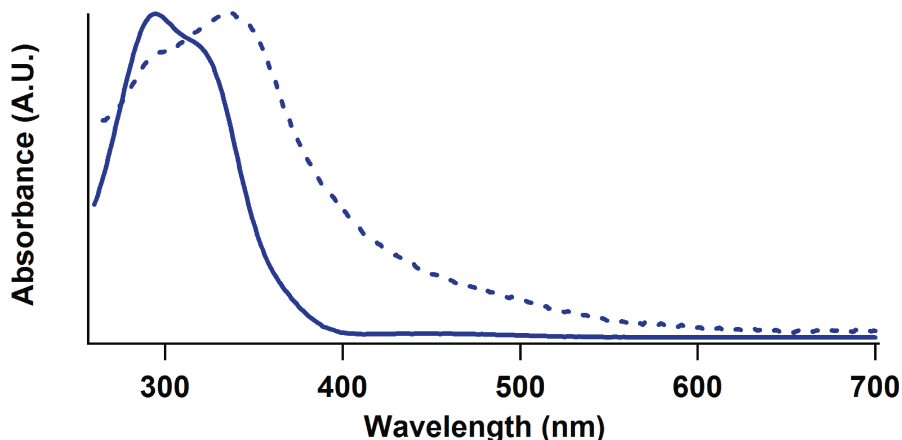


Figure 2.6: Comparison of absorption spectra of **5** (solid trace) with the absorption spectrum of azo-IRMOF-74-III (dotted trace). The transition seen at 315 nm shifts to 337 nm upon coordination of the linker with the magnesium atoms is attributed to a  $\pi$ - $\pi^*$  transition involving the C=O functionalities on the outer rings.

The UV and visible absorption peaks of the azo-benzene moiety are assigned to  $\pi$ - $\pi^*$  and  $n$ - $\pi^*$  electronic transitions, respectively. Both *cis* and *trans* calculated spectra contain a peak near 300 nm with a shoulder at 315 nm, which are attributed to the common ter-phenylene moiety. The higher energy transition near 300 nm is assigned to a  $\pi$ - $\pi^*$  transition that does not shift when the linker is coordinated to the metal atoms in the MOF. However, the shoulder at 315 nm, which is assigned to a  $\pi$ - $\pi^*$  transition involving the C=O functionalities on the outer rings, shifts to 337 nm upon coordination within the MOF structure (Figure 2.6). In the calculated spectrum of the *trans* isomer, a shoulder near 365 nm is attributed to an azobenzene  $\pi$ - $\pi^*$  transition. A weaker  $n$ - $\pi^*$  azobenzene transition is found at 438 nm in the calculated *cis* spectrum.

To characterize the photoproperties of linker **5** used in this MOF, absorption spectra were obtained as a function of irradiation time with UV and blue light.

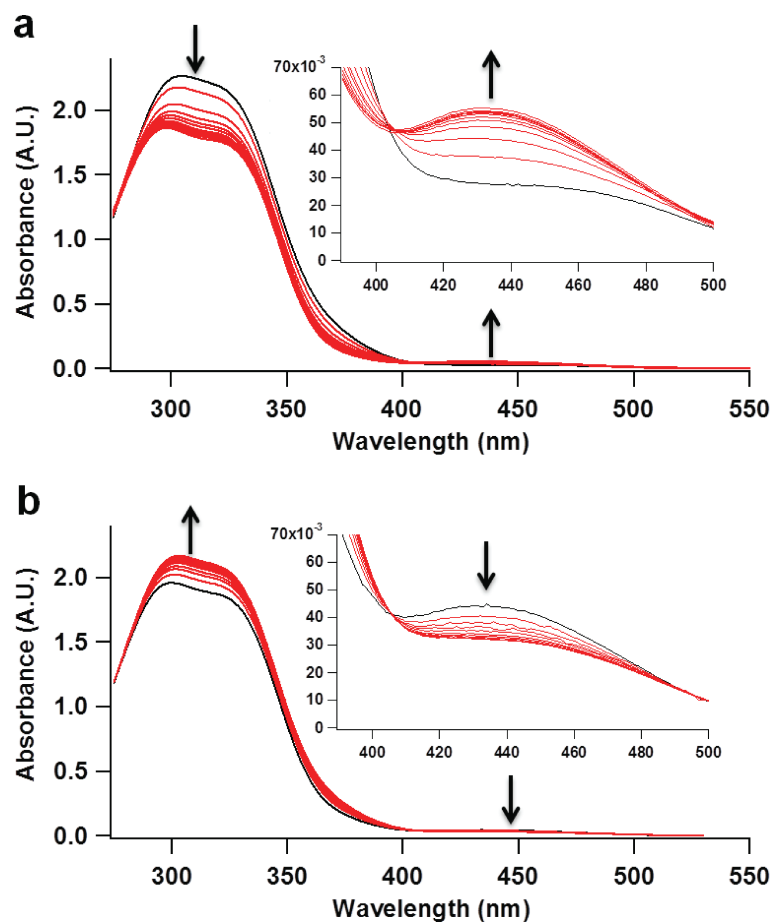


Figure 2.7: Change in absorbance of the azobenzene linker with (a) 377 nm irradiation followed by (b) 457 nm irradiation. Each trace represents 15 seconds of irradiation. The first trace is plotted in black for clarity.

A 50 M solution of **5** was exposed to 15 mW of 377 nm excitation with continuous stirring; its absorption spectra upon irradiation are plotted in Figure 2.7. Irradiation of **5** in the near UV (377 nm, Figure 2.7a) leads to excitation of the azobenzene  $\pi$ - $\pi^*$  transition seen in the calculated trans spectrum.

Since the cis isomer has no appreciable absorbance in the near-UV, the probability of trans to cis isomerization is higher than cis to trans isomerization and thus the population of the cis species increases. Additionally, competing absorp-

tion from the terphenylene portion of the linker is relatively low at 377 nm, so the incident photons are able to reach the azobenzene more efficiently. To convert the molecule back to the trans species, the azobenzene linkers were irradiated in the visible region (457 nm, Figure 2.7b) where the absorbance of the cis isomer is higher than the absorbance of the trans isomer. The absorption spectra show an increase in the  $n-\pi^*$  band at 438 nm and a decrease in the 300 nm peaks upon near-UV irradiation and the opposite trend with visible irradiation, indicating reversible isomer population changes without decomposition of the linker.

The cis and trans isomers of the linker have an isosbestic point at 402 nm that does not shift when coordinated to magnesium (Figure 2.16). Excitation wavelengths in this region can be utilized for stimulating repetitive large amplitude motions. These large amplitude motions have been used to activate the release of cargo from porous substances, [75,96] and cis-trans isomerization expels cargo in a similar way to the MOFs in this study.

To test the ability of azo-IRMOF-74-III to store and release cargo, a luminescent dye (propidium iodide, Sigma) was loaded into the hexagonal channels so that the release due to photoisomerization could be observed spectroscopically. This dye was specifically chosen because its size,  $8\text{\AA} \times 11\text{\AA} \times 16\text{\AA}$  without counterion, matches well with the pore aperture of azo-IRMOF-74-III, between 8.3 and 10.3Å depending on conformation of azobenzene linker (Figures 2.9 and 2.10). When comparing pore diameter to the dye, it can be seen that the dye cannot easily diffuse into the MOF unless the azobenzene functionalities are in the cis conformation (Figure 2.11). To load the azo-MOFs, 100 mg of particles were stirred in a 1 mM ethanolic solution of propidium iodide for 3 days under exposure to room lights. The loading process is driven by a concentration gradient and the photoisomerization afforded by room lights. UV-vis spectra of a propidium iodide solution acquired before and after loading demonstrate a loading capacity of 0.4 wt% (Figure 2.15). While minimizing light exposure the particles were washed

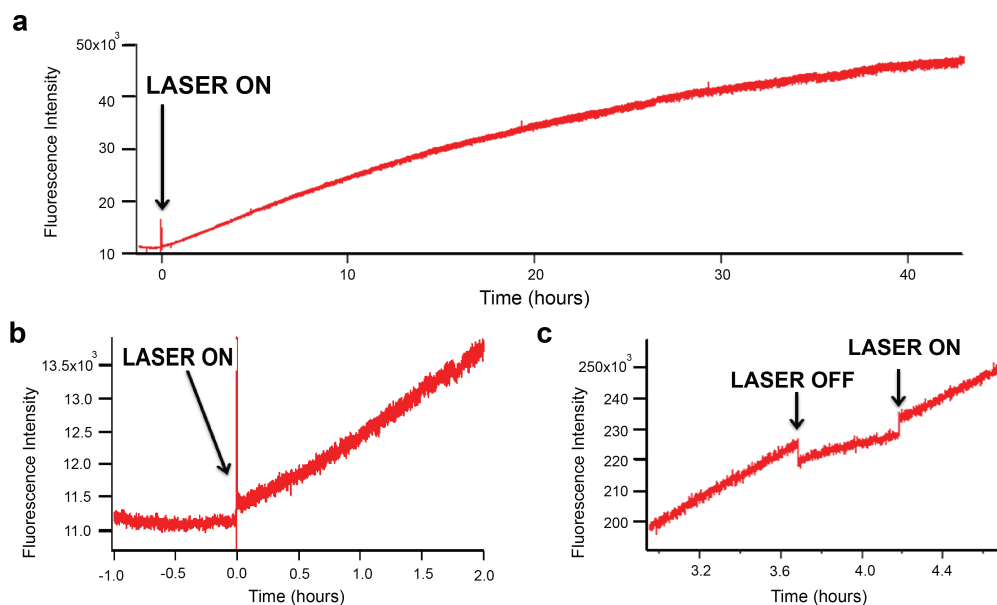


Figure 2.8: (a) Typical release of propidium dye from azo-IRMOF-74-III as a function of time, (b) detailed view of the baseline and start of laser irradiation (marked by the sharp line), and (c) an on/off trial, where the excitation beam was temporarily removed mid-release. The dye continues to diffuse away from the MOF, but the rate of release is drastically reduced.

thoroughly with ethanol to remove surface adsorbed dye. Subsequently the sample was placed in the corner of a  $2 \text{ cm} \times 1 \text{ cm}$  fluorimetric cuvette. A stir bar was placed in the opposite corner to facilitate mixing of the solution, and the cuvette was filled with spectroscopic-grade ethanol. The solution in the cuvette was stirred carefully to avoid disturbing the azo-IRMOF-74-III particles yet facilitate the diffusion of the dye. A probe beam (30 mW, 568 nm) was used to excite the propidium dye in the ethanol solution above the particles, and its fluorescence intensity was integrated and plotted as a function of time (Figure 2.8a).

As seen in Figure 2.8b, there is no increase in propidium iodide intensity prior to laser activation of the cis/trans isomerization motions in the azo-IRMOF-74-



III particles. This indicates that the azobenzene-functionalized MOF acts as an excellent container, and that no dye escapes from the MOF channels until an external light source of the proper wavelength is added.

After a baseline was established with the probe beam, a 50 mW pump beam at 408 nm (wavelength near the isosbestic<sup>1</sup> point) activated the cis-trans wagging motions and expelled the dye from the MOF channels. A clear release was observed which began to level off after 40 hours (see Figure 2.8a). This release, which took much longer than in azobenzene-derivatized MCM-41 nanoparticles, can possibly be attributed to the fact that the MOF structure’s pores are longer and narrower [97]. Additionally, the physical interactions between the guest molecules and the host metal-organic framework may be vastly different than those seen in MCM-41. To demonstrate the necessity of the pump beam near the isosbestic point of the azobenzene moiety, a 647 nm laser was employed as a pump beam in a subsequent experiment (Figure 2.14). No release was observed until the 647 nm laser was replaced with one near the isosbestic point. The release seen in Figure 2.8a can also be controlled by increasing or decreasing the incident power or removing the beam entirely; blockage of the 408 nm pump beam caused the release to slow down (see Figure 2.8c), but upon reintroduction of the beam the original release rate resumed. The sharp increases and decreases seen in the fluorescence spectra of Figure 2.8 when the laser is turned on and off, respectively, are due to effects from laser scattering. When the laser impinges upon the MOF particles, the uneven surfaces of these particles scatter the incoming laser light and increase the overall intensity counts in the spectra. When the laser is turned off, the source of scattering is removed, and an equivalent drop is seen in the spectra.

The slope of the release does not immediately go to zero, most likely due to

---

<sup>1</sup>point where the total absorbance of a sample does not change during a chemical reaction or a physical change of the sample

the following factors: (1) pores have larger apertures in the cis orientation (see Figure 2.2), allowing for some residual diffusion of cargo molecules, (2) a delay caused by diffusion of cargo from the MOF particles to the laser detection area is expected, and (3) thermal back-conversion processes continue to generate a small amount of motion in the dark. Most of these effects are short-lived, however, and discontinuation of laser irradiation will eventually reduce the rate of dye release to a negligible level. Since continuous laser irradiation is needed for efficient expulsion of the dye into solution, the pattern and duration of release can be adjusted as necessary. Azo-IRMOF-74-III, therefore, is useful in applications where longer release or stop-start release is desired [98–100].

## 2.3 Conclusions

An azobenzene-derivatized MOF has been synthesized and studied spectroscopically. Azobenzene trans and cis isomerizations of the linker molecule have been observed via NMR and absorption spectroscopy to ascertain the relative concentrations and the absorption spectra of the cis and trans species as well as the most appropriate wavelength choices for irradiation.

Irradiation at 408 nm, near the linker’s isosbestic point, causes both cis-trans and trans-cis excitations. The large amplitude motions due to these wagging motions led to an increase in dye mobility, expelling cargo from the structure on demand. The storage and release capabilities of the system could be studied with the aid of fluorescent propidium iodide, and the dye release rate was diminished when irradiation was removed. No release was observed prior to irradiation, indicating that the dye molecules are well contained.

The photo-driven azo-MOF structure, the focal point of this paper, is an improvement over recently made photoswitchable frameworks in that this structure contains only one-dimensional pores. The one-dimensional pores permit more effi-

cient storage and release of the dye, and the microporous particles allow filtration in a new size domain. Here, we have shown that the azo-MOF structure is capable of storing dye molecules and releasing them on command via a photoisomerization process. This new MOF creates unprecedented possibilities for the use of light in the realm of robust dynamics.

## 2.4 Supporting Information

### 2.4.1 Materials and general procedures

All reagents unless otherwise stated were obtained from commercial sources (Cambridge isotope laboratories, Sigma Aldrich, TCI) and were used without further purification. Yields reported were unoptimized.

### 2.4.2 Synthesis of azo-IRMOF-74-III

IRMOF-74-III azo [ $\text{Mg}_2(\text{C}_{26}\text{H}_{16}\text{O}_6\text{N}_2)$ ] was made with  $\text{Mg}(\text{NO}_3)_2 \cdot 6\text{H}_2\text{O}$  (80 mg, 0.315 mmol) and the azobenzene-functionalized linker (42.5 mg, 0.09 mmol) in a solution of N,N-dimethylformamide (DMF) (7.5 mL), EtOH (0.5 mL) and  $\text{H}_2\text{O}$  (0.5 mL) for 24 h at 120°C. After 24 h, the red crystals were collected by filtration. The crystals were washed with DMF ( $3 \times 10$  mL) over a thirty-minute period. The DMF was then replaced with MeOH ( $6 \times 30$  mL) over a two-day period. Finally, the volatile MeOH was removed by using a supercritical  $\text{CO}_2$  dryer. The crystals were then heated at 250°C under vacuum (30 mtorr) for 12 hrs.

### 2.4.3 Structure resolution of azo-IRMOF-74-III from Powder X-Ray Diffractometry (PXRD)

Powder X-ray data were collected using a Bruker D8-Discover  $\theta$ - $2\theta$  diffractometer in reflectance Bragg-Brentano geometry employing Ni filtered Cu  $K\alpha$  line focused

radiation at 1600 W (40 kV, 40 mA) power and equipped with a Vantec Line detector. Radiation was focused using parallel focusing Gobel mirrors. The system was also outfitted with an anti-scattering shield that prevents incident diffuse radiation from hitting the detector, preventing the normally large background at  $2\theta < 3$ . Samples were mounted on zero background sample holders by dropping powders from a wide-blade spatula and then leveling the sample with a razor blade. To determine the structure of IRMOF-74-III azo, crystal structure modeling was carried out, followed by Rietveld refinement.

#### **2.4.4 Crystal structure modeling**

The model for azo-IRMOF-74-III, including cell parameters and atomic positions, was generated using Materials Studio chemical structure-modeling software (Materials studio version 5.0, 2009, Accelrys Software Inc.) employing the Crystal Building module. The structure was generated using the relevant space group, the cell parameters were used as obtained, and atom positions were generated from the refined data of extended MOF-74. The constructed structure was minimized with the Forcite module using the Geometry Optimization routine with the Universal force field (UFF). The obtained model was used as input for the Rietveld refinement. Positions of atoms in the respective unit cells are listed as fractional coordinates in Table 2.1.

Table 2.1: Fractional atomic coordinates for azo-IRMOF-74-III.

Space Group = R 3, a = b= 46.771(46)Å, c=6.869(83)Å

Volume = 15028 Å<sup>3</sup>,  $\alpha = \beta = 90$ ,  $\gamma = 120$

Atom	Occupancy	X	Y	Z
H1	1	0.30123	0.14934	0.54529
H2	1	0.30397	0.19166	0.31701
H3	1	0.69359	0.87253	0.42753
H4	1	0.69335	0.91513	0.21653
H5	1	0.66974	0.91562	0.92056
H6	1	-0.01108	0.26389	0.56726
H7	1	0.66141	0.0613	1.02123
H8	1	0.01907	0.42756	0.66852
H9	1	0.99434	0.43105	0.36945
H10	1	0.99896	0.47534	1.15234
H11	1	0.38835	0.15284	1.26852
C1	1	0.32144	0.15974	0.43725
C2	1	0.32324	0.18422	0.30619
C3	1	0.68211	0.86497	0.82752
C4	1	0.6874	0.91552	0.36921
C5	1	0.68854	0.89138	0.49187
C6	1	0.68279	0.89141	0.6933
C7	1	0.67539	0.91589	0.76748
C8	1	0.93122	0.27557	0.61028
C9	1	0.93085	0.26837	0.81376
C10	1	0.95774	0.28938	0.94348
C11	1	0.70221	0.04823	0.6461

Atom	Occupancy	X	Y	Z
C12	1	0.72712	0.07259	0.77487
C13	1	0.72793	0.06653	0.97879
C14	1	0.01307	0.4278	0.82095
C15	1	1.00889	0.45444	0.89296
C16	1	1.00236	0.45509	1.09247
C17	1	1.0002	0.42969	0.21749
C18	1	1.01146	0.48142	0.75876
C19	1	0.37001	0.16151	0.28003
C20	1	0.37251	0.1865	1.14965
O1	1	0.98797	0.26319	0.42254
O2	1	0.95415	0.30335	0.5335
O3	1	0.98405	0.3162	0.88166
O4	1	0.95565	0.28113	1.12396
O5	1	0.70233	0.05569	0.4655
O6	1	0.67974	0.01894	0.70892
O7	1	0.70922	0.03722	1.05563
O8	1	0.66102	0.06141	0.16604
Mg1	1	0.98848	0.30608	0.34006
Mg2	1	0.6723	0.02583	0.25001
N	1	0.46947	0.53429	1.33391
N	1	0.43939	0.52951	1.30546
C	1	0.43532	0.54818	0.14561
C	1	0.46125	0.56422	0.00442
C	1	0.45837	0.58349	-0.14622
C	1	0.42951	0.58708	-0.15782
C	1	0.40365	0.57154	-0.01833
C	1	0.40662	0.55238	0.1328

#### 2.4.5 Comparison of Propidium Iodide to azo-IRMOF-74-III aperture

While it may be possible for a dye which is oriented perfectly perpendicular to the pore channels to escape in dark conditions, other orientations may cause blockage and dye diffusion is limited.

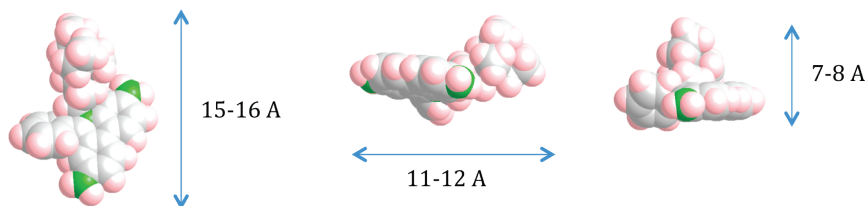


Figure 2.9: Propidium Iodide size without counterion in three dimensions.

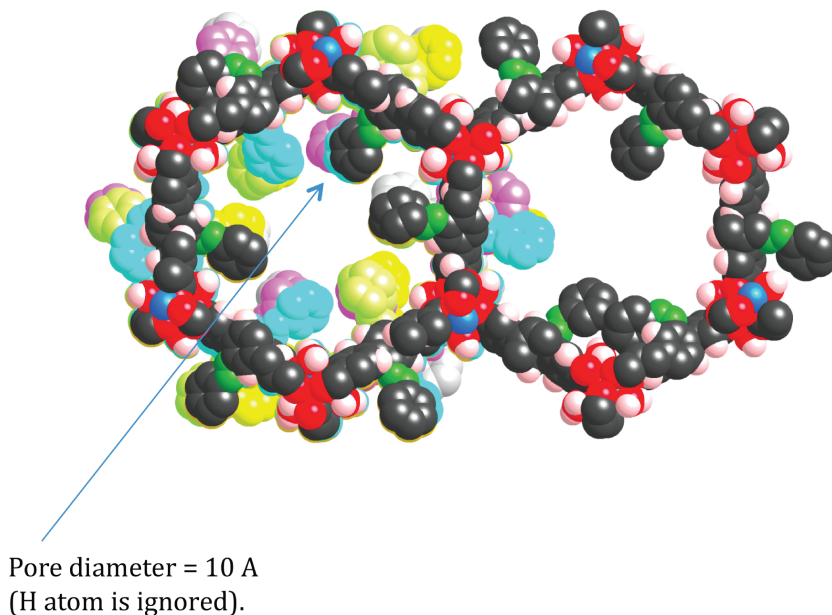


Figure 2.10: Space filling model of non-idealized azo-IRMOF-74-III.

Additionally, interactions with the pore wall and collisions with solvent and counter ions hinder motion through the pore. With photoswitching of the azo-

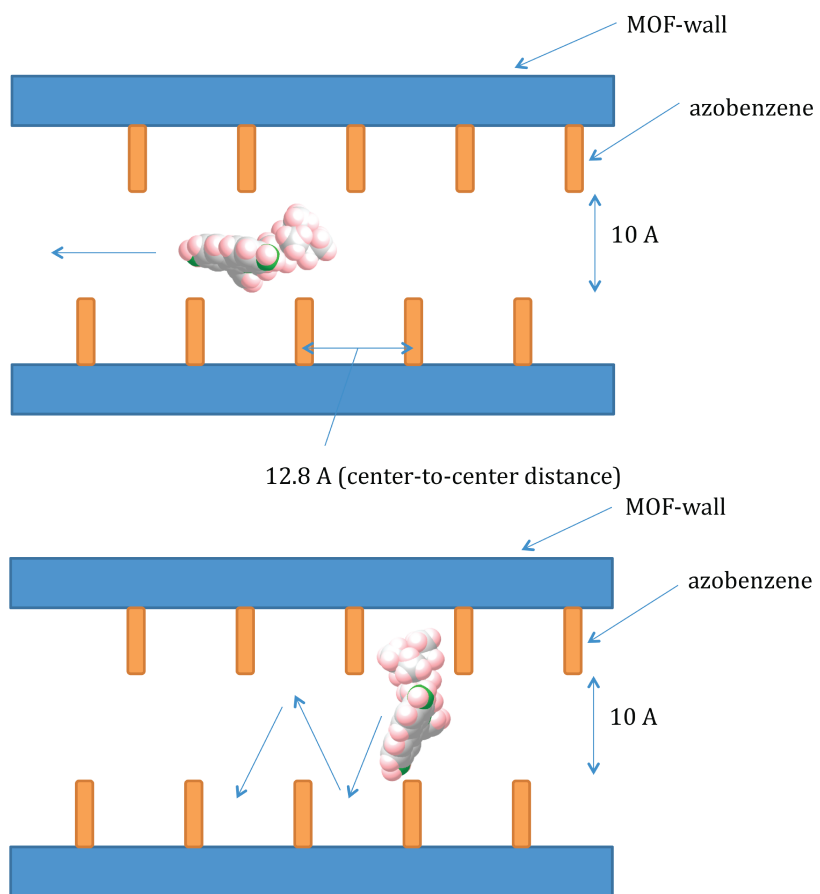


Figure 2.11: Dye diffusion with different orientation through MOF structure.



species from trans to cis, mobility is enhanced.

#### 2.4.6 Thermal gravimetric analysis of azo-IRMOF-74-III

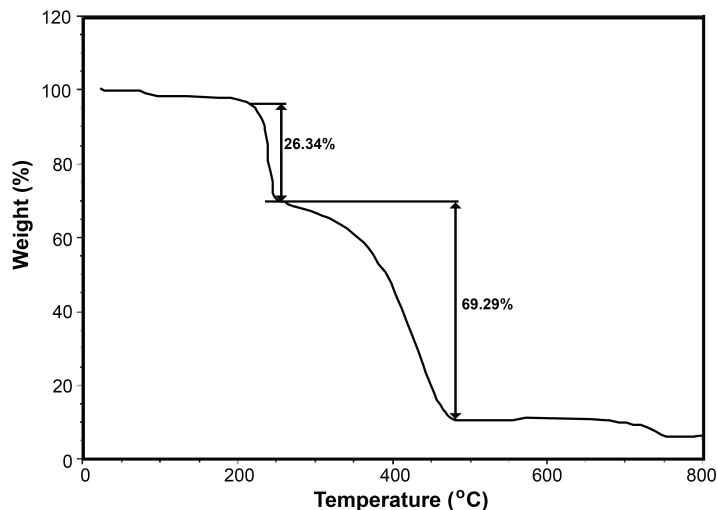


Figure 2.12: Thermal gravimetric analysis of azo-IRMOF-74-III while heating sample from 20-800°C.

#### 2.4.7 Solid-state $^{13}\text{C}$ CP/MAS nuclear magnetic resonance spectroscopy.

High resolution solid-state nuclear magnetic resonance (NMR) spectra were measured at ambient pressure on a Bruker DSX-300 spectrometer using a standard Bruker magic angle-spinning (MAS) probe with 4 mm (outside diameter) zirconia rotors. The magic angle was adjusted by maximizing the number and amplitudes of the signals of the rotational echoes observed in the  $^{79}\text{Br}$  MAS FID signal from KBr.

Cross-polarization with MAS (CP/MAS) was used to acquire  $^{13}\text{C}$  data at 75.47 MHz. The  $^1\text{H}$  and  $^{13}\text{C}$  ninety-degree pulse widths were both 4 ms. The CP contact time varied from 1.5 to 5 ms. High power two-pulse phase modulation (TPPM)

$^1\text{H}$  decoupling was applied during data acquisition. The decoupling frequency corresponded to 72 kHz. The MAS sample-spinning rate was 10 kHz. Recycle delays between scans varied between 3 and 10 s, depending upon the compound as determined by observing no apparent loss in the  $^{13}\text{C}$  signal from one scan to the next. The  $^{13}\text{C}$  chemical shifts are given relative to tetramethylsilane as zero ppm, calibrated using the methylene carbon signal of adamantane assigned to 37.77 ppm as the secondary reference.

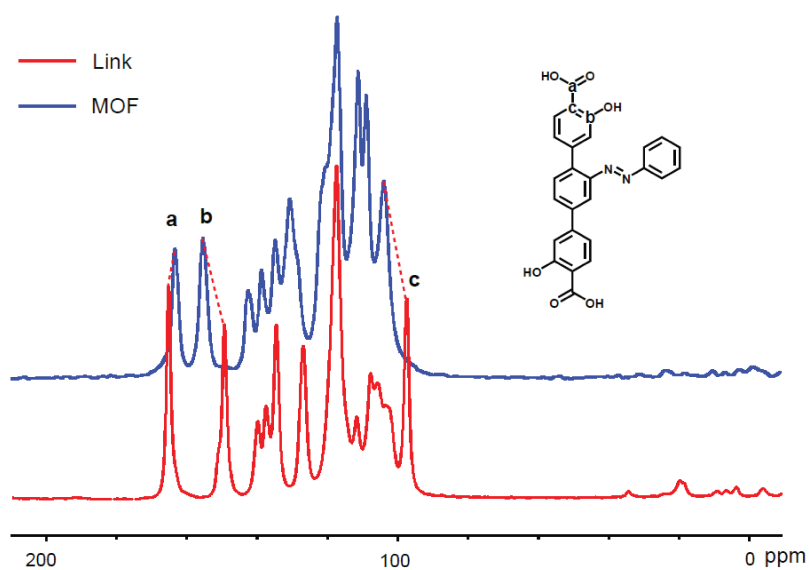


Figure 2.13:  $^{13}\text{C}$  NMR of azobenzene link and azo-IRMOF-74-III in the solid state.

#### 2.4.8 Fluorescence monitoring of wavelength specific release experiment

The fluorescence of the solvent above a 100 mg sample of azo-IRMOF-74-III loaded with propidium iodide was monitored with a 448 nm laser in a setup identical to the other release studies within this paper. After a baseline was established, a 647 nm laser was focused on the sample of particles; no release was observed. Subsequently, a 403 nm laser was focused on the sample and an immediate increase in the fluorescence signal was observed.

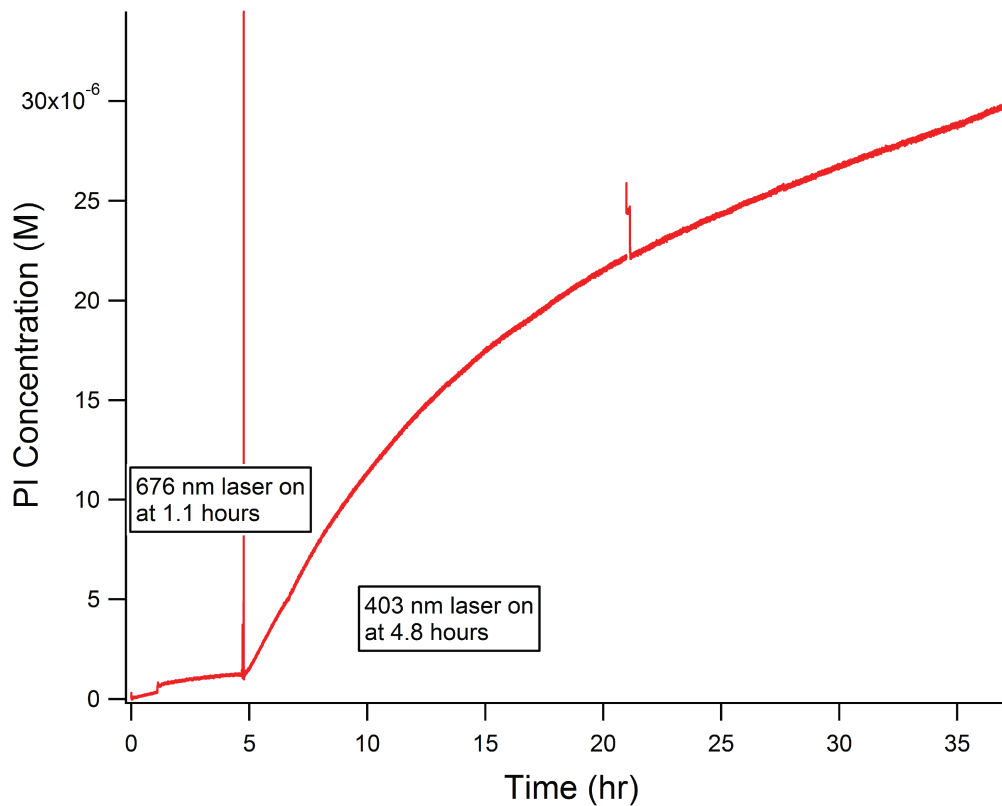


Figure 2.14: Time-dependent concentration of propidium iodide released from azo-IRMOF-74-III under sequential exposure to 647 nm and 403 nm lasers.

#### 2.4.9 UV-vis determination of loading efficiency of propidium iodide into azo-IRMOF-74-III

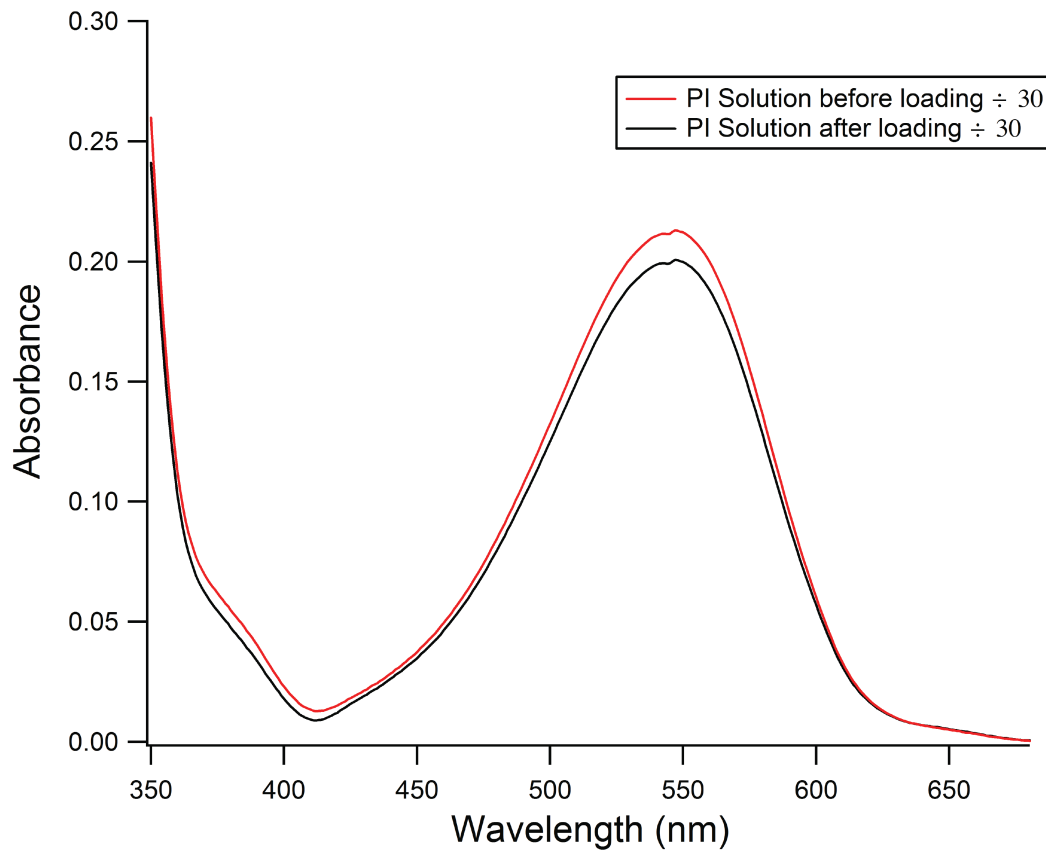


Figure 2.15: UV-vis spectra of a propidium iodide solution before and after loading a 100 mg sample of azo-IRMOF-74-III for three days. The 6% difference in concentration corresponds to the amount of dye uptaken by the particles.

#### 2.4.10 UV-vis spectra of an ethanol solution of the azo-linker and magnesium chloride

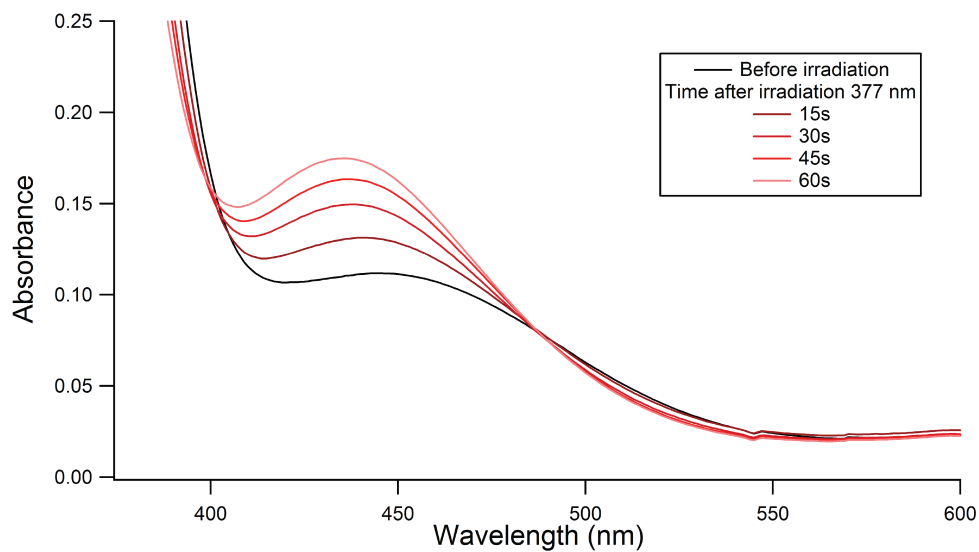


Figure 2.16: Absorption spectra of a 0.2 mM azo-linker and 0.8 mM MgCl<sub>2</sub> solution in ethanol before and after exposure to 377 nm light for 15 s intervals. An isosbestic point at 403 nm is observed.

## CHAPTER 3

# Heterogeneous Heck Coupling in Multivariate Metal-Organic Frameworks for Enhanced Selectivity

Multivariate metal-organic frameworks (termed MTV-MOFs) are porous crystalline solids in which the pores are lined with multiple organic functional groups. [30, 101–104] This report describes heterogeneous Heck coupling reactions in a series of MTV-MOFs where postsynthetic modification is used to adjust and embed specific amounts of catalytically active Pd(II) ions while avoiding pore blockage. [41, 105–107] MOFs as heterogeneous catalysts have been studied because of their high porosity and their ability to incorporate different catalytic units. [43, 44, 46, 108] A distinct advantage of the MTV platform [47, 109] is the ability to control the density of the active sites and the porosity of a catalytic MOF. Varying the percentage of functionalized links, in this case amino-functionalized benzene dicarboxylate (BDC-NH<sub>2</sub>) in the original synthesis of the MOF provides a means of tuning the amount of metal catalyst lining the pores and optimization of its activity.

Heck coupling reactions to form aromatic carbon-carbon bonds are one of the most important and useful ways to prepare complex organic molecules. [110] Due to its outstanding stereoselectivity, Heck coupling is of particular interest in the pharmaceutical chemistry [111] and has been demonstrated in both homogeneous and heterogeneous systems previously, including other MOFs. [112, 113] To high-

light the advantage of combining the MTV approach with postmodification, we investigated the Heck coupling reaction for the synthesis of resveratrol trimethyl ether, a pharmaceutically relevant precursor. Resveratrol is suspected to play a role in the cardioprotective effects of red wine and is of great interest for possible use in cancer treatment. [114] It is found that MOFs with higher porosity and lower density of metal binding sites achieve higher catalytic turnover and selectivity than MOFs with maximal density of metal binding sites.

The MOF-5 structure with 1,4-benzenedicarboxylate (BDC) was assembled by varying amounts of BDC-NH<sub>2</sub> to yield five MOFs, Zn<sub>4</sub>O(BDC-NH<sub>2</sub>)<sub>n</sub>(BDC)<sub>(3-n)</sub> ( $n = 3, 2.4, 1.8, 1.2, 0.9, 0.75, 0.6, 0.3$  and  $0.15$ ). [27, 28] Each compound was postsynthetically modified by reaction with salicylic aldehyde to give the imine derivative and metalated with Pd to give the palladium functionalized framework (Figure 3.1). The structural integrity of the framework was confirmed by a powder X-ray diffraction pattern (PXRD), which was coincident to that of simulated structures. The presence of the imine moiety was confirmed by a resonance at 255 ppm in the <sup>15</sup>N cross-polarization magic angle spinning nuclear magnetic resonance (CP/MAS NMR) spectrum. The MOF was digested in DCl/D<sub>2</sub>O and analyzed with <sup>1</sup>H solution-state NMR to ascertain the yield of the imine reaction (See SI).

After fully characterizing our frameworks, the catalytic activity of our MOFs in heterogeneous Heck coupling reaction to form resveratrol trimethyl ether was investigated (Figure 3.2(a)). While Heck coupling has been demonstrated in heterogeneous systems previously, concerns of recyclability, [42, 115] selectivity, [116] and catalyst leaching [117] continue to plague current systems and led us to investigate the effect of catalyst loading and porosity on yield and selectivity. Our reaction conditions were selected based on a previously published work involving homogenous palladium catalysts. [118] The Heck coupling was performed by loading 1-bromo-3,5-methoxybenzene (0.434 g, 2 mmol), 4-vinylanisole (0.401

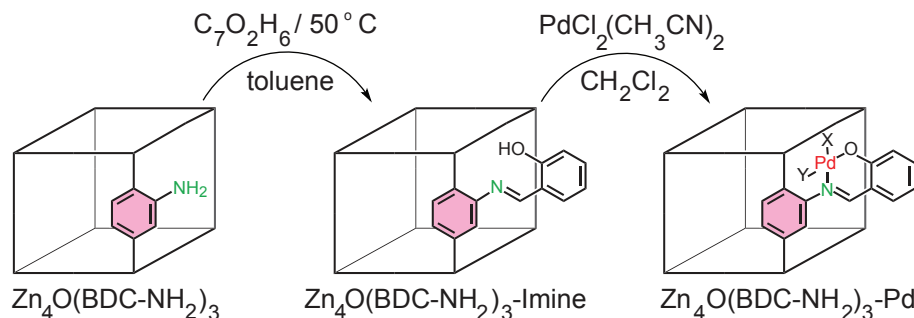


Figure 3.1: Schematic representation of post-synthetic modification and metalation of  $\text{Zn}_4\text{O}(\text{BDC-NH}_2)_3$ , X and Y are Cl and  $\text{CH}_3\text{CN}$ , respectively.

mL, 3 mmol), triethylamine (0.42 mL, 3 mmol), tetra-*n*-butylammonium bromide [TBAB] (0.32 mg, 1 mmol), MOF (20 mg), dodecane (1.0 mmol, inert internal standard) and DMA (6 mL) into a Schlenk flask, then heating to  $120^\circ\text{C}$  for 12 hours. The reaction mixture was monitored using gas chromatography-mass spectrometry (GC-MS).

The reaction conditions for catalysis were optimized by varying the reaction temperature and monitoring the conversion rate. Temperatures in excess of  $120^\circ\text{C}$  did not improve the conversion rate. In addition, each GC-MS spectrum was analysed for both isomers of resveratrol trimethyl ether to determine the trans to cis ratio among the product mixture (Figure 3.2C). Selectively obtaining the trans isomer of resveratrol is of great interest as it has been shown to have greater pharmaceutical activity and cardioprotective activity than the cis isomer. [119]

Figure 3.2B shows the catalytic activity of nine catalysts as well as unmetalated MOF-5 [ $\text{Zn}_4\text{O}(\text{BDC})_3$ ] and their respective surface areas. Interestingly, we see peak catalytic activity for  $\text{Zn}_4\text{O}(\text{BDC-NH}_2)_{0.6}(\text{BDC})_{2.4}\text{-Pd}$ , which has lower metal loading than many other structures but still maintains high surface area. In addition, our MOFs show high selectivity for the trans isomer of resveratrol



trimethyl ether, especially at low metal loading (Figure 3.2C). These results suggest that catalytic conversion varied according to two factors: metalation and porosity. Increased porosity allows for more space in the pore for the aryl halide to perform oxidative addition at the Pd center and for possible cis to trans isomerization at the active site, increasing reaction yield and selectivity in agreement with published reaction mechanisms. [120] Increased BDC-NH<sub>2</sub> loading results in more palladium sites potentially available for catalysis; yet, at higher loadings, these results show that catalytic activity rapidly declines. Peak reaction yield occurs at lower metal loading, but a minimum threshold exists in our frameworks for number of catalytically active sites needed to maintain maximum conversion, in this case 20% BDC-NH<sub>2</sub>. The combination of high reactivity and selectivity coupled with exceptional recyclability seen in Figure 3.3 make these MOFs an excellent alternative to current state of the art heterogeneous catalysts such as zeolites [121] and mesoporous silica. [122] However, a direct comparison between our catalyst and these systems cannot be made due to differing reaction substrates and conditions.

We tested two of our synthesized catalysts [Zn<sub>4</sub>O(BDC-NH<sub>2</sub>)<sub>0.6</sub>(BDC)<sub>2.4</sub>-Pd and Zn<sub>4</sub>O(BDC-NH<sub>2</sub>)<sub>3</sub>-Pd] for catalytic recyclability and possible metal leaching. Our MOFs maintained high crystallinity for up to 10 catalytic cycles (Figure 3.3) as well as high yield and selectivity. In addition, after filtering off the MOF, ICP-AES was performed on the reaction mixture to confirm that no Pd leaching occurred. The heterogeneous nature of the Heck coupling was confirmed by filtration. After the coupling reaction was completed, the MOF was filtered and fresh 1-bromo-3,5-methoxybenzene and 4-vinylanisole were added to the filtrate. Using the filtrate, the reaction was run again under analogous conditions to the initial experiment and no catalytic conversion was observed. In addition, no catalytic conversion was observed if an unmetalated MOF was used in the initial reaction mixture.

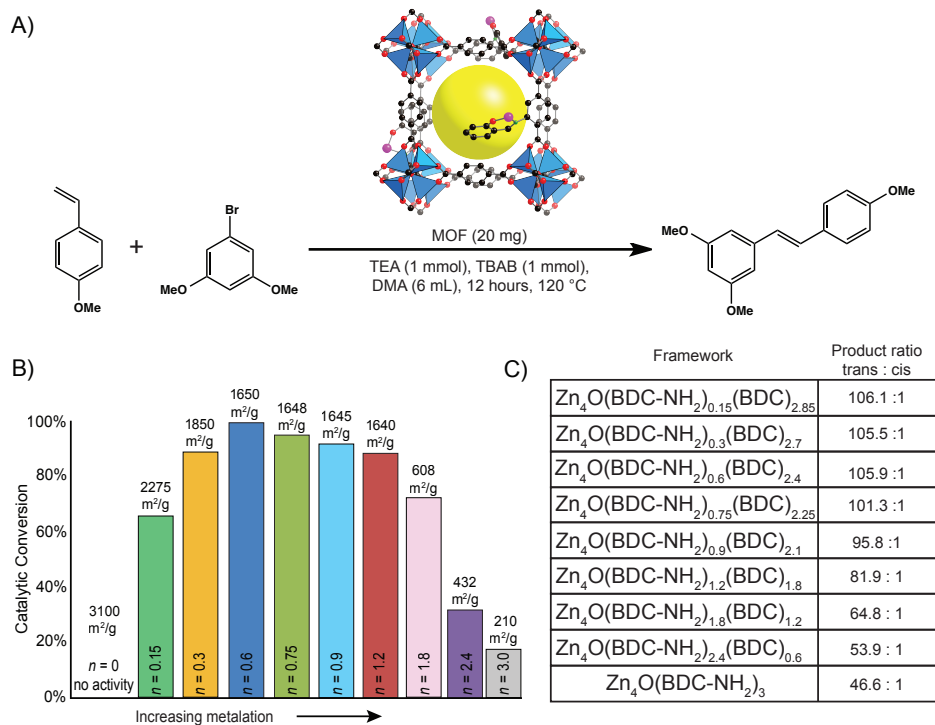


Figure 3.2: MOF performance as catalyst in a Heck coupling reaction. (A) Reaction of 4-vinylanisole and 1-bromo-3,5-methoxybenzene catalysed by MOF to form resveratrol trimethyl ether (B) Catalytic conversion as a function of increasing metalation. Indicated specific surface areas ( $\text{m}^2/\text{g}$ ) were calculated from Brunauer-Emmett-Teller (BET) analysis of isotherms, as shown in the SI section. (C) Selectivity of Heck coupling for each MOF. As metalation decreases, we see higher selectivity for the trans isomer until a plateau is reached below  $n = 0.6$  (trans : cis product ratio approximately 106 : 1).

To ensure that no palladium nanoparticles or aggregates were formed during the post-synthetic modification, we performed selective poisoning of our catalyst through use of  $\text{Hg}(0)$  and  $\text{PPh}_3$ .  $\text{Hg}(0)$  has been shown to selectively poison metal-particle catalysts by amalgamating the metal and  $\text{PPh}_3$  selectively poisons molecular single-site catalysts. [123] After adding  $\text{Hg}(0)$  to our reaction mixture,

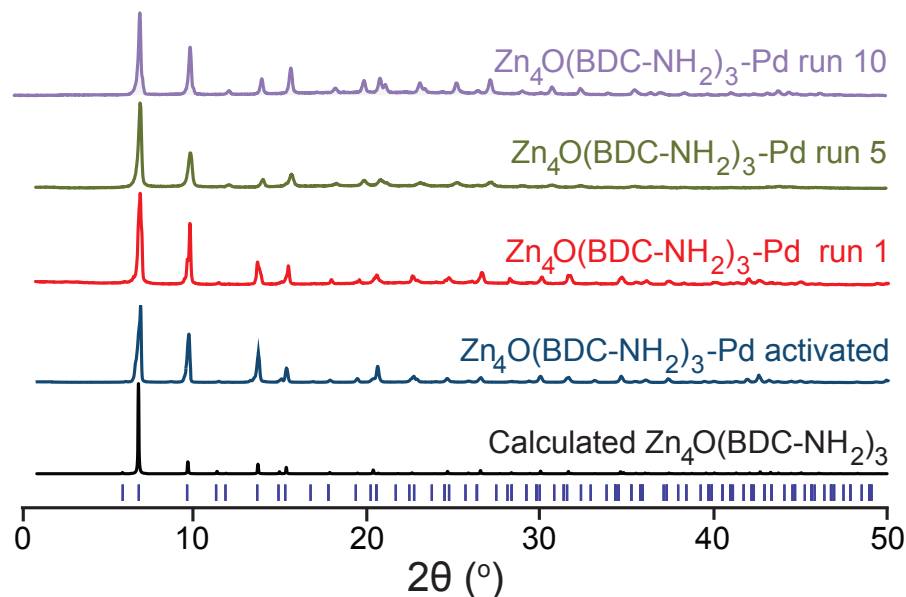


Figure 3.3: PXRD analysis for  $\text{Zn}_4\text{O}(\text{BDC-NH}_2)_3\text{-Pd}$  indicate crystallinity is maintained after multiple catalytic cycles. PXRD spectra of calculated  $\text{Zn}_4\text{O}(\text{BDC-NH}_2)_3$  (black), activated  $\text{Zn}_4\text{O}(\text{BDC-NH}_2)_3\text{-Pd}$  (blue),  $\text{Zn}_4\text{O}(\text{BDC-NH}_2)_3\text{-Pd}$  after one catalytic cycle (red), after five catalytic cycles (green), and after ten catalytic cycles (purple). Dark blue ticks indicate the positions of Bragg reflections.

we see no change in reaction yield or selectively, indicating that we have no metal aggregates within our frameworks (see SI). In a separate trial, we added  $\text{PPh}_3$  to our reaction mixture and observed an immediate drop-off in catalytic activity (see SI). The results of these tests indicate that we have a single atom Pd catalyst as opposed to Pd nanoparticles or aggregates within the pores.

In conclusion, we have developed a new heterogeneous Heck coupling catalyst and successfully demonstrated its activity by synthesizing resveratrol trimethyl ether. While direct comparisons to other heterogeneous catalysts are difficult due to different reaction substrates and conditions, our catalyst shows an excellent

combination of high activity, selectivity and recyclability. The observed decreased catalytic activity with increased BDC-NH<sub>2</sub> loading is attributed to the blocking of access to the palladium sites as more links are reacted with imine functionalities and Pd, leading to a decrease in overall porosity of the MOFs. The interplay of metalation and porosity implies that the catalytic activity of the MOFs can be adjusted to maximize catalytic efficiency.

### 3.1 Supporting Information

#### 3.1.1 Materials and general procedures

All reagents, unless otherwise stated, were obtained from commercial sources (Alfa Aesar, Cambridge isotope laboratories, Sigma Aldrich, TCI) and were used without further purification. Reported MOF crystallization yields were unoptimized. All experiments other than ICP-AES (performed at University of Southern California) were performed at the University of California, Los Angeles, Department of Chemistry and Biochemistry.

#### 3.1.2 Synthesis of all Zn<sub>4</sub>O(BDC-NH<sub>2</sub>)<sub>n</sub>(BDC)<sub>(3-n)</sub> (n = 3, 2.4, 1.8, 1.2, 0.9, 0.75, 0.6, 0.3 and 0.15) samples

##### 3.1.2.1 Zn<sub>4</sub>O(C<sub>8</sub>H<sub>4</sub>O<sub>4</sub>)<sub>2.85</sub>(C<sub>8</sub>NH<sub>5</sub>O<sub>4</sub>)<sub>0.15</sub>

A mixture of H<sub>2</sub>BDC-NH<sub>2</sub> (9 mg, 0.05 mmol), H<sub>2</sub>BDC (157 mg, 0.95 mmol) and zinc nitrate hexahydrate (890 mg, 3.0 mmol) was added to DMF (50 mL) and sonicated until the components were fully dissolved. The static solution was heated at 85°C for 24 h to form single crystals. The crystals were collected and washed with DMF (3 times, 30 mL) over a 3-h period.

#### **3.1.2.2 $\text{Zn}_4\text{O}(\text{C}_8\text{H}_4\text{O}_4)_{2.7}(\text{C}_8\text{NH}_5\text{O}_4)_{0.3}$**

A mixture of  $\text{H}_2\text{BDC-NH}_2$  (18 mg, 0.10 mmol),  $\text{H}_2\text{BDC}$  (149 mg, 0.90 mmol) and zinc nitrate hexahydrate (890 mg, 3.0 mmol) was added to DMF (50 mL) and sonicated until the components were fully dissolved. The static solution was heated at 85°C for 24 h to form single crystals. The crystals were collected and washed with DMF (3 times, 30 mL) over a 3-h period.

#### **3.1.2.3 $\text{Zn}_4\text{O}(\text{C}_8\text{H}_4\text{O}_4)_{2.4}(\text{C}_8\text{NH}_5\text{O}_4)_{0.6}$**

A mixture of  $\text{H}_2\text{BDC-NH}_2$  (63 mg, 0.34 mmol),  $\text{H}_2\text{BDC}$  (108 mg, 0.65 mmol) and zinc nitrate hexahydrate (890 mg, 3.0 mmol) was added to DMF (50 mL) and sonicated until the components were fully dissolved. The static solution was heated at 85°C for 24 h to form single crystals. The crystals were collected and washed with DMF (3 times, 30 mL) over a 3-h period.

#### **3.1.2.4 $\text{Zn}_4\text{O}(\text{C}_8\text{H}_4\text{O}_4)_{2.25}(\text{C}_8\text{NH}_5\text{O}_4)_{0.75}$**

A mixture of  $\text{H}_2\text{BDC-NH}_2$  (45 mg, 0.25 mmol),  $\text{H}_2\text{BDC}$  (124 mg, 0.75 mmol) and zinc nitrate hexahydrate (890 mg, 3.0 mmol) was added to DMF (50 mL) and sonicated until the components were fully dissolved. The static solution was heated at 85°C for 24 h to form single crystals. The crystals were collected and washed with DMF (3 times, 30 mL) over a 3-h period.

#### **3.1.2.5 $\text{Zn}_4\text{O}(\text{C}_8\text{H}_4\text{O}_4)_{2.1}(\text{C}_8\text{NH}_5\text{O}_4)_{0.9}$**

A mixture of  $\text{H}_2\text{BDC-NH}_2$  (116 mg, 0.70 mmol),  $\text{H}_2\text{BDC}$  (116 mg, 0.70 mmol) and zinc nitrate hexahydrate (890 mg, 3.0 mmol) was added to DMF (50 mL) and sonicated until the components were fully dissolved. The static solution was heated at 85°C for 24 h to form single crystals. The crystals were collected and

washed with DMF (3 times, 30 mL) over a 3-h period.

#### **3.1.2.6 $\text{Zn}_4\text{O}(\text{C}_8\text{H}_4\text{O}_4)_{1.8}(\text{C}_8\text{NH}_5\text{O}_4)_{1.2}$**

A mixture of  $\text{H}_2\text{BDC-NH}_2$  (120 mg, 0.66 mmol),  $\text{H}_2\text{BDC}$  (100 mg, 0.60 mmol) and zinc nitrate hexahydrate (890 mg, 3.0 mmol) was added to DMF (50 mL) and sonicated until the components were fully dissolved. The static solution was heated at 85°C for 24 h to form single crystals. The crystals were collected and washed with DMF (3 times, 30 mL) over a 3-h period.

#### **3.1.2.7 $\text{Zn}_4\text{O}(\text{C}_8\text{H}_4\text{O}_4)_{1.2}(\text{C}_8\text{NH}_5\text{O}_4)_{1.8}$**

$\text{H}_2\text{BDC-NH}_2$  (136 mg, 0.750 mmol),  $\text{H}_2\text{BDC}$  (42 mg, 0.25 mmol) and zinc nitrate hexahydrate (890 mg, 3.0 mmol) was added to DMF (50 mL) and sonicated until the components were fully dissolved. The static solution was heated at 85°C for 24 h to form single crystals. The crystals were collected and washed with DMF (3 times, 30 mL) over a 3-h period.

#### **3.1.2.8 $\text{Zn}_4\text{O}(\text{C}_8\text{H}_4\text{O}_4)_{0.6}(\text{C}_8\text{NH}_5\text{O}_4)_{2.4}$**

A mixture of  $\text{H}_2\text{BDC-NH}_2$  (163 mg, 0.89 mmol),  $\text{H}_2\text{BDC}$  (17 mg, 0.10 mmol) and zinc nitrate hexahydrate (890 mg, 3.0 mmol) was added to DMF (50 mL) and the mixture was sonicated until the components were fully dissolved. The static solution was heated at 85°C for 24 h to form single crystals. The crystals were collected and washed with DMF (3 times, 30 mL) over a 3-h period.

#### **3.1.2.9 $\text{Zn}_4\text{O}(\text{BDC-NH}_2)_3$**

The synthesis of IRMOF-3 was analogous to those reported in the literature. [28]  $\text{H}_2\text{BDC-NH}_2$  (180 mg, 0.99 mmol) and zinc nitrate hexahydrate (890 mg, 3 mmol)

were added to DMF (50 mL) and the mixture was sonicated until the components were fully dissolved. The static solution was heated at 85°C for 24 h to form single crystals. The crystals were collected and washed with DMF (3 times, 10 mL) repeatedly over a 3-h period. PXRD was used to confirm the phase purity of the as-synthesized samples.

### **3.1.3 Metalation of $\text{Zn}_4\text{O}(\text{BDC-NH}_2)_n(\text{BDC})_{(3-n)}$ ( $n = 3, 2.4, 1.8, 1.2, 0.9, 0.75, 0.6, 0.3$ and $0.15$ )**

Utilizing a two-step postmodification reaction, imine condensation followed by metalation, all samples were metalated using identical synthetic conditions. [106] For example, a freshly solvent-exchanged sample of  $\text{Zn}_4\text{O}(\text{BDC-NH}_2)_n(\text{BDC})_{(3-n)}$  was reacted with salicyclic aldehyde in toluene to form an imine bond in the framework. Before metalation could be achieved, the framework was washed to remove excess salicyclic acid. After solvent exchange with  $\text{CH}_2\text{Cl}_2$  was completed,  $\text{PdCl}_2(\text{CH}_3\text{CN})_2$  in  $\text{CH}_2\text{Cl}_2$  was added, and allowed to stand at room temperature. After 48 h the sample was exchanged with  $\text{CH}_2\text{Cl}_2$  to remove excess  $\text{PdCl}_2(\text{CH}_3\text{CN})_2$ . The framework was then exposed to a vacuum (30 mTorr) at 85°C to remove all of the solvent from the pores.

#### **3.1.3.1 Imine formation in $\text{Zn}_4\text{O}(\text{BDC-NH}_2)_3$**

DMF-exchanged  $\text{Zn}_4\text{O}(\text{BDC-NH}_2)_3$  (100 mg) was solvent exchanged with dry toluene (5–20 mL) over a 2-h period. Salicyclic aldehyde (1.0 mL, 7.1 mmol) was added to  $\text{Zn}_4\text{O}(\text{BDC-NH}_2)_3$  in toluene and the reaction was allowed to stand at 50°C for 5 days. After 5 days, the sample was exchanged with dry toluene (5 times, 20 mL) to remove unreacted salicyclic aldehyde, yielding  $\text{Zn}_4\text{O}(\text{BDC-NH}_2)_3$ -Imine.

### 3.1.3.2 Metalation of $\text{Zn}_4\text{O}(\text{BDC-NH}_2)_3$

Toluene exchanged  $\text{Zn}_4\text{O}(\text{BDC-NH}_2)_3$ -Imine (100 mg) was solvent exchanged with  $\text{CH}_2\text{Cl}_2$  (1 times, 20 mL) over a 2-h period.  $\text{PdCl}_2(\text{CH}_3\text{CN})_2$  (50 mg, 0.19 mmol) was dissolved in  $\text{CH}_2\text{Cl}_2$  (40 mL) to which the  $\text{Zn}_4\text{O}(\text{BDC-NH}_2)_3$ -Imine was added in a minimum amount of solvent. The reaction was allowed to stand at room temperature for 2 days, at which point it was washed with  $\text{CH}_2\text{Cl}_2$  (3 times, 20 mL) over a 2-h period, followed by  $\text{CH}_2\text{Cl}_2$  (3 times, 20 mL) over a 3-day period. The solvents were removed from the pores of the framework by vacuum pumping (at 30 mTorr) for 12 h at  $85^\circ\text{C}$  to yield  $\text{Zn}_4\text{O}(\text{BDC-NH}_2)_3$ -Pd.

### 3.1.3.3 Imine formation in $\text{Zn}_4\text{O}(\text{BDC-NH}_2)_n(\text{BDC})_{(3-n)}$ ( $n = 2.4, 1.8, 1.2, 0.9, 0.75, 0.6, 0.3$ and $0.15$ )

DMF exchanged  $\text{Zn}_4\text{O}(\text{BDC-NH}_2)_n(\text{BDC})_{(3-n)}$  (100 mg) was exchanged with toluene (5 times, 20 mL) over a 2-h period. Salicyclic aldehyde (1.0 mL, 7.1 mmol) was added to  $\text{Zn}_4\text{O}(\text{BDC-NH}_2)_n(\text{BDC})_{(3-n)}$  in toluene and the reaction was allowed to stand at  $50^\circ\text{C}$  for 5 days. After 5 days, the sample was exchanged with fresh toluene (5 times, 20 mL) to remove unreacted salicyclic aldehyde, yielding  $\text{Zn}_4\text{O}(\text{BDC-NH}_2)_n(\text{BDC})_{(3-n)}$ -Imine.

### 3.1.3.4 Metalation of $\text{Zn}_4\text{O}(\text{BDC-NH}_2)_n(\text{BDC})_{(3-n)}$ -Imine

Toluene-exchanged  $\text{Zn}_4\text{O}(\text{BDC-NH}_2)_n(\text{BDC})_{(3-n)}$ -Imine was solvent exchanged with  $\text{CH}_2\text{Cl}_2$  (20 mL) over a 2-h period.  $\text{PdCl}_2(\text{CH}_3\text{CN})_2$  (50 mg, 0.19 mmol) was dissolved in  $\text{CH}_2\text{Cl}_2$  (20 mL) to which the  $\text{Zn}_4\text{O}(\text{BDC-NH}_2)_n(\text{BDC})_{(3-n)}$ -Imine was added in a minimum amount of solvent. The reaction was allowed to stand at room temperature for 2 days, at which point it was washed with  $\text{CH}_2\text{Cl}_2$  (3 times, 20 mL) over a 2-h period, followed by  $\text{CH}_2\text{Cl}_2$  (3 times, 20 mL) over a 3-day period. The solvents were removed from the pores of the framework by vacuum



(30 mTorr) for 12 h at 85°C to yield  $\text{Zn}_4\text{O}(\text{BDC-NH}_2)_n(\text{BDC})_{(3-n)}\text{-Pd}$ .

### 3.1.4 Powder X-ray diffraction data

The structural integrity of the unfunctionalized  $[\text{Zn}_4\text{O}(\text{BDC-NH}_2)_n(\text{BDC})_{(3-n)}]$ , the imine functionalized framework  $[\text{Zn}_4\text{O}(\text{BDC-NH}_2)_n(\text{BDC})_{(3-n)}\text{-Imine}]$ , and the Pd functionalized framework  $[\text{Zn}_4\text{O}(\text{BDC-NH}_2)_n(\text{BDC})_{(3-n)}\text{-Pd}]$  ( $n = 3, 2.4, 1.8, 1.2, 0.9, 0.75, 0.6, 0.3$  and  $0.15$ ) was confirmed by PXRD.

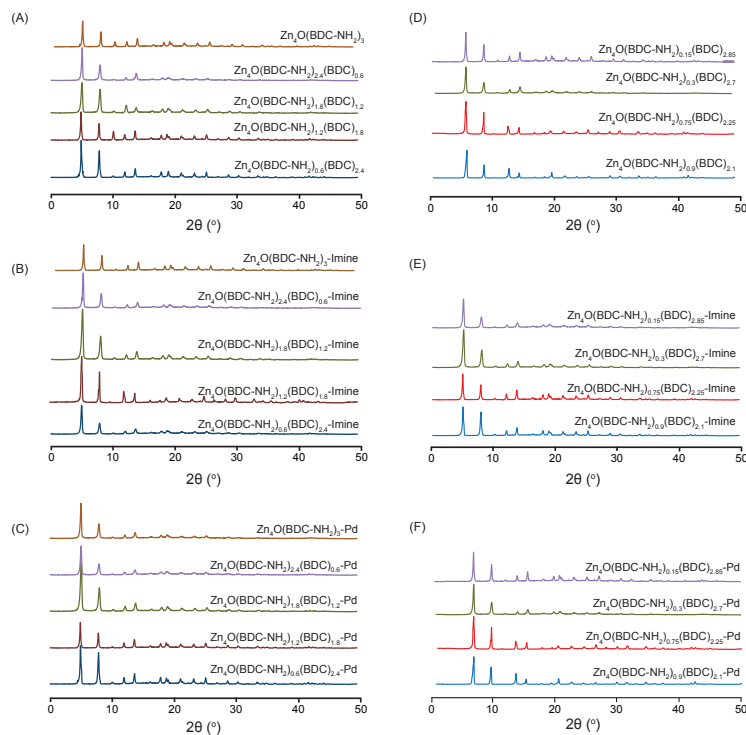


Figure 3.4: PXRD patterns of unfunctionalized (A, D), imine functionalized (B, E), and metalated frameworks (C, F).

### 3.1.5 Gas adsorption at 77 K

Upon activation of  $\text{Zn}_4\text{O}(\text{BDC-NH}_2)_n(\text{BDC})_{(3-n)}$  ( $n = 3, 2.4, 1.8, 1.2,$  and  $0.6$ ), the  $\text{N}_2$  isotherms of each material were measured at 77 K. Isotherms at 77 K indicated that metalation had decreased the porosity of  $\text{Zn}_4\text{O}(\text{BDC-NH}_2)_3\text{-Pd}$ , with the BET surface area of  $210 \text{ m}^2/\text{g}$ , analogous to other studies of metalation in  $\text{Zn}_4\text{O}(\text{BDC-NH}_2)_3$ . [105] However,  $\text{N}_2$  isotherms at 77 K confirmed other  $\text{Zn}_4\text{O}(\text{BDC-NH}_2)_n(\text{BDC})_{(3-n)}$  samples maintained high porosity upon metalation; the accuracy is  $10 \text{ m}^2/\text{g}$  for all samples. The maintenance of porosity displays the advantage of the application of the MTV-process in the metalation of MOFs with pores smaller than 1 nm. It is known that MOF samples after postsynthetic modification reactions sometimes show a significant hysteresis loop, [105] and this is most likely due to intercrystalline voids in the sample related to lowered crystallinity of the sample after the postsynthetic modification reaction. [124]

Low-pressure  $\text{N}_2$  adsorption experiments (below 760 Torr) were performed on a Quantachrome NOVA 4200e automatic volumetric gas adsorption analyzer. Ultra-high purity grade  $\text{N}_2$  (99.999% purity) and a liquid nitrogen bath (77 K) were used. For the estimation of surface areas, the BET method was applied using the adsorption branches of the  $\text{N}_2$  isotherms assuming a  $\text{N}_2$  cross-sectional area of  $16.2 \text{ \AA}^2/\text{molecule}$ .

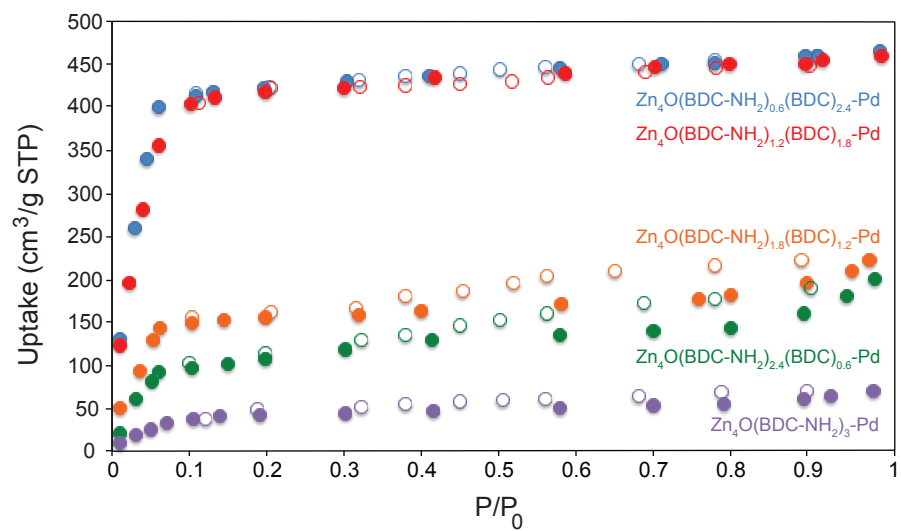


Figure 3.5: Nitrogen isotherms of all  $\text{Zn}_4\text{O}(\text{BDC-NH}_2)_n(\text{BDC})_{(3-n)}\text{-Pd}$  samples.

### 3.1.6 $^{15}\text{N}$ and $^1\text{H}$ solution NMR spectra and ICP-AES analysis

$^{15}\text{N}$  CP/MAS solid state NMR provides no information about the yield of reactions; therefore, we employed digestion NMR and ICP-MS to quantify the yield of postmodification and metalation techniques that have been used to quantify the yield of postmodification reactions in MOFs. [125] [126] Samples of metalated MOFs were digested in DCl/DMSO- $d^6$ , all visible peaks in the spectra were labeled with corresponding hydrogen atoms (letters A-F wherever possible) and the percentage amino-BDC and functionalization for each framework is shown in Figure 3.6 To determine the loading of the frameworks with palladium inductively coupled plasma atomic emission spectroscopy (ICP-AES) was performed, and  $\text{Zn}_4\text{O}:\text{Pd}$  ratios of 1:0.4, 1:0.7, 1:1.0, 1:1.1, and 1:1.7 for  $n = 0.6, 1.2, 1.8, 2.4$ , and 3.0, respectively, could be determined. All ICP-AES measurements have a standard deviation of 10%. MOF samples were digested in DMSO- $d^6$ /D $_2$ O/DCl. Liquid-state NMR spectra were performed on a Bruker AX 400 spectrometer.

Framework	Expected amino-BDC content (%)	Actual amino-BDC content (%)	Imine formation (% of amino-BDC functionalized)
$\text{Zn}_4\text{O}(\text{BDC-NH}_2)_{2/0.15}(\text{BDC})_{2.85}$	5	5.08	90
$\text{Zn}_4\text{O}(\text{BDC-NH}_2)_{2/0.3}(\text{BDC})_{2.7}$	10	9.97	90
$\text{Zn}_4\text{O}(\text{BDC-NH}_2)_{2/0.6}(\text{BDC})_{2.4}$	20	20.17	80
$\text{Zn}_4\text{O}(\text{BDC-NH}_2)_{2/0.75}(\text{BDC})_{2.25}$	25	24.95	80
$\text{Zn}_4\text{O}(\text{BDC-NH}_2)_{2/0.9}(\text{BDC})_{2.1}$	30	30.20	85
$\text{Zn}_4\text{O}(\text{BDC-NH}_2)_{2/1.2}(\text{BDC})_{1.8}$	40	40.10	80
$\text{Zn}_4\text{O}(\text{BDC-NH}_2)_{2/1.8}(\text{BDC})_{1.2}$	60	59.06	90
$\text{Zn}_4\text{O}(\text{BDC-NH}_2)_{2/2.4}(\text{BDC})_{0.6}$	80	79.69	90
$\text{Zn}_4\text{O}(\text{BDC-NH}_2)_3$	100	100	70

Figure 3.6: Percentage and degree of functionalization of amino-BDC in MTV-MOFs

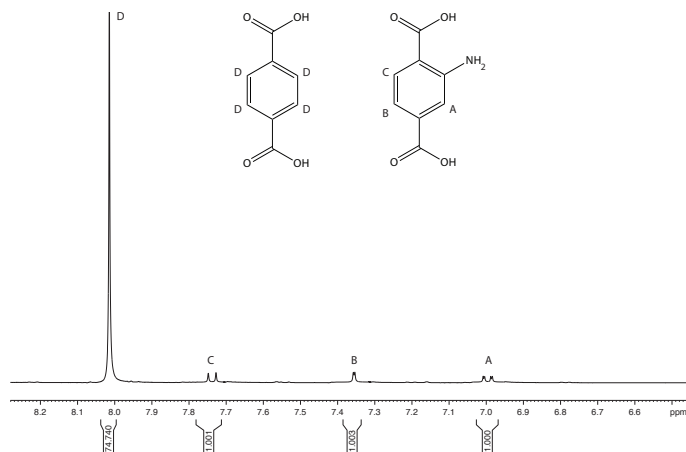


Figure 3.7: Digestion NMR spectrum of  $\text{Zn}_4\text{O}(\text{BDC-NH}_2)_{0.15}(\text{BDC})_{2.85}$ .

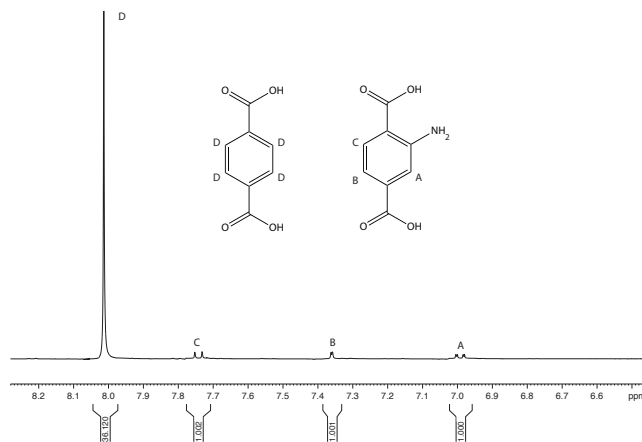


Figure 3.8: Digestion NMR spectrum of  $\text{Zn}_4\text{O}(\text{BDC-NH}_2)_{0.3}(\text{BDC})_{2.7}$ .

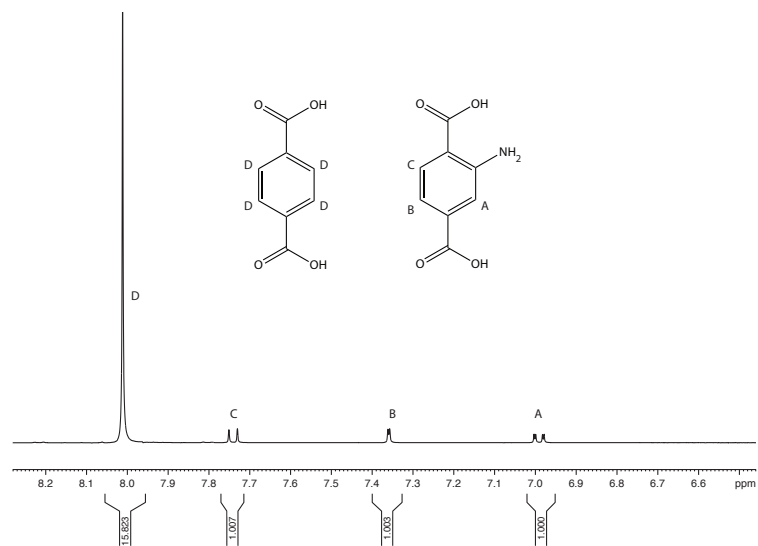


Figure 3.9: Digestion NMR spectrum of  $\text{Zn}_4\text{O}(\text{BDC-NH}_2)_{0.6}(\text{BDC})_{2.4}$ .

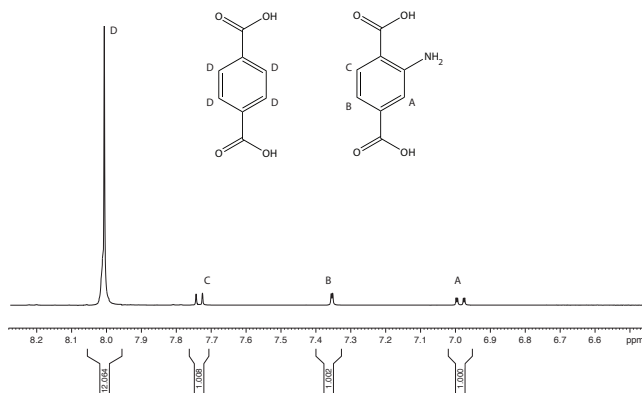


Figure 3.10: Digestion NMR spectrum of  $\text{Zn}_4\text{O}(\text{BDC-NH}_2)_{0.75}(\text{BDC})_{2.25}$ .

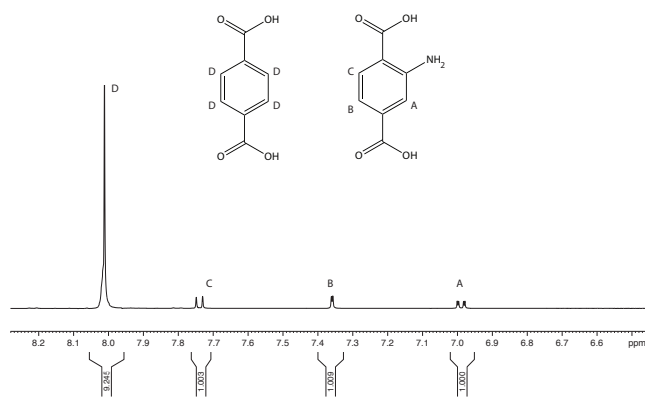


Figure 3.11: Digestion NMR spectrum of  $\text{Zn}_4\text{O}(\text{BDC-NH}_2)_{0.9}(\text{BDC})_{2.1}$ .

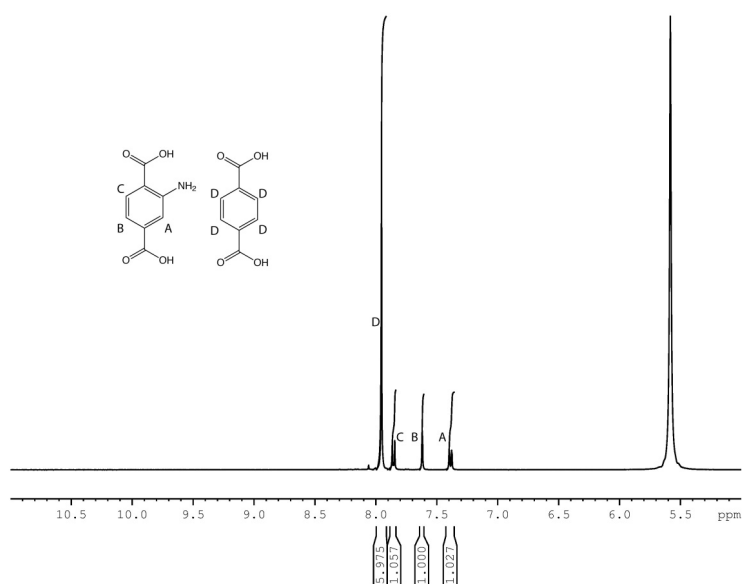


Figure 3.12: Digestion NMR spectrum of  $\text{Zn}_4\text{O}(\text{BDC-NH}_2)_{1.2}(\text{BDC})_{1.8}$ .

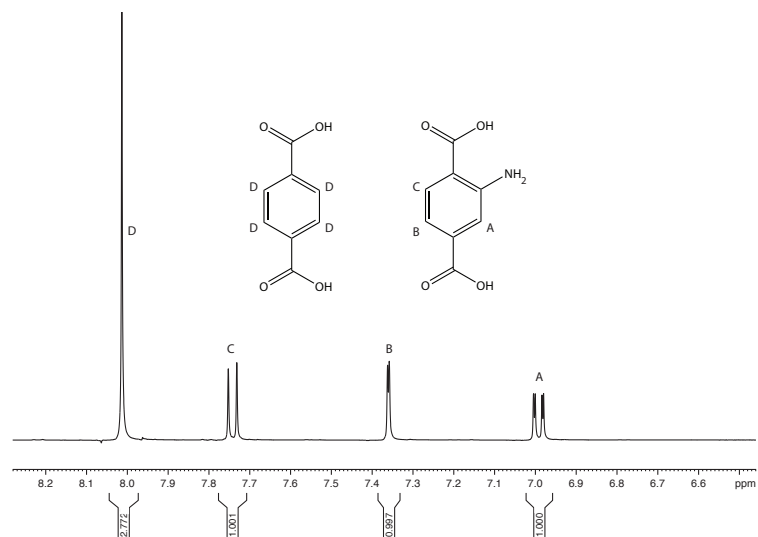


Figure 3.13: Digestion NMR spectrum of  $\text{Zn}_4\text{O}(\text{BDC-NH}_2)_{1.8}(\text{BDC})_{1.2}$ .

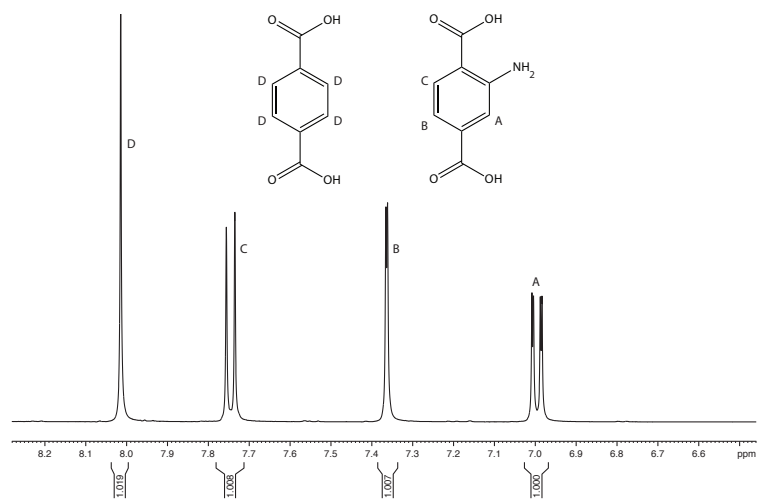


Figure 3.14: Digestion NMR spectrum of  $\text{Zn}_4\text{O}(\text{BDC-NH}_2)_{2.4}(\text{BDC})_{0.6}$ .



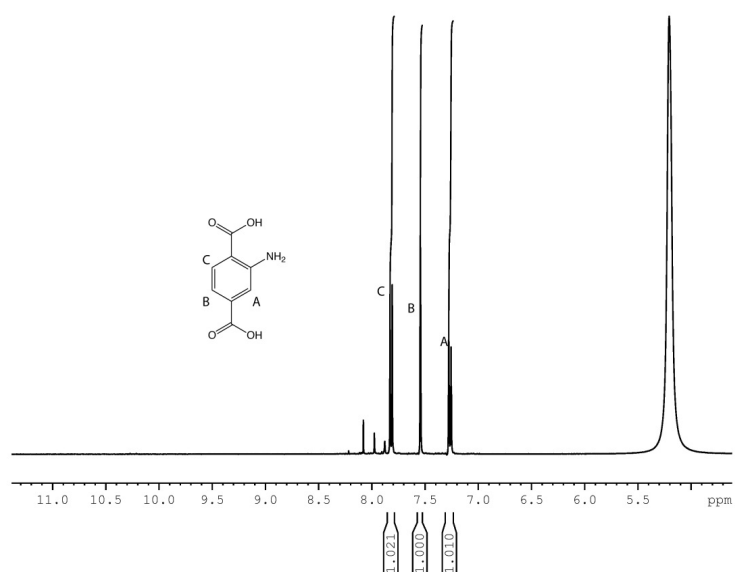


Figure 3.15: Digestion NMR spectrum of Zn<sub>4</sub>O(BDC-NH<sub>2</sub>)<sub>3</sub>.

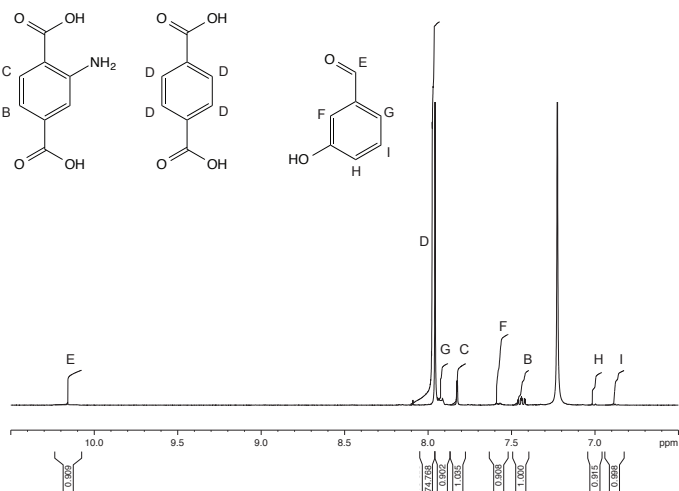


Figure 3.16: Digestion NMR spectrum of  $\text{Zn}_4\text{O}(\text{BDC-NH}_2)_{0.15}(\text{BDC})_{2.85}\text{-Pd}$ .

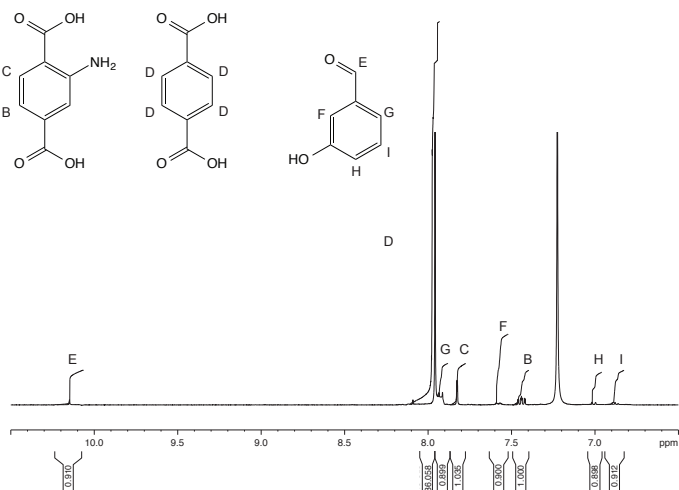


Figure 3.17: Digestion NMR spectrum of  $\text{Zn}_4\text{O}(\text{BDC-NH}_2)_{0.3}(\text{BDC})_{2.7}\text{-Pd}$ .

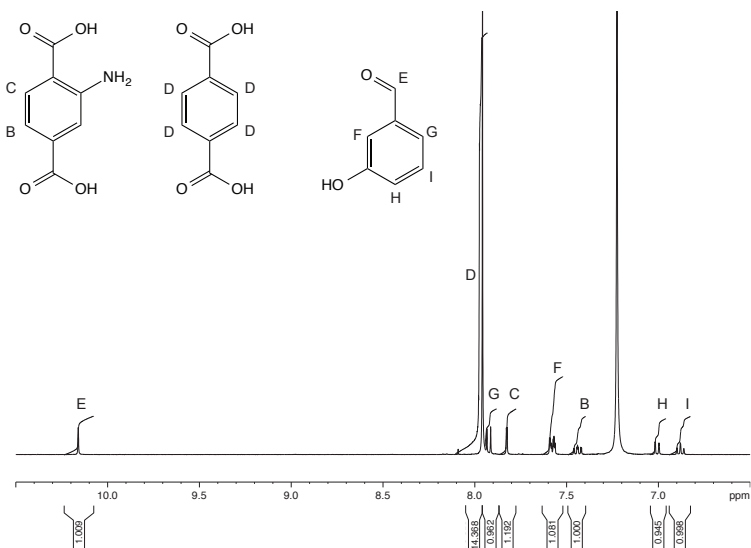


Figure 3.18: Digestion NMR spectrum of  $\text{Zn}_4\text{O}(\text{BDC-NH}_2)_{0.6}(\text{BDC})_{2.4}\text{-Pd}$ .

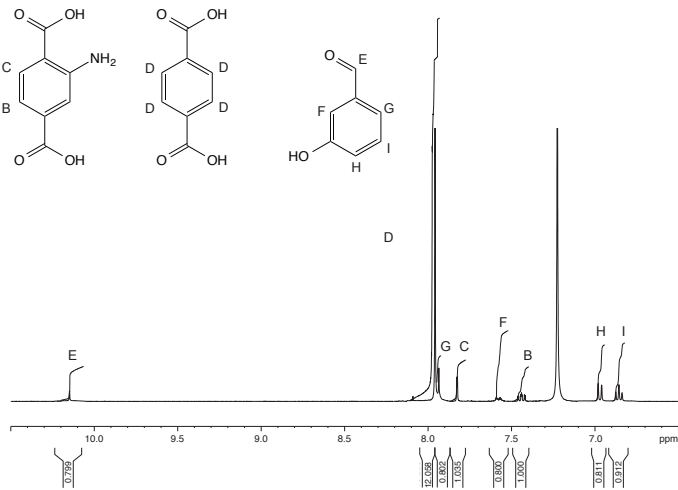


Figure 3.19: Digestion NMR spectrum of  $\text{Zn}_4\text{O}(\text{BDC-NH}_2)_{0.75}(\text{BDC})_{2.25}\text{-Pd}$ .

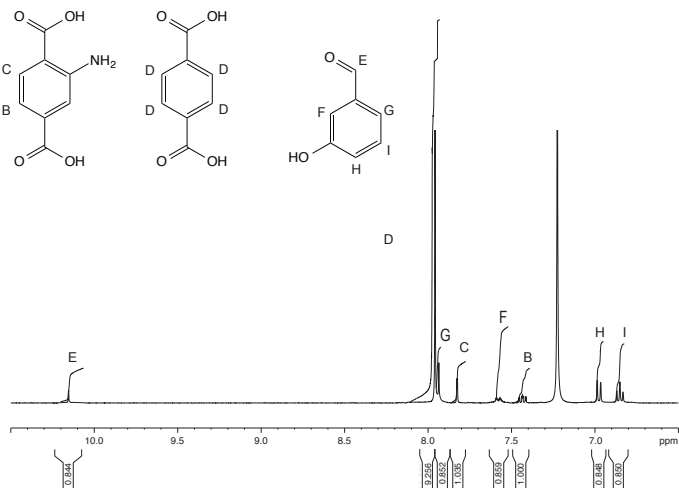


Figure 3.20: Digestion NMR spectrum of  $\text{Zn}_4\text{O}(\text{BDC-NH}_2)_{0.9}(\text{BDC})_{2.1}\text{-Pd}$ .

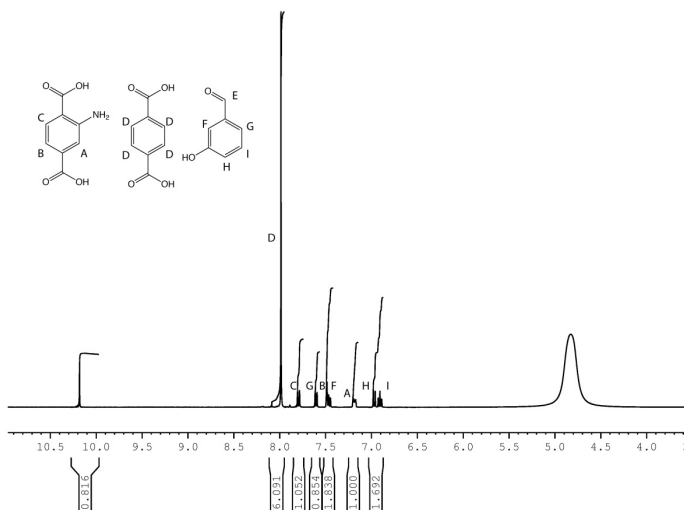


Figure 3.21: Digestion NMR spectrum of  $\text{Zn}_4\text{O}(\text{BDC-NH}_2)_{1.2}(\text{BDC})_{1.8}\text{-Pd}$ .

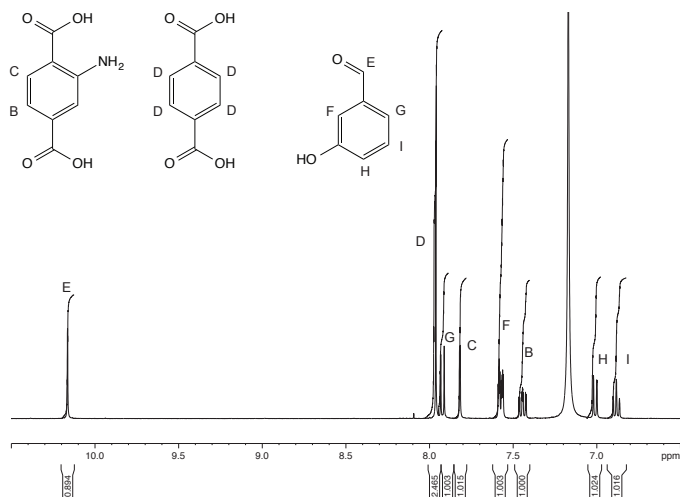


Figure 3.22: Digestion NMR spectrum of  $\text{Zn}_4\text{O}(\text{BDC-NH}_2)_{1.8}(\text{BDC})_{1.2}\text{-Pd}$ .

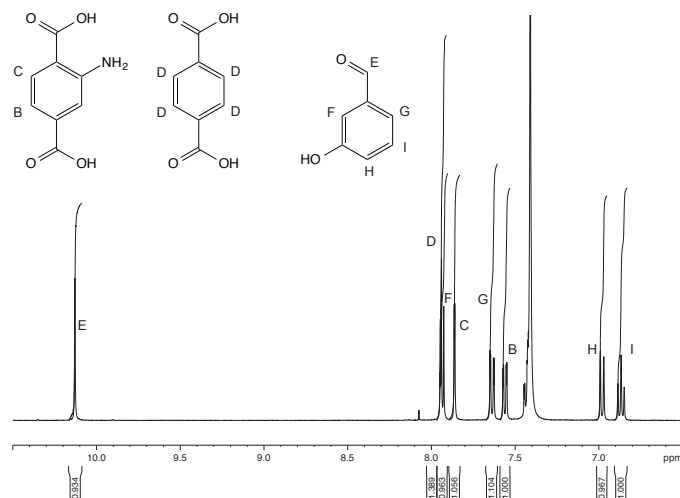


Figure 3.23: Digestion NMR spectrum of  $\text{Zn}_4\text{O}(\text{BDC-NH}_2)_{2.4}(\text{BDC})_{0.6}\text{-Pd}$ .

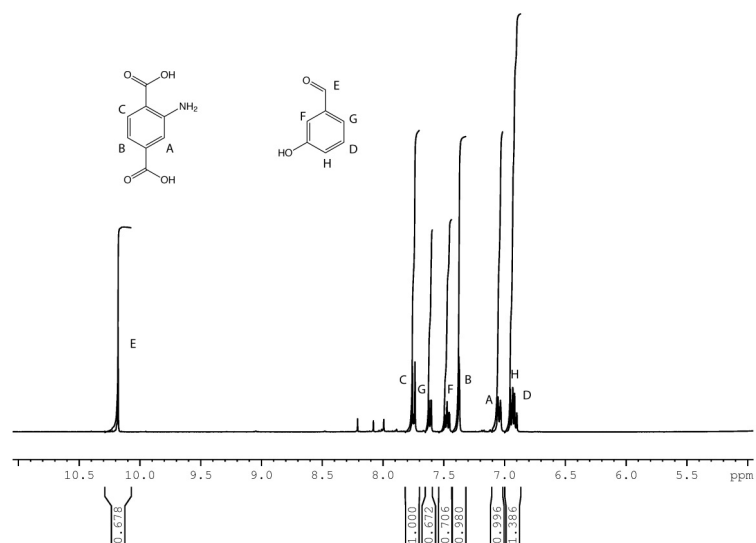


Figure 3.24: Digestion NMR spectrum of Zn<sub>4</sub>O(BDC-NH<sub>2</sub>)<sub>3</sub>-Pd.

### 3.1.7 Solid-state $^{15}\text{N}$ CP/MAS NMR spectroscopy

The palladium coordination was determined using  $^{15}\text{N}$  CP/MAS solid-state NMR spectroscopy, which characterizes the imine condensation and the metal binding site, with the use of  $^{15}\text{N}$  labeled BDC-NH<sub>2</sub>.  $\text{Zn}_4\text{O}(\text{BDC-NH}_2)_{1.2}(\text{BDC})_{1.8}$  was synthesized using labeled BDC-NH<sub>2</sub>,  $^{15}\text{N}$  CP/MAS solid-state NMR clearly showed an amine resonance at 65 ppm. [127] Upon postmodification with salicyclic acid an imine resonance is observed at 255 ppm in  $\text{Zn}_4\text{O}(\text{BDC-NH}_2)_{1.2}(\text{BDC})_{1.8}$ -Imine. In addition, the amine resonance is still observed at 68 ppm indicating the reaction does not proceed to completion. The final step of the postmodification in  $\text{Zn}_4\text{O}(\text{BDC-NH}_2)_{1.2}(\text{BDC})_{1.8}$ , metalation, was further characterized by  $^{15}\text{N}$  NMR, which contained a broad resonance at 10 ppm, the Pd- $^{15}\text{N}$  bond of the imine complex. This resonance was confirmed by comparison to a model compound  $\text{Pd}(\text{C}_{13}\text{H}_{10}\text{NO})_2$ , which also showed two resonances, at 5 and 13 ppm (Figure 3.25).

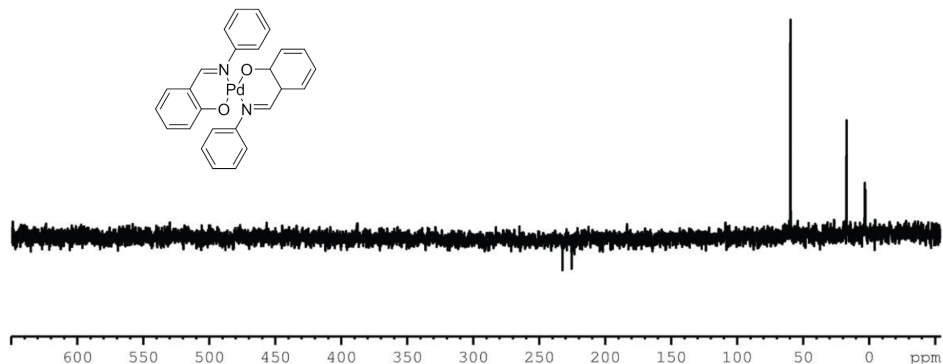


Figure 3.25:  $^{15}\text{N}$  solution spectrum of a model compound  $\text{Pd}(\text{C}_{13}\text{H}_{10}\text{NO})_2$  used to confirm the metal binding in the solid state NMR experiments.

High resolution solid-state NMR spectra were recorded at ambient pressure on a Bruker DSX-300 spectrometer using a standard Bruker MAS probe with 4 mm (outside diameter) zirconia rotors. The magic angle was found by maximizing the number and amplitudes of the signals of the rotational echoes observed in the  $^{79}\text{Br}$

MAS free induction signal from KBr.

$^{15}\text{N}$  CP MAS for the isotopically labeled materials were measured at 30.42 MHz. The  $^1\text{H}$  and  $^{15}\text{N}$  ninety-degree pulse widths were both 4 s. The CP contact time varied from 1.5 to 5 ms. The direct excitation NMR was measured at recycle delays of up to 45 seconds to allow for complete relaxation. The  $^{15}\text{N}$  chemical shifts are given relative to liquid  $\text{N}_2$  at zero ppm, calibrated using the nitrogen signal of glycine assigned to 36.2 ppm as secondary reference.

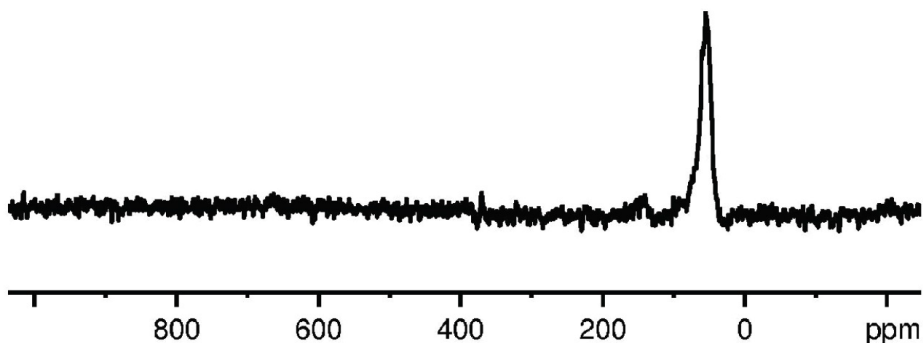


Figure 3.26:  $^{15}\text{N}$  CP/MAS NMR spectrum of  $\text{Zn}_4\text{O}(\text{BDC-NH}_2)_{1.2}(\text{BDC})_{1.8}$ .

The peak between 100 and 200 is most likely the result of protonation of the amine. This downfield shift of approximately 100 ppm from the free amine has been observed by our group [128] and other groups. [129]



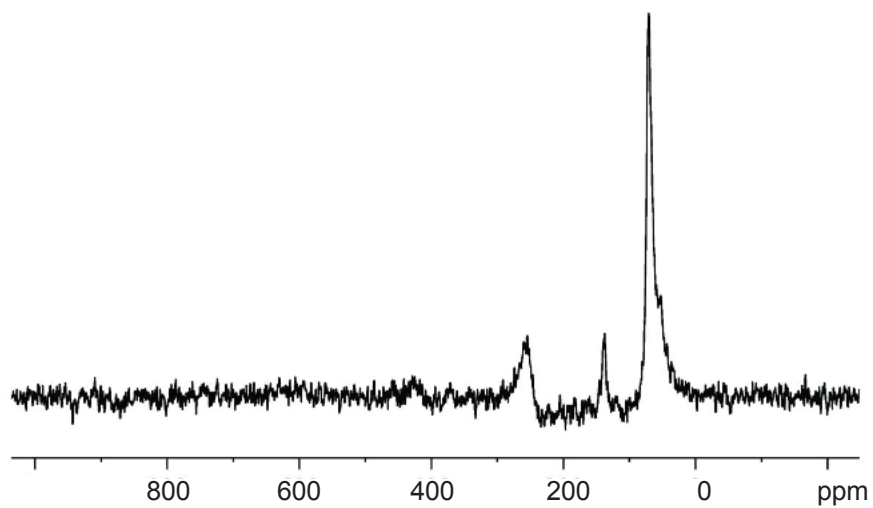


Figure 3.27:  $^{15}\text{N}$  CP/MAS NMR spectrum of  $\text{Zn}_4\text{O}(\text{BDC-NH}_2)_{1.2}(\text{BDC})_{1.8}\text{-Imine}$ .

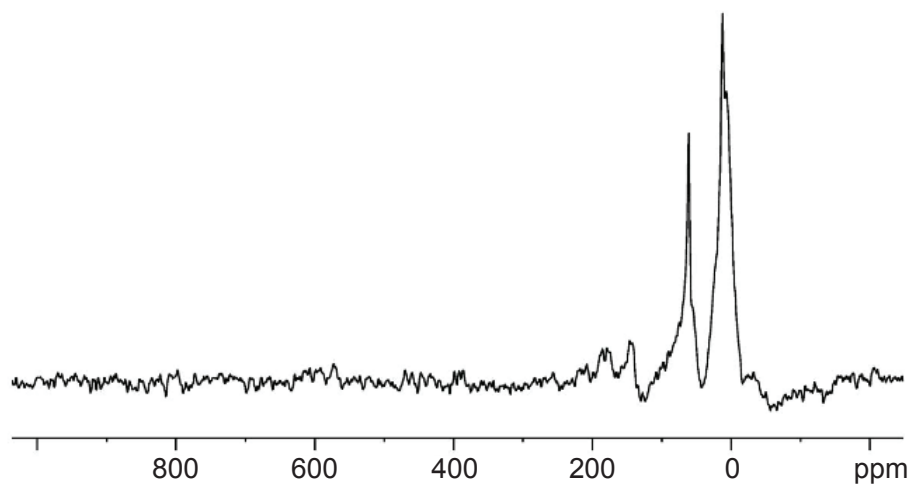


Figure 3.28:  $^{15}\text{N}$  CP/MAS NMR spectrum of  $\text{Zn}_4\text{O}(\text{BDC-NH}_2)_{1.2}(\text{BDC})_{1.8}\text{-Pd}$ .

### 3.1.8 Optical microscopy

Optical microscopy of  $\text{Zn}_4\text{O}(\text{BDC-NH}_2)_{1.2}(\text{BDC})_{1.8}$ ,  $\text{Zn}_4\text{O}(\text{BDC-NH}_2)_{1.2}(\text{BDC})_{1.8}$ -Imine,  $\text{Zn}_4\text{O}(\text{BDC-NH}_2)_{1.2}(\text{BDC})_{1.8}$ -Pd was carried out using a Leica optical microscope. The as-synthesized samples were dispersed onto a glass plate for imaging.

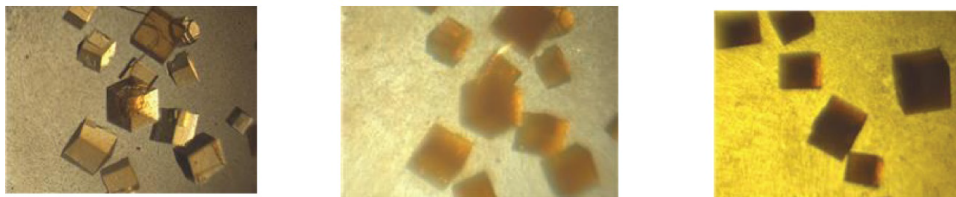


Figure 3.29: Optical microscopy of  $\text{Zn}_4\text{O}(\text{BDC-NH}_2)_{1.2}(\text{BDC})_{1.8}$ ,  $\text{Zn}_4\text{O}(\text{BDC-NH}_2)_{1.2}(\text{BDC})_{1.8}$ -Imine,  $\text{Zn}_4\text{O}(\text{BDC-NH}_2)_{1.2}(\text{BDC})_{1.8}$ -Pd, from left to right.

### 3.1.9 Catalytic Testing: Experimental Setup

In a 25 mL Schlenk flask, 1-bromo-3,5-methoxybenzene (0.434 g, 2 mmol), 4-vinylanisole (0.401 mL, 3 mmol), triethylamine (0.42 mL, 3 mmol), tetra-*n*-butylammonium bromide (0.32 mg, 1 mmol), MOF (20 mg), dodecane (1.0 mmol, inert internal standard) were added to DMA (6 mL). After rapidly stirring for 5 minutes, the reaction was heated to 120°C for 12 hours and was monitored via GC-MS.

Experiments with a palladium homogeneous catalyst used the following procedure:

In a 25 mL Schlenk flask, 1-bromo-3,5-methoxybenzene (0.434 g, 2 mmol), 4-vinylanisole (0.401 mL, 3 mmol), triethylamine (0.42 mL, 3 mmol), tetra-*n*-butylammonium bromide (0.32 mg, 1 mmol),  $(\text{MeCN})_2\text{Pd}(\text{Cl})_2$  (10 mol%), dodecane (1.0 mmol, inert internal standard) were added to DMA (6 mL). After

rapidly stirring for 5 minutes, the reaction was heated to 120°C for 12 hours and was monitored via GC-MS.

### 3.1.10 Determination of Catalytic Activity: GC-MS

**Instrument description.** GC-MS measurements were carried out using an Agilent Model 7683 Autosampler, 6890 Gas Chromatograph, and 5975 Inert Mass Selective Detector in the Electron Impact (EI) mode. EI energy was set to 70 eV. Data collection was controlled using MSD Enhanced Chemstation software (Agilent). Separation was carried out on an Agilent HP5-MS column with dimensions 30 m×250 m×0.25 m. Ultra High Purity Grade He (Airgas) was used as carrier gas with the flow set to 0.8 mL/min in constant flow mode.

**Data collection parameters.** 1 L of sample dissolved in dichloromethane (Fisher) was injected using a split ratio of 20:1, with the inlet temperature set to 280°C. The initial oven temperature was set to 45°C for 1 minute followed by a 30°C/min ramp to a final temperature of 300°C which was maintained for 3 min. A 4.5 min solvent delay was used. The MSD was set to scan the 40 — 1050 m/z range.

**Data analysis.** Mass Spectrometric data was analyzed using the MSD Enhanced Chemstation software. Product spectra were identified by comparison of the measured fragmentation patterns to those found in the NIST 08 Mass Spectral Library.

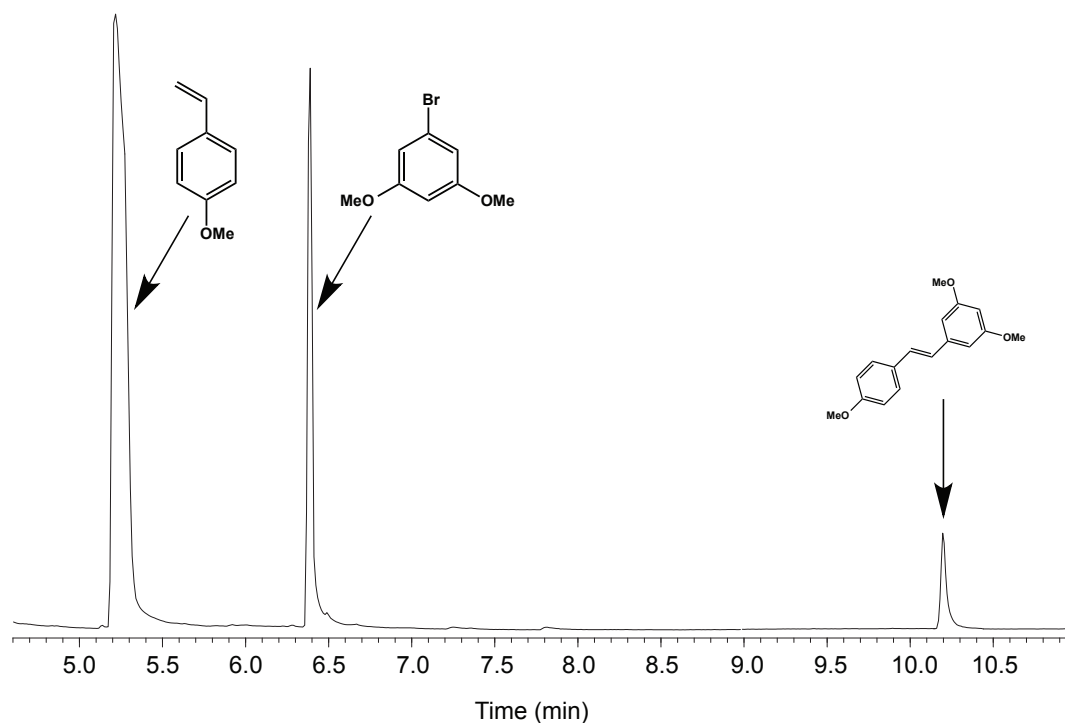


Figure 3.30: GC-MS of pure reactants and product for Heck coupling to establish retention times.

To determine the retention times of the isomers of resveratrol trimethyl ether, a sample of trans-resveratrol trimethyl ether was placed under U. V. irradiation (294 nm for 60 mins). GC-MS experiments of the resveratrol trimethyl ether was performed both before and after irradiation and shown in Figures 3.31 and 3.32, respectively.

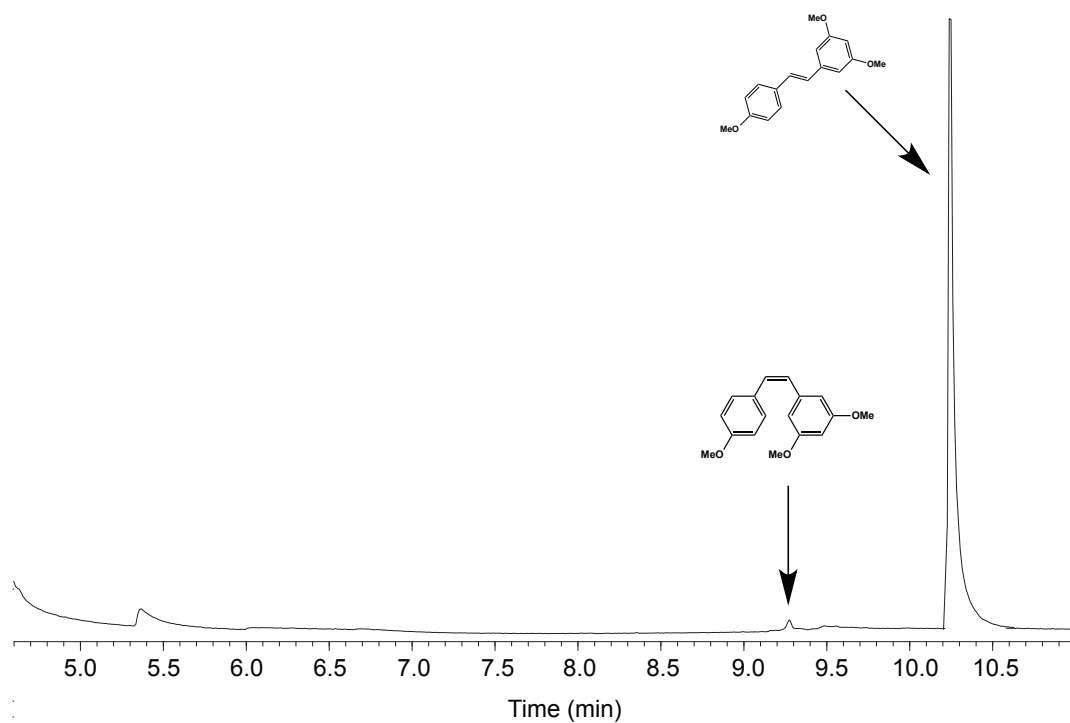


Figure 3.31: GC-MS of resveratrol trimethyl ether before U.V. irradiation (294 nm for 60 min).

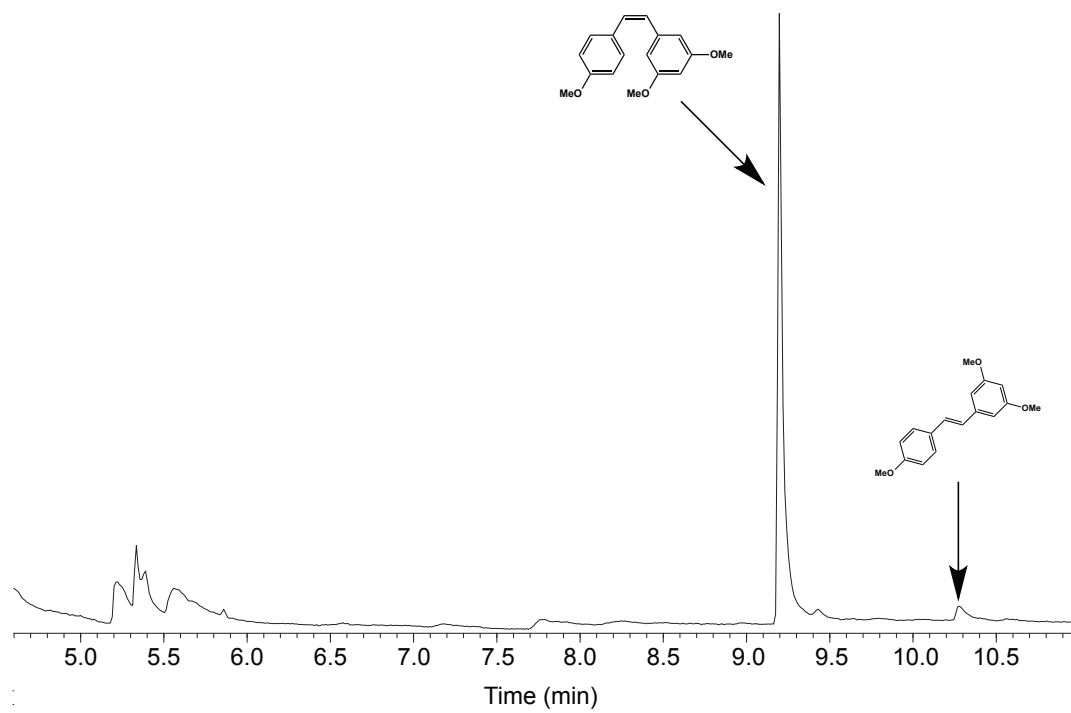


Figure 3.32: GC-MS of resveratrol trimethyl ether after U.V. irradiation.

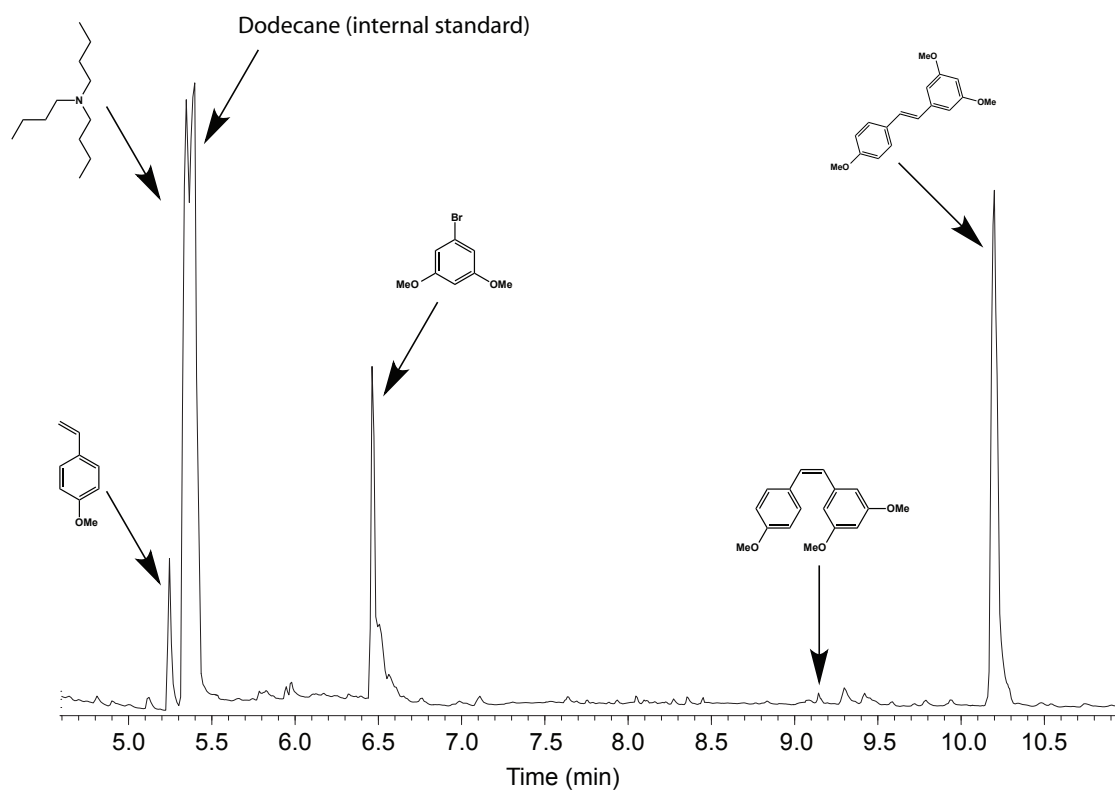


Figure 3.33: GC-MS of Heck coupling reaction to synthesize resveratrol trimethyl ether.

### 3.1.11 Catalyst Results and Recycling Experiments

The yield and selectivity of all MOFs and a homogeneous palladium catalyst are shown in Figure 3.34. We can see that some MOFs show higher yield and selectivity than the homogeneous catalyst.

Catalyst used	Yield (%)	Trans to cis ratio in product
$\text{Zn}_4\text{O}(\text{BDC-NH}_2)_{0.6}(\text{BDC})_{2.4}$	$99.3 \pm 0.02$	105.9 : 1
$\text{Zn}_4\text{O}(\text{BDC-NH}_2)_{1.2}(\text{BDC})_{1.8}$	$89.7 \pm 1.7$	81.9 : 1
$\text{Zn}_4\text{O}(\text{BDC-NH}_2)_{1.8}(\text{BDC})_{1.2}$	$75.5 \pm 1.4$	64.8 : 1
$\text{Zn}_4\text{O}(\text{BDC-NH}_2)_{2.4}(\text{BDC})_{0.6}$	$33.4 \pm 3.8$	53.9 : 1
$\text{Zn}_4\text{O}(\text{BDC-NH}_2)_3$	$15.5 \pm 1.6$	46.6 : 1
$(\text{MeCN})_2\text{Pd}(\text{Cl})_2$	$92.9 \pm 0.9$	58.5 : 1

Figure 3.34: Yield and selectivity for MOF and homogeneous catalysts.

Two MOFs [ $\text{Zn}_4\text{O}(\text{BDC-NH}_2)_{0.6}(\text{BDC})_{2.4}\text{-Pd}$  and  $\text{Zn}_4\text{O}(\text{BDC-NH}_2)_3\text{-Pd}$ ] were tested for recyclability to ensure that our frameworks maintain high yield after repeated catalytic cycles. As seen in Figure 3.35, high catalytic activity and selectivity is maintained for 10 cycles.



Framework used	Average Yield for 10 cycles (%)	Average trans to cis ratio in product
$\text{Zn}_4\text{O}(\text{BDC-NH}_2)_{0.6}(\text{BDC})_{2.4}\text{-Pd}$	$99.3 \pm 0.002$	$105.8 \pm 6.3$
$\text{Zn}_4\text{O}(\text{BDC-NH}_2)_3\text{-Pd}$	$15.5 \pm 1.6$	$46.5 \pm 2.5$

Figure 3.35: Average yield and trans to cis ratio of product for two MOFs after 10 catalytic cycles.

### 3.1.12 Catalyst control and poisoning results

Control studies were performed to test that our metalated MOFs are the catalytically active species. Heck coupling reactions were run without any MOF present and with unmetalated MOFs to ensure that our frameworks without Pd are not catalytically active. As seen in Figure 3.36, no catalytic conversion was observed if MOF is omitted or an unmetalated MOF is used. Reaction conditions, other than omitted species, are analogous to those of other catalytic runs, namely mixing MOF (20 mg), DMA (6 mL), 1-bromo-3,5-methoxybenzene (0.434 g, 2 mmol), 4-vinylanisole (0.401 mL, 3 mmol), triethylamine (0.42 mL, 3 mmol), tetra-n-butylammonium bromide (0.32 mg, 1 mmol), and dodecane (1.0 mmol, inert internal standard). This mixture was stirred rapidly for 5 minutes before heating to 120°C and monitoring the reaction via GC-MS.

Catalyst poisoning experiments were performed to test that our metalated MOFs have a single site Pd catalyst and that Pd nanoparticles or aggregates have not formed during catalyst synthesis. Heck coupling reactions were run using  $\text{Zn}_4\text{O}(\text{BDC-NH}_2)_{0.6}(\text{BDC})_{2.4}\text{-Pd}$  with the addition of either Hg(0) or  $\text{PPh}_3$ . As seen in Figure 3.37, no change in catalytic conversion was observed if Hg(0) is added to our reaction mixture. Figure 3.38 shows immediate drop-off of catalytic activity followed by cessation of all catalytic activity.

Reaction conditions are analogous to those of other catalytic runs, namely mixing MOF (20 mg), DMA (6 mL), 1-bromo-3,5-methoxybenzene (0.434 g, 2 mmol), 4-vinylanisole (0.401 mL, 3 mmol), triethylamine (0.42 mL, 3 mmol), tetra-n-butylammonium bromide (0.32 mg, 1 mmol), and dodecane (1.0 mmol, inert internal standard). For Hg(0) poisoning experiments, 0.25 mL Hg(0) was added to the reaction mixture and for  $\text{PPh}_3$  poisoning experiments, 80 mg of  $\text{PPh}_3$  was added to the reaction mixture. These mixtures were stirred rapidly for 5 minutes before heating to 120 °C and monitoring the reaction via GC-MS.

Framework used	Yield (%) Unmetalated MOF	Yield (%) MOF omitted
$\text{Zn}_4\text{O}(\text{BDC-NH}_2)_{0.6}(\text{BDC})_{2.4}$	0.0	0.0
$\text{Zn}_4\text{O}(\text{BDC-NH}_2)_{1.2}(\text{BDC})_{1.8}$	0.0	0.0
$\text{Zn}_4\text{O}(\text{BDC-NH}_2)_{1.8}(\text{BDC})_{1.2}$	0.0	0.0
$\text{Zn}_4\text{O}(\text{BDC-NH}_2)_{2.4}(\text{BDC})_{0.6}$	0.0	0.0
$\text{Zn}_4\text{O}(\text{BDC-NH}_2)_3$	0.0	0.0

Figure 3.36: Reaction yields of Heck coupling after omission of MOF or using unmetalated MOF. All measurements have an uncertainty of 1 %

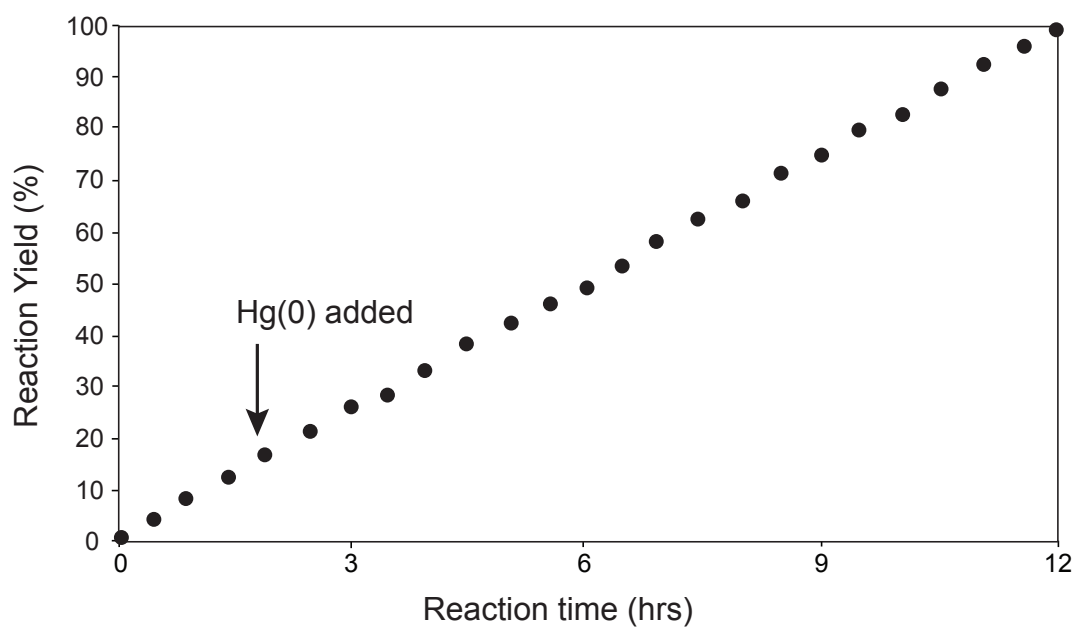


Figure 3.37: Reaction progress shows no change after  $\text{Hg}(0)$  is added to reaction mixture.

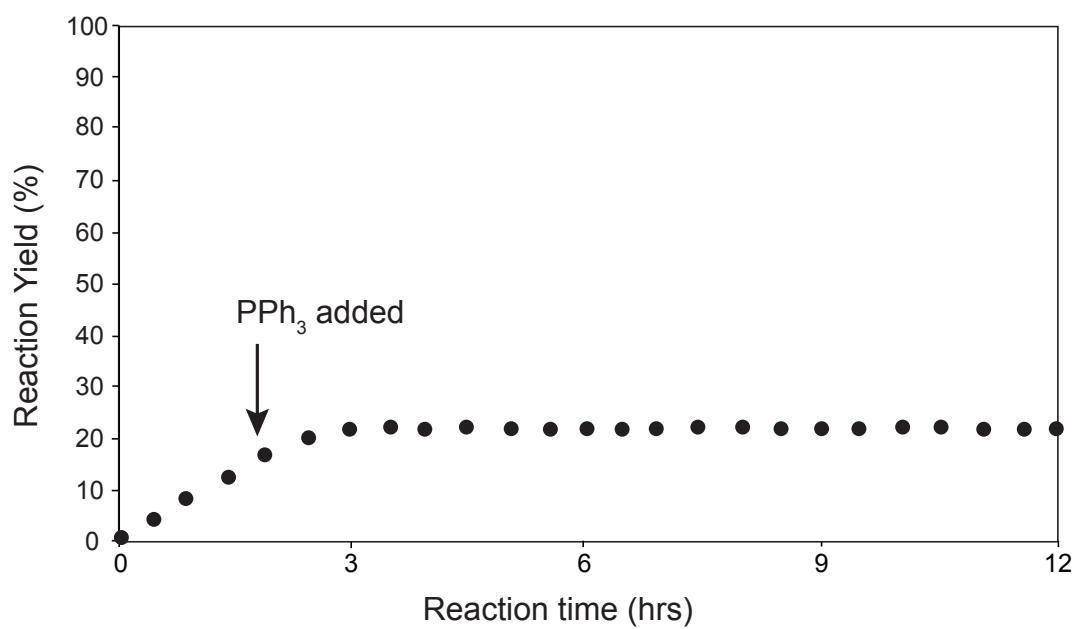


Figure 3.38: Reaction progress shows loss of catalytic activity after PPh<sub>3</sub> is added to reaction mixture.

### 3.1.13 ICP-AES of reaction product

Samples of the reaction product were submitted to USC to determine palladium leaching after the Heck coupling reaction had occurred. ICP-AES (standard deviation = 2.8%) indicated leaching was within the experimental error of the experiment and we conclude that no leaching occurred during the Heck coupling reaction.

### 3.1.14 X-ray photoelectron spectroscopy (XPS)

X-ray photoelectron spectroscopy (XPS) was employed to investigate the oxidation state of the Pd in  $\text{Zn}_4\text{O}(\text{BDC-NH}_2)_{1.2}(\text{BDC})_{1.8}\text{-Pd}$  and  $\text{Zn}_4\text{O}(\text{BDC-NH}_2)_3\text{-Pd}$ . In both samples only photoelectrons corresponding to  $\text{Pd}^{2+}$  are observed prior to catalysis, as expected for a square planar complex (Figure 3.33). However, after catalytic tests, XPS reveals both MOF samples contain  $\text{Pd}^{2+}$  and  $\text{Pd}^0$ , indicating that during the reaction,  $\text{Pd}^{2+}$  is reduced (Figure 3.39). This reduction is also observed in a color change from purple to black in each MOF sample. XPS was performed using a Kratos AXIS Ultra DLD (acquired under NSF CRIF:MU award number 0840531) with the charge neutralizer on. The finely powdered samples were supported using non-conductive double-sided tape. Spectra were analyzed using CasaXPS, fitting the peak areas to a Gaussian/Lorentzian (GL(30)) product form lineshape ( $m = p/100$ , in which  $p = 30$ ) (Figure 3.39(inset)). Pd 3d spectra were fitted and plotted using the GL(30) lineshape.

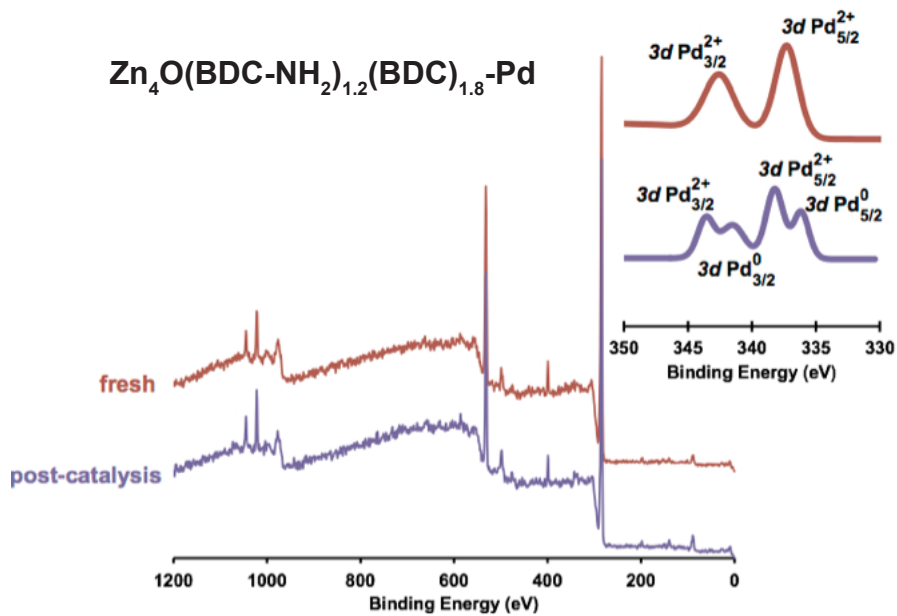
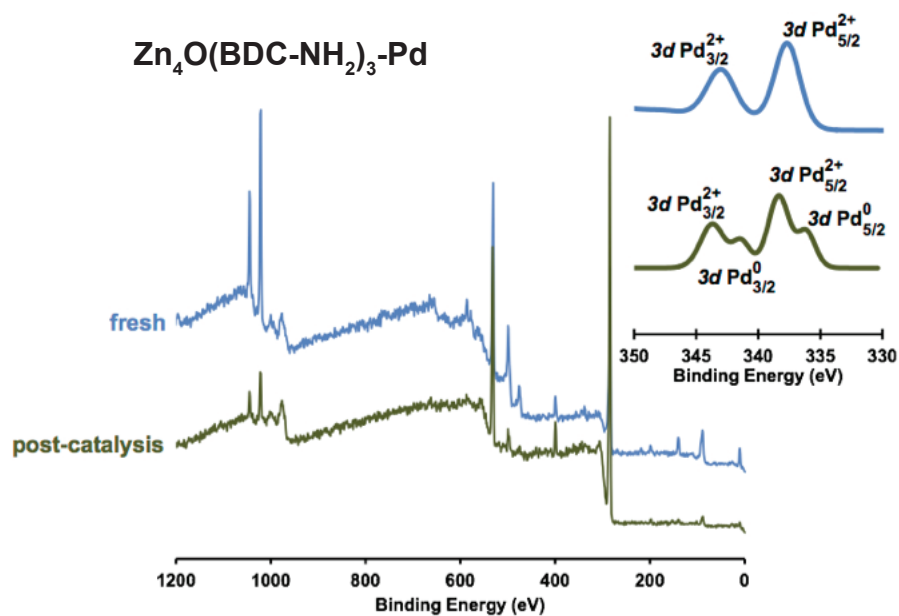


Figure 3.39: XPS Spectra of  $\text{Zn}_4\text{O}(\text{BDC-NH}_2)_3\text{-Pd}$  and  $\text{Zn}_4\text{O}(\text{BDC-NH}_2)_{1.2}(\text{BDC})_{1.8}\text{-Pd}$ .

## CHAPTER 4

# Epoxidation of Alkenes with Molecular Oxygen Catalyzed by a Manganese Porphyrin-Based Metal-Organic Framework

Here, MOFs are extended crystalline structures comprising metal clusters joined by organic links. [101,130] Due to the tunability of the reticular framework, MOFs may be designed and synthesized for specific catalytic reactions. Heterogenous MOF catalysis [46,131] was demonstrated in a number of reactions including hydrogenation, [132] oxidation, [133] and Knoevenagel condensations. [43] Recently, MOFs with metalloporphyrin linkers have been synthesized and their catalytic applications explored. [134–136] Industrially-viable catalytic MOFs are still unknown due to framework degradation upon exposure to harsh conditions. [137–139]

Epoxidation reactions are important to the chemical industry as oxides of small alkenes are produced in million ton quantities each year and are used as starting points for the production of common chemicals such as polyether polyol and ethylene glycol. [57,140] The catalysis of epoxidation reactions at mild conditions using molecular oxygen would be an important development. This study demonstrates the epoxidation of several alkenes with molecular oxygen by a manganese porphyrin containing MOF (Figure 4.1).

Molecular oxygen, commonly used in industrial catalysis, is an ideal oxidant for epoxidations due to its low cost and environmentally friendly nature. [55] Earlier studies involving homogenous epoxidation of alkenes using manganese porphyrin



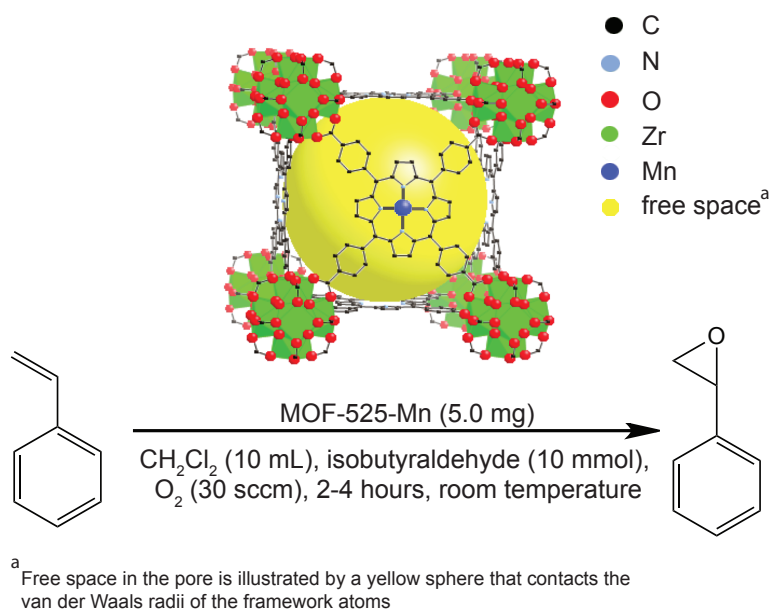


Figure 4.1: Epoxidation of styrene using MOF-525-Mn and molecular oxygen.

show high reactivity when using molecular oxygen as the oxidant. [141] While epoxidations in MOFs using molecular oxygen have been reported, [142] thus far, only low conversion rates and leaching of embedded catalysts has been shown. This article details a zirconium MOF with manganese porphyrin active site which uses molecular oxygen for enhanced catalytic conversion rates and decreased leaching of catalytic species during epoxidation.

Heterogeneous catalysts eliminate the need for steps to separate product from catalyst. The immobilization of homogeneous catalysts has been a long-standing problem in catalysis and MOFs could be useful platforms to this end. We sought to incorporate this high catalytic activity into an extended framework by selecting the MOF-525 structure for its potentially high density of catalytically active sites and the high thermal and chemical stability of the zirconium secondary building unit. [51] While other catalytically-active porphyrin-containing MOFs have been reported, [44, 143, 144] this is the first instance where a porphyrin MOF uses

molecular oxygen to catalyze epoxidation of alkenes.

The new MOF, termed MOF-525-Mn  $[\text{Zr}_6\text{O}_4(\text{OH})_4(\text{MgC}_{48}\text{H}_{24}\text{O}_8\text{N}_4\text{Cl})_3]$ , is analogous to a previously reported MOF [145] where zirconyl chloride octahydrate (12.5 mg, 0.037 mmol) and Mn(III) meso-Tetra (4-carboxyphenyl) porphine chloride (TCPP-Mn) (2.5 mg, 0.0028 mmol) was added to N,N-dimethylformamide (DMF, 10 mL) in a 20 mL scintillation vial and sonicated for 30 minutes. After sonication, acetic acid (2.5 mL) was added to the vial and heated to 65°C for 72 hours to form MOF-525-Mn. The structure of MOF-525-Mn was confirmed by coincidence of the observed PXRD with the simulated pattern (see SI) and has a pore size of 19 Å. Full manganese metal loading in the framework was confirmed by UV-Vis spectroscopy and ICP-AES. N<sub>2</sub> adsorption isotherm measurements at 77 K revealed a BET surface area of 1850 m<sup>2</sup>/g.

Reaction conditions were selected based on a previously published work involving homogenous manganese metalloporphyrins, [146] with the exception that in our heterogeneous system the MOF catalyst could easily be separated from the reaction solution at the end of the catalytic run using a simple filtration step. The epoxidation reactions were performed by bubbling O<sub>2</sub> (30 sccm) through a mixture of methylene chloride (10 mL), isobutyraldehyde (0.913 mL, 10 mmol), alkene (2 mmol), MOF (5 mg) and heptane (1.0 mmol, inert internal standard) in a reaction vessel for an extended period of time. The reaction mixture was monitored using GC-MS. The results for catalysis of different alkenes by both MOF-525-Mn and the free TCPP-Mn linker are summarized in Figure 4.2, which lists the main reaction products for each alkene reactant and corresponding reaction yields and conversion rates. Note that the size of all alkenes and sacrificial aldehyde are small enough to fit inside the MOF pore (19 Å in diameter), allowing full access to all active sites in the framework. Some yields and conversion rates for the smaller alkenes are close to maximal for MOF-525-Mn. Ethylene and propylene were not investigated in this study due to the gas-phase nature of these

reactions, requiring an entirely different reaction setup than the one used here.

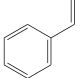
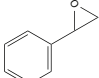
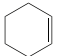
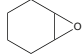
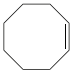
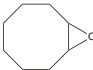
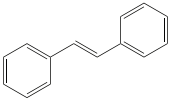
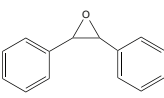
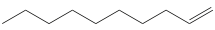
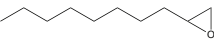
Reactant	Product	Time (h)	Conversion (%)	MOF Yield (%)	Yield free linker (%)
		2.5	99	82.8 ± 0.2	97.2 ± 0.1
		2.0	99	96.9 ± 0.1	97.1 ± 0.2
		3.0	99	96.8 ± 0.3	97.2 ± 0.1
		4.0	74	70.0 ± 0.1	84.5 ± 0.2
		4.0	75	67.9 ± 0.2	90.3 ± 0.3

Figure 4.2: Epoxidation of alkenes catalyzed by MOF-525-Mn and free TCPP-Mn with molecular oxygen and isobutyraldehyde.

In the case of styrene epoxidation, GC-MS analysis revealed a series of reaction products, with the main reaction product being styrene oxide (see Figure 4.9). Due to the large number of side products, we optimized the styrene reaction yield by varying reactor temperature. While this optimization technique could be applied to the other alkene reactions, we decided to focus on styrene and therefore analyzed the reaction kinetics to determine the main parameters of the epoxidation reaction pathway (Figure 4.3). Industrial applications of styrene epoxidation include epoxy resins and production of chemicals such as phenethyl alcohol and styrene glycol. [147]

The reactor was modeled as a constant-volume batch reactor. Rapid stirring of the reaction mixture served to ensure homogenous mixing of all components in the reactor, and the concentration of dissolved oxygen in the reaction mixture was assumed constant due to the large and continuous flux of oxygen gas into

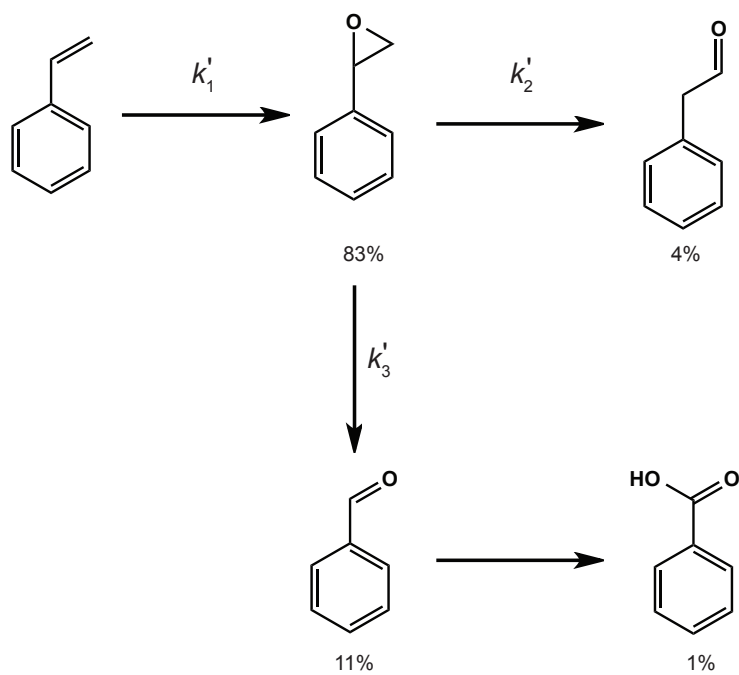


Figure 4.3: Reaction pathway for the epoxidation of styrene to styrene oxide including side products. Relative yields of each species measured at equilibrium are shown as percentages.

the reaction vessel. The reaction pathway is assigned the pseudo-rate constants ( $k'_1, k'_2, k'_3$ ). The latter are assumed to follow Arrhenius behavior:

$$k'_i(T) = A_i(T)e^{-E_{a,i}/RT} \quad (4.1)$$

where  $E_{a,i}$  is the activation energy for the  $i$ -th pathway,  $R$  is the ideal gas constant,  $T$  is the temperature and  $A_i(T)$  is the pre-exponential prefactor. The pseudo-rate constant for styrene epoxidation,  $k'_1$ , is related to the inherent rate constant,  $k_1$ , according to  $k'_1 = k_1 [\text{O}_2]$ , where  $[\text{O}_2]$  is the concentration of oxygen dissolved in the solvent.

The apparent rate constants and reaction orders were computed over the temperature range 293–329 K by fitting the decline in styrene concentration over time (see SI section for details of the procedure). The pseudo-rate constants at different temperatures were used to derive the activation energy of the reaction from a fit to 4.1. The temperature dependence of the reaction pseudo-rate constants for MOF-525-Mn was calculated from experimental data. A linearized Arrhenius plot showing the fit over the temperature range 293–329 K is found in Figure 4.4. The styrene epoxidation reaction was found to be first order with respect to styrene, and the activation energy for the epoxidation of styrene was found to be  $42.6 \pm 5.7$  kJ/mol. This activation energy agrees with calculated theoretical values within experimental error. [148] (We are unaware of any experimentally measured values for  $E_a$  reported in the literature at time of writing.) The reaction order for this heterogeneous catalyst is in agreement with published results from homogeneous manganese porphyrin systems. [149–151] This result suggests that the manganese porphyrin heterogeneous catalyst likely operates according to a mechanism similar to its homogeneous counterpart.

The heterogeneous nature of the epoxidation reaction was confirmed by filtration. After the initial reaction of styrene, the MOF was filtered and fresh isobu-

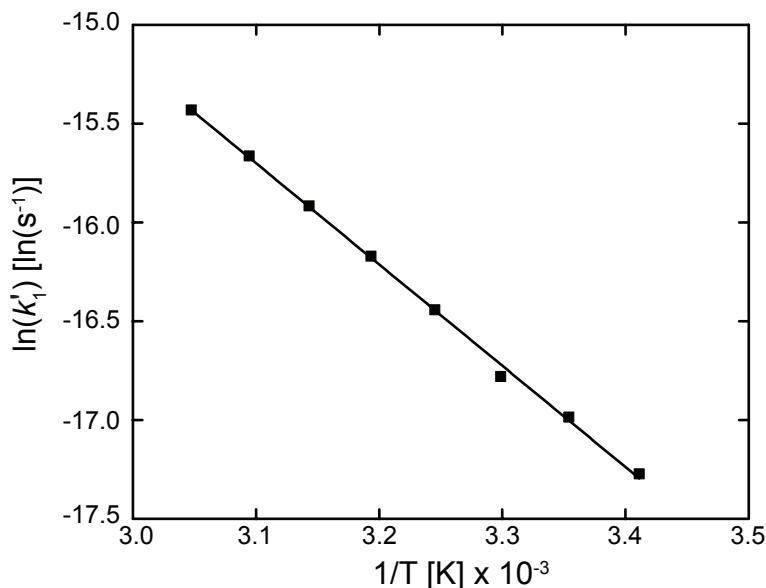


Figure 4.4: Arrhenius plot of the rate constants  $k'_1$  over the temperature range 293—329 K.

tyraldehyde and styrene were added to the filtrate. Using the filtrate, the reaction was run again under analogous conditions to the initial experiment and no catalytic conversion was observed. In addition, no catalytic conversion was observed if isobutyraldehyde, MOF-525-Mn, or metalated porphyrin were not present in the initial reaction mixture.

MOF-525-Mn showed minimal deactivation and maintained its structural stability and crystallinity at the end of the catalytic cycle, as evidenced by structural analysis with PXRD (Figure 4.5). Leeching of manganese and porphyrin from MOF-525-Mn was investigated by performing ICP-AES and elemental analysis on the product solution after filtration. We found no evidence of leeching within experimental error of these measurement techniques. XPS measurements indicated an oxidation state of Mn(III) within the framework and no change in oxidation state was observed after catalysis (Figure 4.5). To test catalytic activity after multiple runs, several cycles of epoxidations were run back-to-back using the

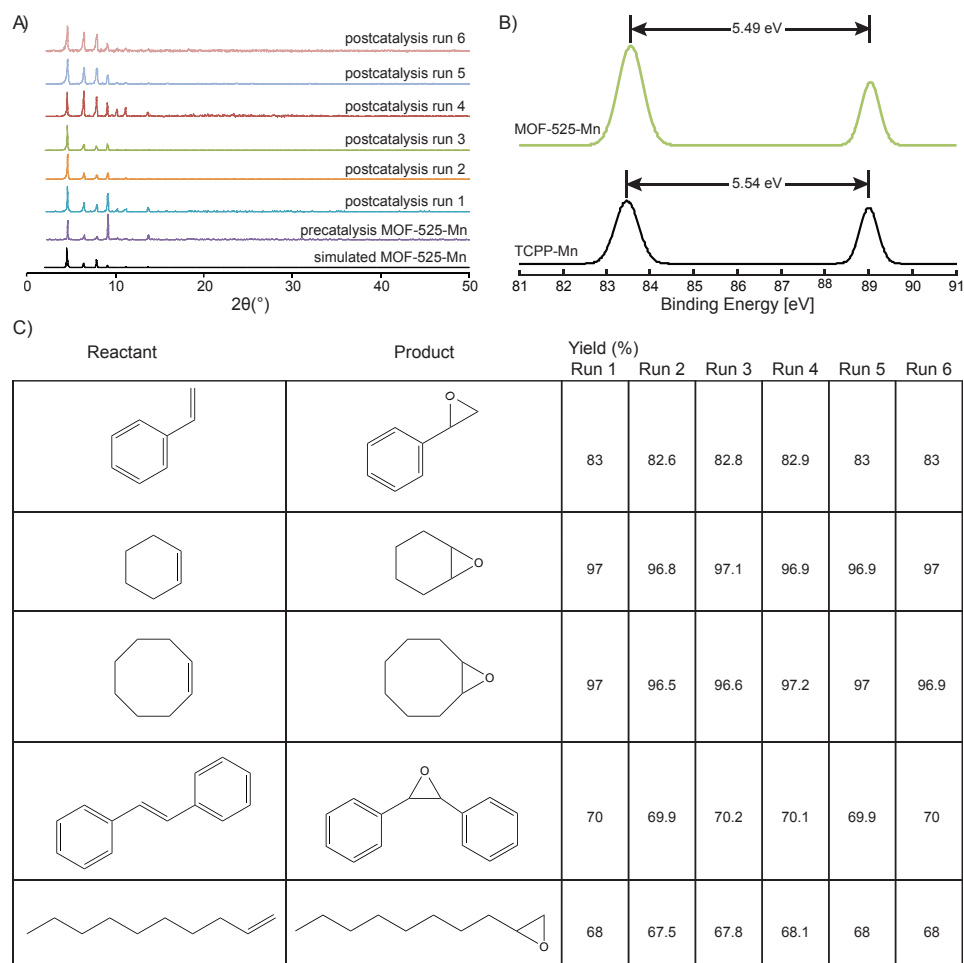


Figure 4.5: Catalytic recycling of MOF-525-Mn (a) PXRD of MOF-525-Mn after multiple catalytic runs indicates crystallinity is maintained after 6 catalytic cycles (b) XPS spectra for Mn 3s of TCPP-Mn linker and MOF-525-Mn. The data has been fit to the sum of two Gaussian, splitting is indicative of Mn(III) and does not change after catalysis (c) Product yield after multiple catalytic runs by MOF-525-Mn. High activity is maintained for all alkenes for 6 catalytic cycles.

same MOF sample, filtering it between each run while monitoring the reaction via GC-MS. High catalytic activity was maintained for all alkenes after 6 catalytic cycles (Figure 4.5).

The newly developed heterogeneous catalyst, MOF-525-Mn, based on manganese porphyrin, catalyzes epoxidation reactions of alkenes using molecular oxygen. The catalyst exhibits high yields, excellent recyclability and chemical stability with respect to different alkenes tested. The ability to use molecular oxygen in heterogeneous epoxidation reactions may lead to improved strategies for industrially viable processes.



## 4.1 Supporting Information

### 4.1.1 Materials and general procedures

All reagents unless otherwise stated were obtained from commercial sources (Frontier Scientific, Cambridge Isotope laboratories, Sigma Aldrich, TCI) and were used without further purification. Yields reported were unoptimized. All synthesis and reaction experiments were performed at the University of California, Los Angeles, Department of Chemistry and Biochemistry. Elemental analysis was performed at UC Davis Stable Isotope Facility and inductively coupled plasma atomic emission spectroscopy (ICP-AES) was performed at USC.

### 4.1.2 Synthetic procedure for MOF-525-Mn

#### 4.1.2.1 $[\text{Zr}_6\text{O}_4(\text{OH})_4(\text{MgC}_{48}\text{H}_{24}\text{O}_8\text{N}_4\text{Cl})_3]$

Zirconyl chloride octahydrate (12.5 mg, 0.037 mmol) was added to DMF (10 mL) and sonicated for 30 minutes. After sonication, Mn(III) meso-Tetra (4-carboxyphenyl) porphine chloride (TCPP-Mn) (2.5 mg, 0.0028 mmol) was added to the solution. After 10 minutes of further sonication, acetic acid (2.5 mL) was added to the solution. The solution was placed into a 20 mL scintillation vial and heated to 65°C for 72 hours. The microcrystalline powder was filtered and washed with DMF (5 x 10 mL) over a three-hour period. The DMF was replaced with acetone (5 x 30 mL) over a five-day period. Finally, the acetone was removed by heating by 120°C under vacuum (40 mTorr) for 48 hours.

### 4.1.3 Powder X-ray diffraction data

The structural integrity of activated MOF-525-Mn was confirmed by PXRD, which showed peak position analogous to MOF-525 (Figure 4.6). The PXRD patterns for synthesized and activated MOF-525-Mn are shown in Figure 4.6.

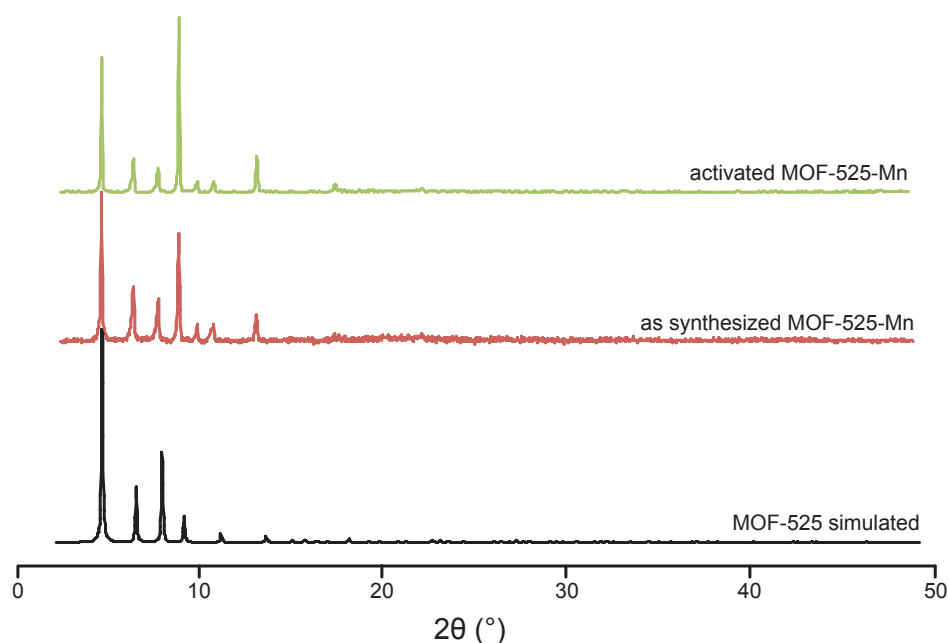


Figure 4.6: PXRD patterns of as synthesized and activated MOF-525-Mn .

#### 4.1.4 Gas adsorption at 77 K

Low-pressure gas adsorption isotherms of MOF-525-Mn were measured volumetrically and the BET surface area was found to be 1850 m<sup>2</sup>/g. The N<sub>2</sub> isotherms of MOF-525-Mn were measured using an NOVA surface area analyzer (Quantachrome Instruments). A liquid nitrogen sample bath (77 K) was used for N<sub>2</sub> measurements and the N<sub>2</sub> gas used was UHP grade. For measurement of the surface areas, the BET method was applied using the adsorption branches of the N<sub>2</sub> isotherms assuming a N<sub>2</sub> cross-sectional area of 16.2 Å<sup>2</sup>/molecule.

#### 4.1.5 ICP-AES results for metalation

To ensure the manganese metal content of the frameworks, ICP-AES was carried out, which revealed a Zr:Mn ratio of 1:0.5, confirming the porphyrin is fully metalated inside the framework.

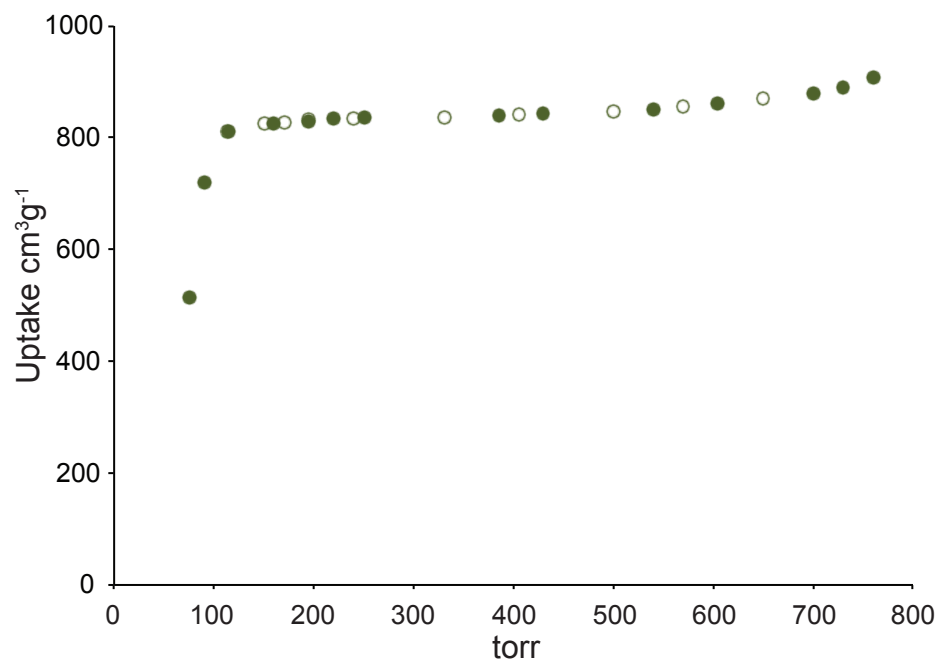


Figure 4.7: N<sub>2</sub> isotherm of MOF-525-Mn.

#### 4.1.6 UV-Vis spectroscopy

UV-Vis spectrophotometry measurements were performed on a Shimadzu UV1800 using 1 cm Hellma quartz optical cells and used to confirm the presence of manganese in MOF-525-Mn. A basic solution (1M NaOH) was used to dissolve MOF-525-Mn and the TCPP-Mn link for UV-Vis analysis. Literature values of porphyrins containing manganese show peaks at 468, 562, 596 nm. [152] These peaks are seen in both the TCPP-Mn link and MOF-525-Mn (Figure 4.8)

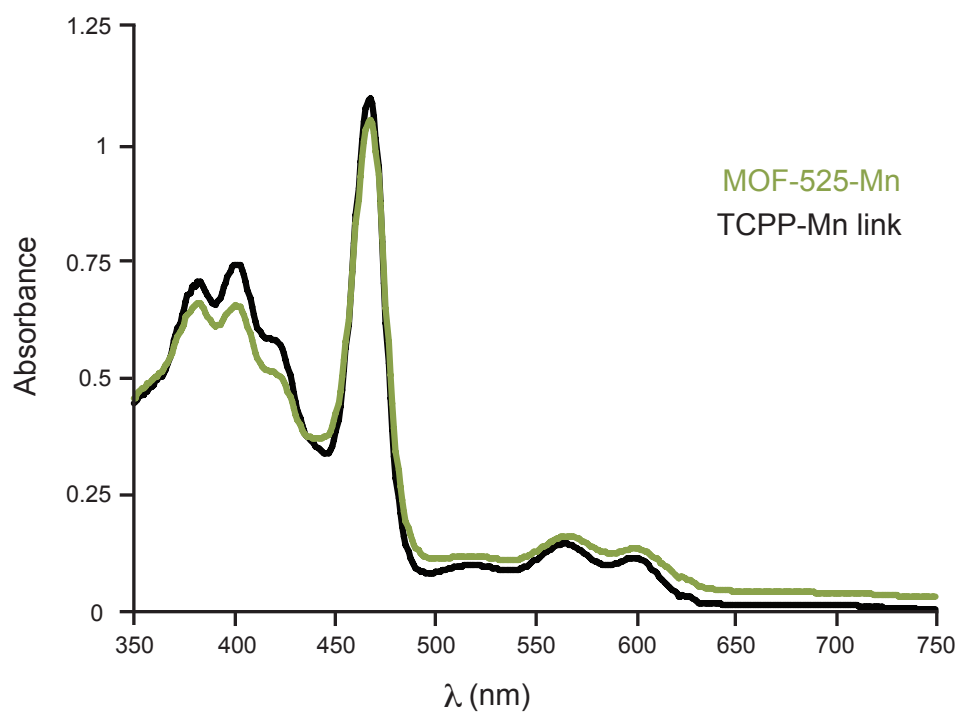


Figure 4.8: UV-Vis spectra of TCPP-Mn link and MOF-525-Mn show absorbance peaks at 468, 562, 596 nm, confirming the presence of manganese.

#### 4.1.7 X-ray photoelectron spectroscopy (XPS)

XPS was employed to investigate the oxidation state of the Mn in MOF-525-Mn and TCPP-Mn. Both pre and post-catalysis MOF-525-Mn exhibit the same Mn 3s spectrum with a splitting of 5.49 eV, corresponding to Mn(III). The TCPP-Mn linker exhibited a Mn 3s splitting of 5.54 eV which also corresponds to Mn(III). XPS was performed using a Kratos AXIS Ultra DLD (acquired under NSF CRIF:MU award number 0840531) with the charge neutralizer on. The finely powdered samples were supported using non-conductive double-sided tape. Spectra were analyzed using MATLAB, fitting the peak areas to a sum of two Gaussians.

#### 4.1.8 Catalytic Testing: Experimental Setup

In a 25 mL Schlenk flask, isobutyraldehyde (0.913 mL, 10 mmol), alkene (2 mmol), MOF-525-Mn (5 mg) and heptane (1.0 mmol, inert internal standard) were added to methylene chloride (10 mL). After rapidly stirring for 5 minutes, bubbling O<sub>2</sub> (30 sccm) was introduced and the reaction was monitored via gas chromatography-mass spectroscopy (GC-MS).

#### 4.1.9 Determination of Catalytic Activity: GC-MS

**Instrument description.** GC-MS measurements were carried out using an Agilent Model 7683 Autosampler, 6890 Gas Chromatograph, and 5975 Inert Mass Selective Detector in the Electron Impact (EI) mode. EI energy was set to 70 eV. Data collection was controlled using MSD Enhanced Chemstation software (Agilent). Separation was carried out on an Agilent HP5-MS column with dimensions 30 m x 250  $\mu$ m x 0.25  $\mu$ m. Ultra High Purity Grade He (Airgas) was used as carrier gas with the flow set to 0.8 mL/min in constant flow mode.

**Data collection parameters.** 1 L of sample dissolved in dichloromethane

(Fisher) was injected using a split ratio of 20:1, with the inlet temperature set to 280°C. The initial oven temperature was set to 45°C for 1 minute followed by a 30°C/min ramp to a final temperature of 300°C which was maintained for 3 min. A 3.2 min solvent delay was used. The MSD was set to scan the 40 – 1050 m/z range.

**Data analysis.** Mass Spectrometric data was analyzed using the MSD Enhanced Chemstation software. Product spectra were identified by comparison of the measured fragmentation patterns to those found in the NIST 08 Mass Spectral Library.

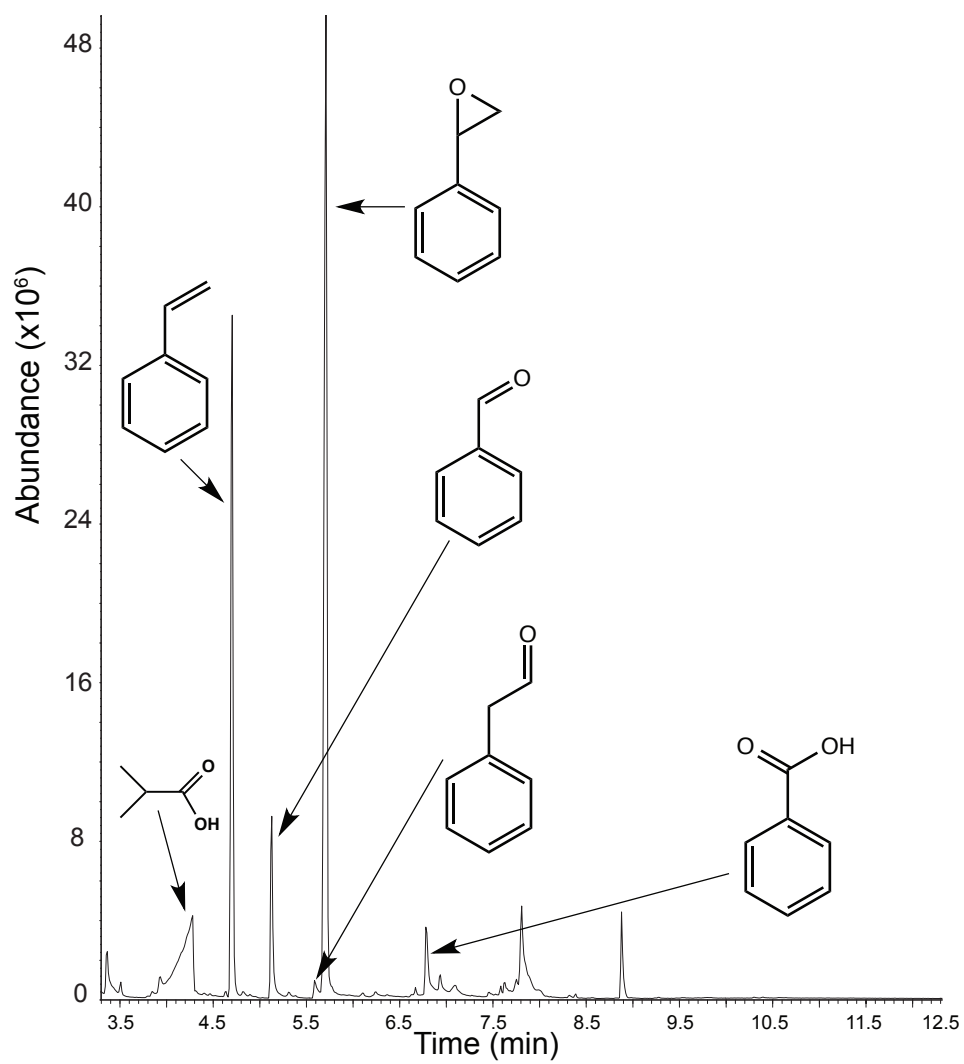


Figure 4.9: GC-MS spectrum of styrene epoxidation reaction.

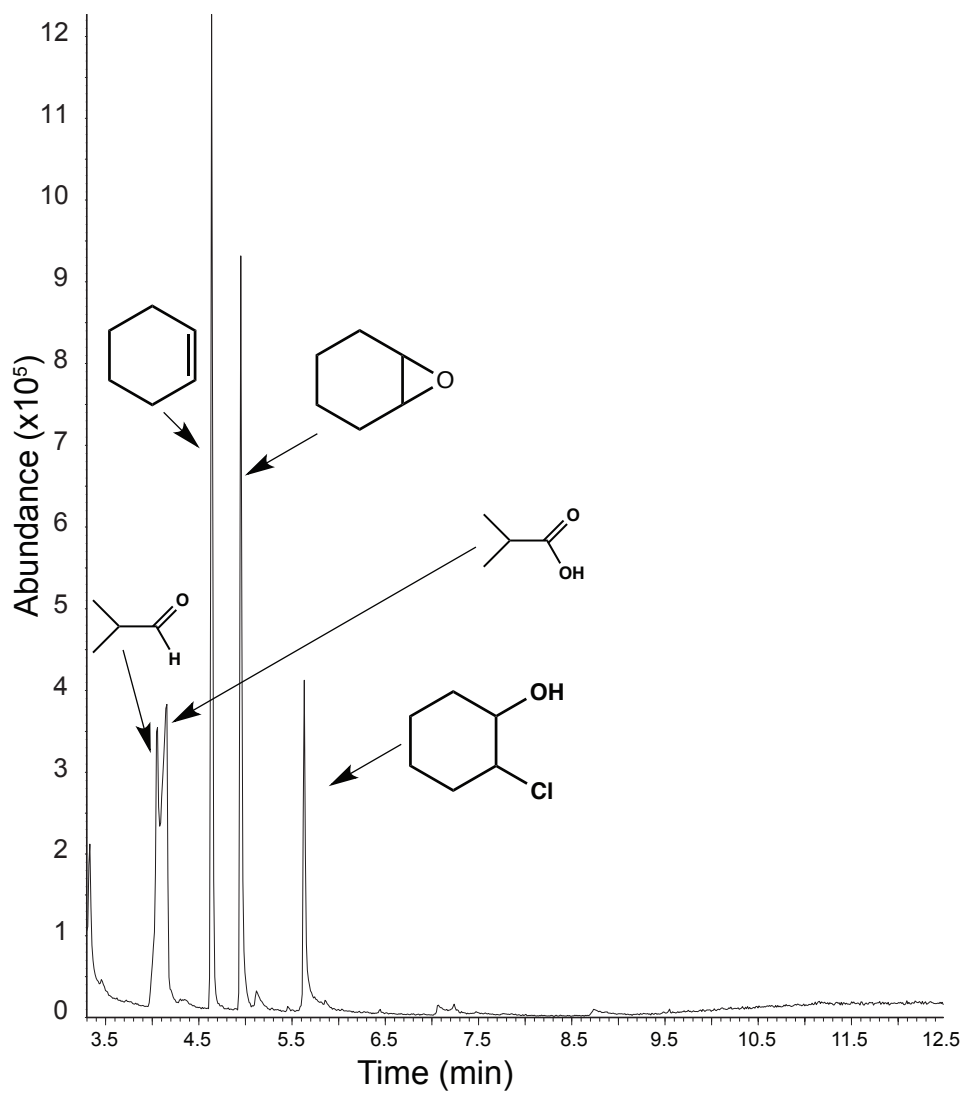


Figure 4.10: GC-MS spectrum of cyclohexene epoxidation reaction.



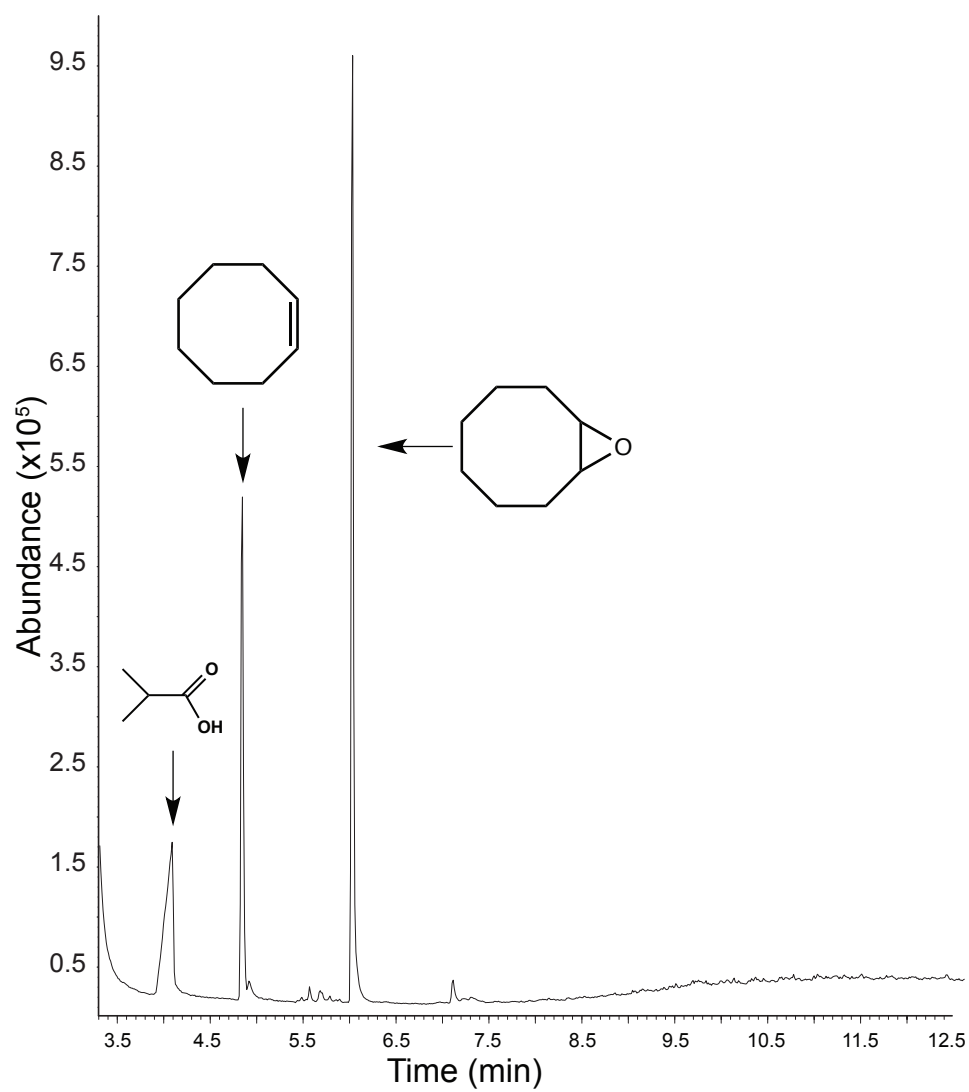


Figure 4.11: GC-MS spectrum of cyclooctene epoxidation reaction.

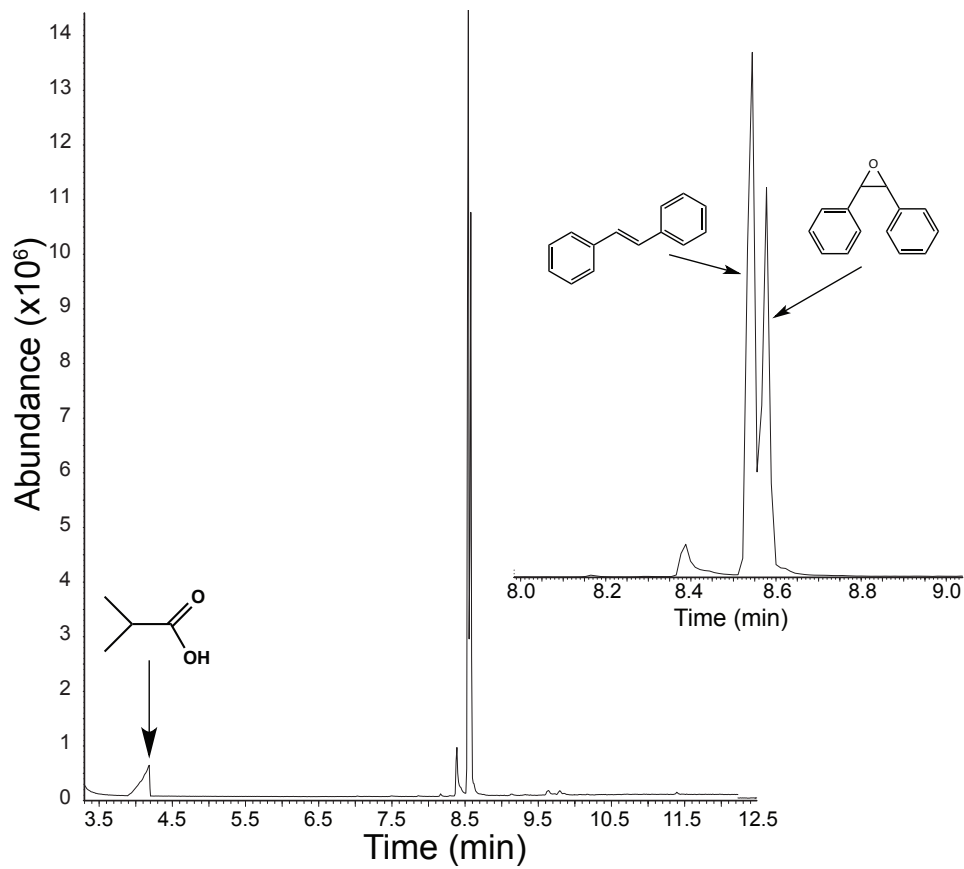


Figure 4.12: GC-MS spectrum of trans-stilbene epoxidation reaction.

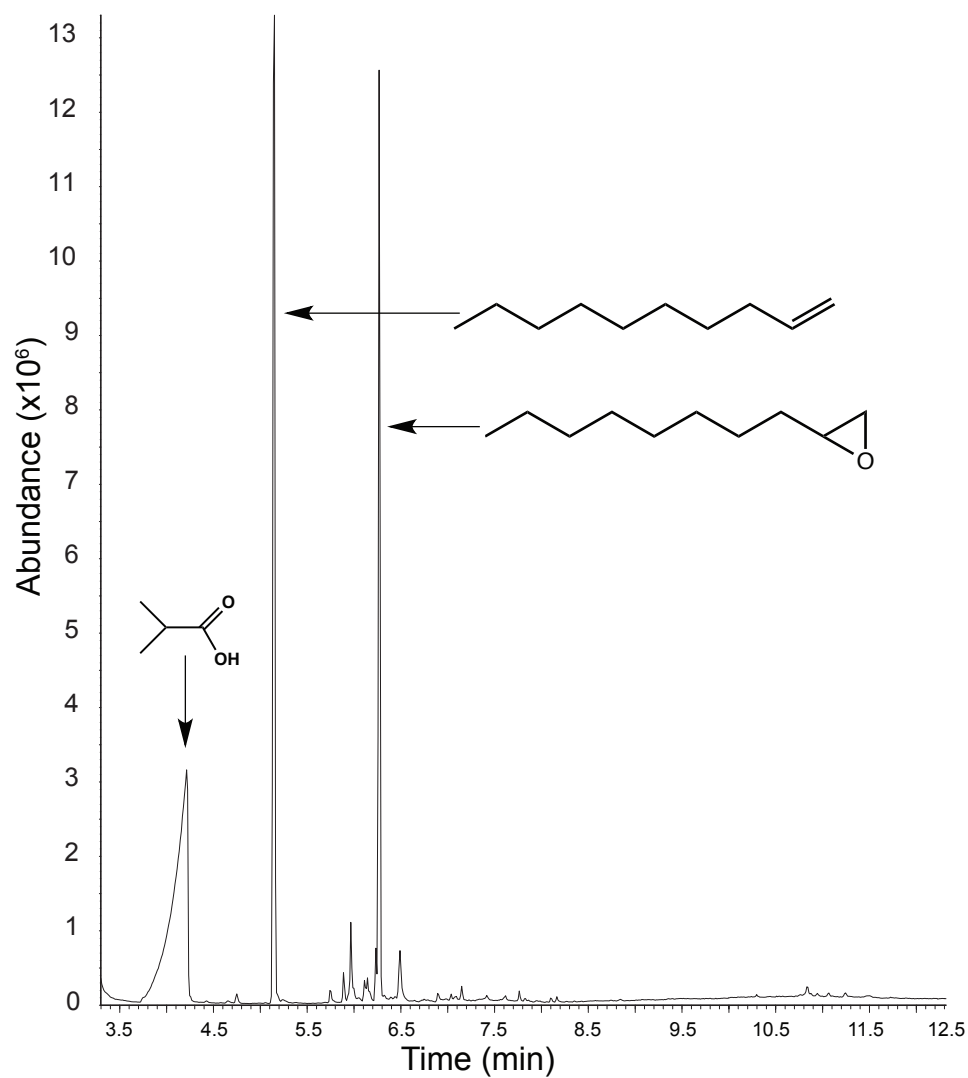


Figure 4.13: GC-MS spectrum of decene epoxidation reaction.

#### 4.1.10 Catalyst control results

Control studies were performed to test that MOF-525-Mn is the catalytically active species and that sacrificial aldehyde, isobutyraldehyde, is necessary. Epoxidation reactions were also run with unmetalated MOF-525 to ensure that unmetalated MOF-525 is not catalytically active. As seen in Figure 4.14, no catalytic conversion was observed if MOF-525-Mn or isobutyraldehyde are omitted or if un-

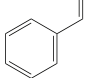
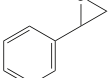
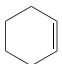
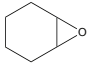
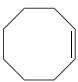
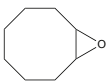
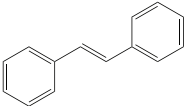
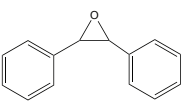
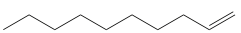
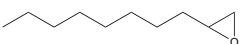
Reactant	Product	Yield (%) no MOF-525-Mn	Yield (%) no isobutyraldehyde	Yield (%) Unmetalated MOF-525
		0.0	0.0	0.0
		0.0	0.0	0.0
		0.0	0.0	0.0
		0.0	0.0	0.0
		0.0	0.0	0.0

Figure 4.14: Reaction yields of epoxidation after omission of MOF-525-Mn and isobutyraldehyde or using unmetalated MOF-525 .

metalated MOF-525 is used. Reaction conditions, other than omitted species, are analogous to those of other catalytic runs, namely mixing MOF (5 mg), methylene chloride (10 mL), isobutyraldehyde (0.913 mL, 10 mmol), alkene (2 mmol). This mixture was stirred rapidly for 5 minutes before adding bubbling O<sub>2</sub> (30 sccm) and monitoring the reaction via GC-MS.

#### 4.1.11 Elemental analysis and ICP-AES of reaction product

Samples of the reaction product were submitted to UC Davis Stable Isotope Facility and USC to determine porphyrin and manganese leeching, respectively, after the epoxidation reaction had occurred. Both elemental analysis (standard deviation = 0.3%) and ICP-AES (standard deviation = 2.8%) indicated leeching was within the experimental error of the experiment and we conclude that no leeching occurred during the epoxidation reaction.

#### 4.1.12 Reaction Rate Kinetics and Fitting of GC-MS data in MATLAB

The reaction vessel is modeled as a constant volume batch reactor due to the absence of liquid streams entering or exiting the vessel. Though oxygen is bubbled constantly through the liquid mixture, this was found to cause minimal volume change from O<sub>2</sub> induced evaporation. Under these assumptions, the general mass balance for styrene (denoted with subscript A) in the reaction vessel is

$$\frac{dC_A}{dt} = \dot{r}_A \quad (4.2)$$

where  $\dot{r}_A$  is the rate of generation of styrene. Since the styrene participates in three reactions (conversion into styrene oxide, benzaldehyde, and benzeneacetaldehyde, see Figure 4.3 in the main text) the rate term has three contributions

$$\dot{r}_A = -k_1 C_A^\alpha [O_2]^\beta - k_2 [C_A]^\gamma - k_3 [C_A]^\delta \quad (4.3)$$

where the rate constants  $k_1$ ,  $k_2$ , and  $k_3$  apply to each of the three major reactions that the styrene takes part in, and  $\alpha, \beta, \gamma$ , and  $\delta$  are the reaction orders for each reaction.

In this study, the dissolved oxygen concentration [O<sub>2</sub>] is approximately constant across all trials due to the large excess of gaseous oxygen used, and is therefore incorporated into  $k_1$  (reabeled  $k_1'$ ) to form the pseudo rate equation:

$$\dot{r}_A = -k_1' C_A^\alpha - k_2 [C_A]^\gamma - k_3 [C_A]^\delta \quad (4.4)$$

Equation 4.4 was used in equation 4.2 in order to fit rate parameters to the concentration data collected for styrene. Time derivatives were computed by fitting a polynomial equation to  $C_A$  as a function of time and differentiating the resulting expression. All reactions were found to be first order with respect to

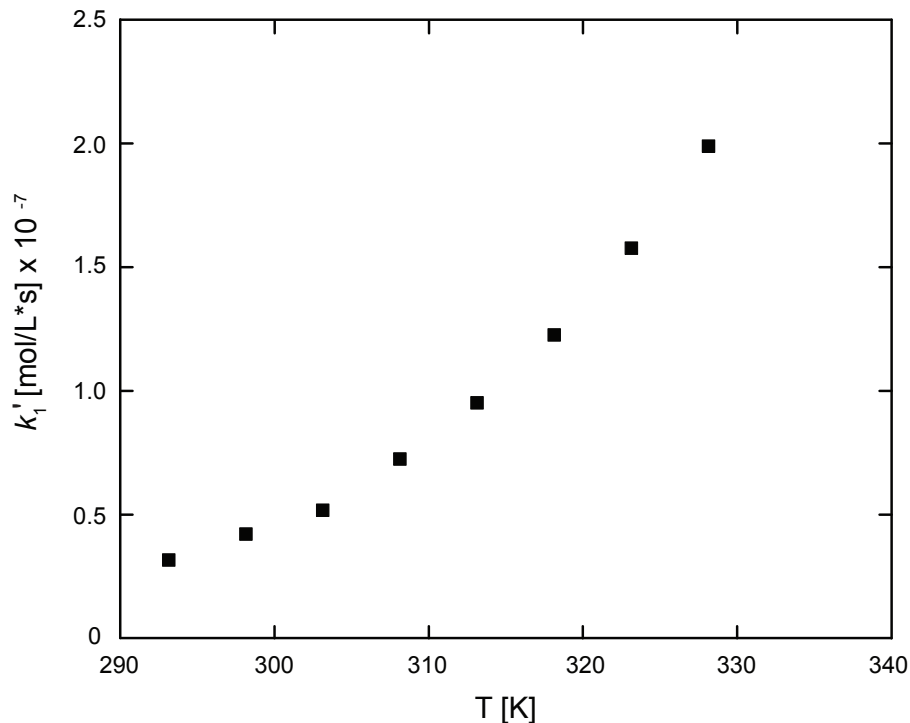


Figure 4.15: Temperature dependence of the pseudo kinetic rate constant  $k'_1(T)$  of MOF-525-Mn.

styrene by fitting experimentally measured time-course concentrations of styrene and styrene oxide with Equation 4.4. Using a multiple start-point solver for constrained gradient-based optimization (Global Optimization Toolbox, MATLAB), the rate constants ( $k'_1, k_2, k_3$ ) and reaction orders ( $\alpha, \gamma, \delta$ ) that minimized the residuals between the proposed rate model and the empirically observed rate of styrene consumption were identified. The globally optimal parameters for the data fit indicated that exponential values ( $\alpha, \gamma, \delta$ ) were equal to one (first order kinetics). The pseudo rate constants  $k'_1$  calculated by the solver at different temperatures are the values reported in the main text. An Arrhenius fit to  $k'_1$  values at different temperatures was used to report the activation energy in the main text. The temperature dependent plot of  $k'_1$  is shown in Figure 4.15.

## CHAPTER 5

### Conclusions and Future Directions

The research demonstrated in this dissertation explores several important aspects of MOFs and their use in catalysis. The azobenzene containing MOF-74 shown in Chapter 2 is the first instance of dynamic pores controlling release of cargo molecules, Figure 5.1A. This dynamic pore environment may play a major role in future MOF catalysis where molecules of interest need to controllably captured and released in catalytic systems. In addition to dynamic pore control, MOFs must be able to withstand typically harsh chemical environments often used in industrial catalysis. These necessary qualities have been demonstrated by use of a manganese porphyrin-containing framework in the epoxidation of alkenes, Figure 5.1B. In addition, this is the first instance of using molecular oxygen, the most commonly used industrial oxidant, in epoxidation by MOFs. Finally, viable MOF catalysis benefits from inherent advantages of using MOFs, namely the improvement of catalytic efficiency through varying the density of active sites and ability to introduce new catalytically active sites in frameworks. In Chapter 4, the use of the MTV principle and postsynthetic modification in frameworks show that we have the ability to enhance catalytic activity and selectivity while limiting the amount of catalyst needed, Figure 5.1C.

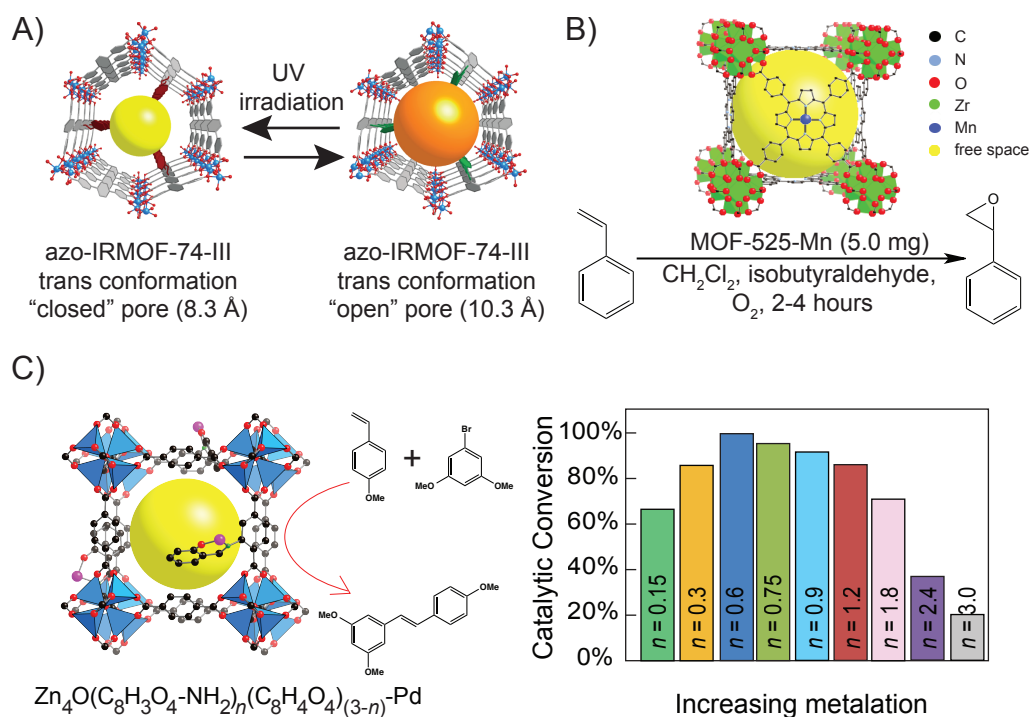


Figure 5.1: A) Schematic representation of open and closed pore azo-IRMOF-74-III B) Epoxidation of styrene by MOF-525-Mn C) Heterogeneous Heck coupling inside a Pd containing MOF with varying number of catalytic active sites.

## 5.1 Attempts to Immobilize Crabtree's Catalyst in IRMOF-74-III for Heterogeneous NMR Signal Enhancement

One area of interest for our group is utilizing a MOF to immobilize a heterogeneous catalyst, specifically for use in NMR signal amplification by reversible exchange (NMR-SABRE). Currently, SABRE is performed using a homogeneous iridium N-Heterocyclic Carbene (NHC) catalyst yielding signal enhancements up to 8100 fold. [153] The SABRE catalyst achieves this enhancement factor by transferring the polarization from para-hydrogen to a molecule of interest without any chemical modification, unlike para-hydrogen induced polarization. [154, 155] If we were



able to successfully immobilize a SABRE catalyst in a water stable MOF, this heterogeneous system would be a significant advancement in the hyperpolarization field and a step forward for catalytically active MOFs.

While there are several approaches to immobilizing catalysts inside MOFs, including cationic exchange [156], host-guest “locking” [157] and incorporating the catalyst as the organic linker [158], we decided to use a well known PSM method, formation of an imine bond, [36] to attach a modified version of the Crabtree catalyst [159] to IRMOF-74-III.

Our method is described in the Figure 5.2, but despite varying our PSM conditions, we were unable to preserve crystallinity after PSM of IRMOF-74-III. This may have been due to the fact that we were attempting to attach an active hydrogenation catalyst to our MOF. In addition, attempted hydrogenation of propylene using the amorphous material after PSM showed no catalytic activity. Catalyst and pore size may have also played a part in the unsuccessful PSM. While we specifically selected IRMOF-74-III for its large pore size and had a relatively small counter-ion with our Crabtree catalyst, perhaps the solvated catalyst was too large to properly diffuse into the pore and rearrange itself and attach to the framework. To remedy this, we would need to expand our linkers to create a larger pore cavity, as has been seen in the IRMOF-74 system, or select a different MOF that has a larger pore cavity such as MIL-101. [52]

Though we were ultimately unsuccessful in attaching a SABRE catalyst to a MOF for heterogeneous hyperpolarization, there are still several avenues that could be explored for a successful heterogeneous SABRE catalyst. One has already been discussed above and would involve expanding the MOF pore to accommodate the large homogeneous catalyst but this still involves attempting to attach an active catalyst via chemical reaction. Two other methods that may be more viable are the host-guest “locking” and cationic exchange demonstrated in other MOF systems for incorporation of homogeneous catalysts. The advantages of both are

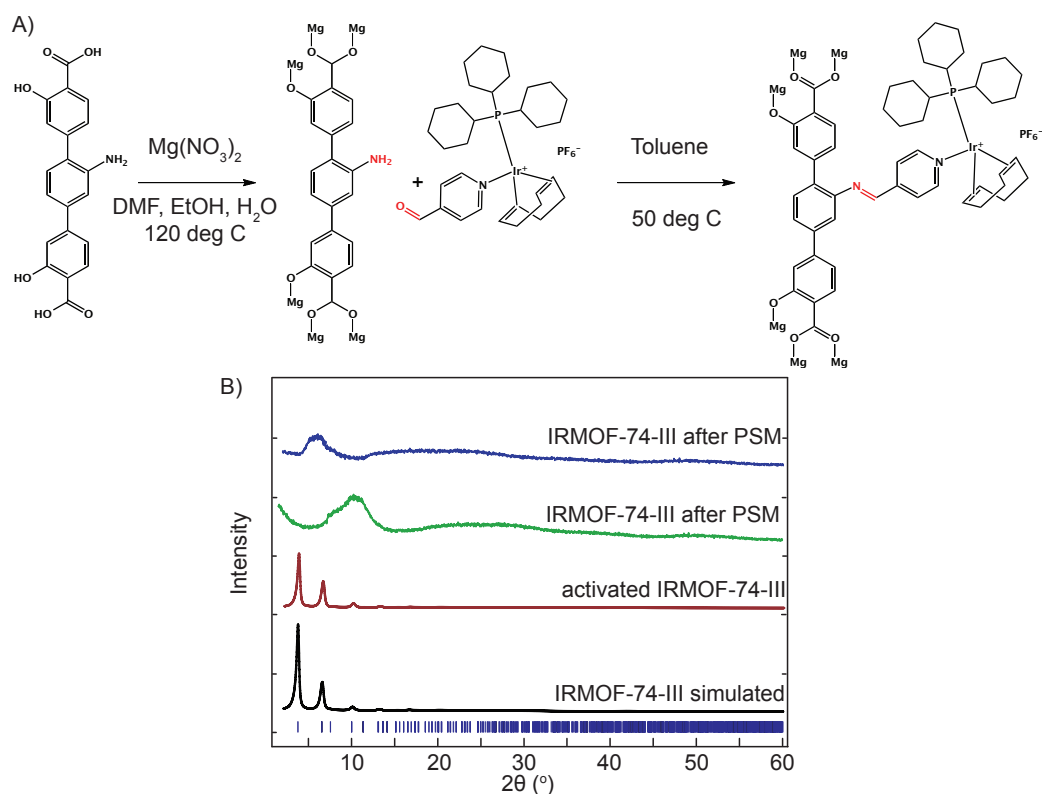


Figure 5.2: A) PSM scheme for attaching Crabtree catalyst to IRMOF-74-III B) PXRD after PSM shows loss of crystallinity in framework.

that a homogeneous catalyst can be introduced without requiring a covalent bond to be formed between catalyst and framework. This should mitigate the loss of crystallinity that was seen in our systems and still gives us room to play with the steric effects from side groups on the homogeneous catalyst. While changing these side groups could ultimately effect the catalytic activity observed from our SABRE catalyst, this is another factor to take into consideration while attempting to immobilize a homogeneous catalyst.

Another possibility for heterogeneous SABRE catalysis is to use the organic linker or MOF SBU itself as a catalyst. Recently iridium catalysts have been introduced in zirconium based MOFs [160,161] but there has yet to be a MOF where the SBU itself it made from iridium clusters. While this may be unfeasible

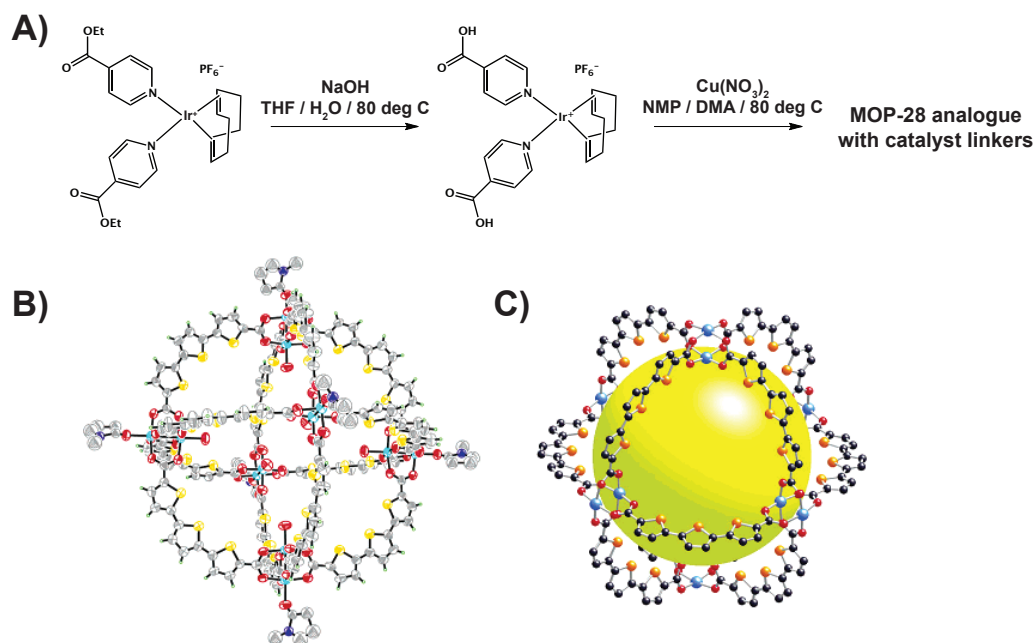


Figure 5.3: A) Synthetic scheme for NHC linker and MOP-28 analogue B) MOP-28 structure C) MOP-28 structure with yellow ball indicating free space.

due to the high activity of iridium centers, a MOF with an iridium based SBU would be ideal for this type of SABRE catalysis. In addition to using MOFs, a metal-organic polyhedra (MOP) [162] could be used with catalyst linkers as seen in Figure 5.3. While this is a feasible way to incorporate NHC iridium catalysts into a crystalline structure, the catalyst centers would all be pointing into the middle of the pore, possibly decreasing catalytic activity due to pore space constraints. Since the size of Ir complexes do play an appreciable role in SABRE activity, the idea of cation exchange to incorporate catalysts into a MOF is especially interesting. While the size of both the MOF and catalyst would have to be tuned for proper catalyst encapsulation into the superstructure, this could be accomplished either by modifying the side groups on the catalyst or modifying the linker length to accommodate a catalyst of specific size.

## 5.2 The Effect of Topologically Distinct MOFs on Alkene Epoxidation Yield

While MOF catalysis is still in its infancy, there are many future directions available for new research. One of the most intriguing aspects of MOFs is the wide array of topologies available for catalytically active MOFs. Changes in topology can effect a wide range of properties including pore size, pore aperture, density of functionalities and environment of the functionality. While these parameters have been explored in terms of gas separation and storage, [163] there is a scarcity of studies involving the effect of topology in heterogeneous MOF catalysis. Nature often finely tunes the environment of catalytic sites in enzymes using many of the same parameters highlighted above. Therefore, by using the same catalyst in different topologic environments, we can explore the possibility of catalytic optimization via different catalytic activities as well as different product selectivity for different topologies, which will likely deviate from homogeneous systems. We have already begun preliminary work on catalytic activity optimization via change in topology through the epoxidation of alkenes in MOF-545-Mn, MOF-525-Mn and PCN-224-Mn, where the effect of different topologies is being investigated in alkene epoxidation. This work builds upon the work in Chapter 4 on the epoxidation of alkenes using a manganese porphyrin based MOF, MOF-525-Mn  $[\text{Zr}_6\text{O}_4(\text{OH})_4(\text{MgC}_{48}\text{H}_{24}\text{O}_8\text{N}_4\text{Cl})_3]$ . While this project looks simply at optimization of catalytic yield as a function of topology, different frameworks can also influence selectivity of products. This has initially been seen in the oligomerization of ethylene based on the change in pore apertures in MOF-74 analogues. [58] The selectivity of linear versus branched alkene chains could be influenced largely by the topology of the heterogeneous catalysis. These two projects are both extensions of the idea that framework topology research can influence the catalytic optimization for industrially relevant reactions and are interesting new directions

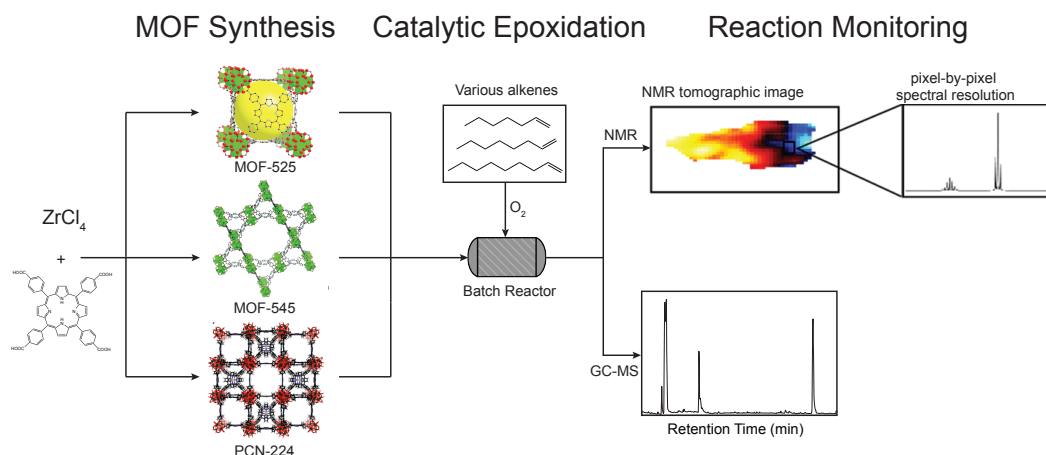


Figure 5.4: Synthesis and catalytic testing of MOF-525-Mn, MOF-545-Mn and PCN-224 for epoxidation of long chain alkenes.

forward for the research I have completed during my time at UCLA.

The work on alkene epoxidation presented in Chapter 4 will lead to the investigation of the epoxidation of longer alkene chains. With larger substrates, there may be difficulty accessing all active sites in MOF-525-Mn due to its cubic topology and small pore aperture (19 Å diameter, space group  $Pm\bar{3}m$ ). An excellent alternative would use the hexagonal topology of MOF-545 that has a large one-dimensional pore (35 Å diameter, space group  $P6/mmm$ ) or to use PCN-224 which has channel type pores (19 Å diameter, space group  $Im\bar{3}m$ ). We expect different catalytic activity from the three frameworks simply based on steric concerns and size exclusion of longer alkene chains from the MOF-525 structure. We would expect that as alkene chain length increases, the activity of the MOF-545 and PCN-224 structures would increase relative to the MOF-525 structure due to greater number of accessible catalytically active sites. To test this, we can set up a system such as the one seen in Figure 5.4, where we monitor catalytic conversion over time via GC-MS or NMR.

Current work shows that there are some differences in catalytic activity be-

Reactant	Product	MOF-525-Mn Yield (%)	MOF-545-Mn Yield (%)
		82.8	80.2
		96.9	99.5
		96.8	94.4
		70.0	97.1
		67.9	54.9

Figure 5.5: Epoxidation of alkenes using molecular oxygen in MOF-525-Mn and MOF-545-Mn.

tween the two frameworks but more work needs to be done optimizing the MOF-545-Mn reaction parameters. The yields shown in Figure 5.5 have been optimized for MOF-525-Mn; however, only preliminary data at room temperature has been collected for the MOF-545-Mn reactions. We are currently working on optimizing the MOF-545-Mn reactions as well as synthesizing and testing the activity of PCN-224. Initial attempts at synthesizing PCN-224 indicates that the framework cannot be made by starting with a metallated TCPP link. Instead an unmetallated TCPP linker must be used in the initial framework synthesis, then the framework post-synthetically modified to include the Mn metal center on the porphyrin link.

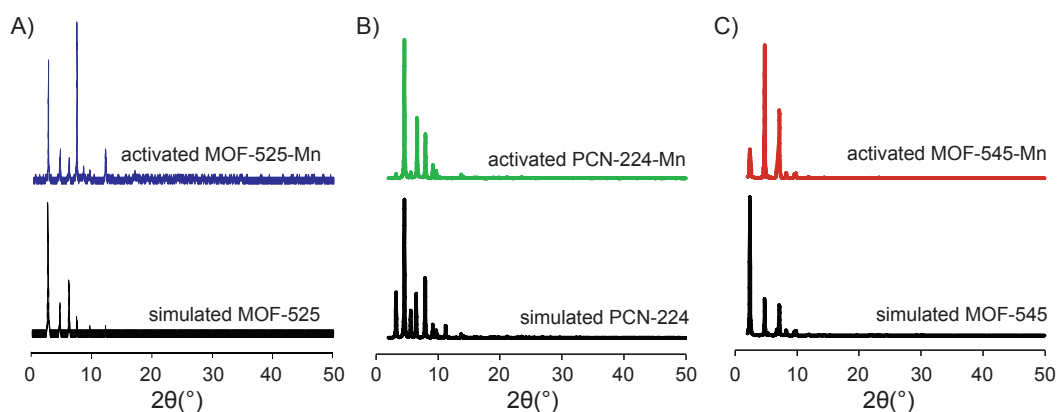


Figure 5.6: PXRD of simulated and activated A) MOF-525-Mn B) PCN-224-Mn and C) MOF-545-Mn.

We have confirmed our porphyrin MOF structures by PXRD as seen in Figure 5.6. Surface area and XPS measurements still need to be taken for MOF-545-Mn and PCN-224-Mn.

We expect MOF-545-Mn and PCN-224 to show enhanced catalytic yield as alkene size increases due to the larger space in the pore cavity of MOF-545-Mn. There may be some tradeoff in this increased free space as the isobutyraldehyde co-catalyst also needs to interact at the active site of the manganese porphyrin and there may be some optimal density of co-catalyst to active site that needs to be achieved. Discussion of optimal density of catalyst to co-catalyst within a given pore volume is beyond the scope of this thesis but these are simple experiments that can be quickly carried out on these systems to find optimal catalytic yield for epoxidations of various alkenes.

### 5.3 Bimetallic Porphyrin-based MOFs for Propylene Epoxidation

In addition to small alkene epoxidation using known structures, preliminary work on bimetallic MOF systems for propylene epoxidation was explored through collaboration with the Senkan group at UCLA. Our idea was to insert Cu and Ru porphyrin sites into the MOF-525 framework as the Senkan group has observed propylene epoxidation from mixing Cu and Ru nanoparticles. [164] We tried two approaches for incorporation of two metalated porphyrins. First, mixing pre-metalated Cu porphyrin linkers in specific ratios (Cu to unmetalated ratios of 90:10, 80:20, 60:40, and 50:50) with unmetalated linkers, synthesizing the framework, and then inserting the Ru into the unmetalated porphyrins. Second, using premetalated Cu and Ru porphyrins and then mixing the links in the initial synthesis (using the same ratios as the previous method). We observed crystalline MOF-525 with incorporation of both metals into the final structures using the second method, but observed no appreciable conversion of propylene into propylene oxide when our MOF samples were used in the Senkan group catalytic set-up. This may have been due to several factors including the two catalytic centers not being in close proximity to each other, a lack of appropriate reaction conditions for this new system, and an inability to saturate the MOF with NaCl which helped achieve higher yields in different systems. [165] Additionally, while the oxidation states of the Cu and Ru linkers (II and IV respectively) should match those in the system used by the Senkan group, these may have been altered by solvated ions in our MOF system. We did not run XPS analysis to confirm the oxidation states in our system, but that should be a major component for this project going forward to confirm the identity of each metal center within the MOF.

Another major factor in this epoxidation system is whether a cocatalyst is necessary for epoxide formation. In our other epoxidation project, the sacrificial



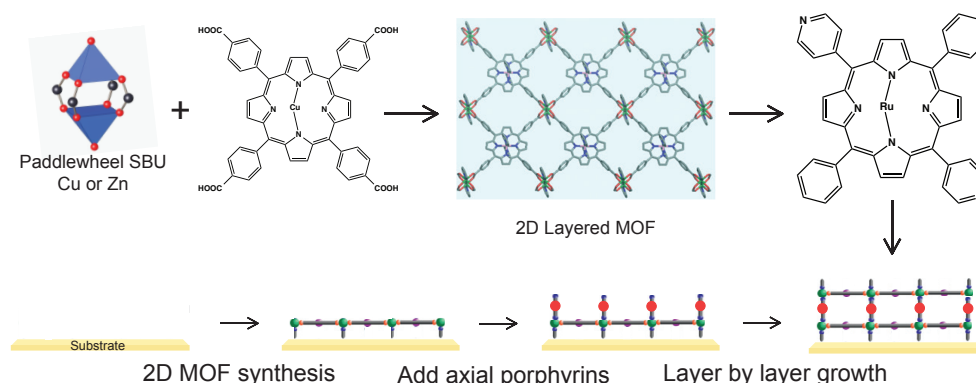


Figure 5.7: Schematic representation of 2D layered Cu-porphyrin MOF joined by axial Ru-porphyrins to make a bimetallic 3D MOF.

aldehyde isobutyraldehyde is an integral part of the catalytic system. For this system, and more specifically for propylene epoxidation, it remains to be seen if a cocatalyst is necessary to observe propylene oxide formation. The Senkan group observed that the introduction of NaCl into the space between nanoparticles facilitates higher reaction yield of propylene oxide but we are unsure whether the porous structure of a MOF needs the same NaCl introduction and whether a cocatalyst will remain inside the pores during catalysis. We attempted to saturate the pores with NaCl by soaking our bimetallic MOF with an aqueous NaCl solution but no propylene oxide was observed after attempted catalysis. While I believe the NaCl is necessary for higher propylene oxide formation, the distance between Cu and Ru centers seems to be of greater importance for this reaction and should be investigated first before varying cocatalysts.

Finally, it may be prudent to validate this bimetallic system in a gas phase epoxidation using a different alkene before attempting propylene epoxidation. At this point, we are unable to assess whether this bimetallic MOF system is even catalytically active due to the lack of observed epoxide products from our pro-

propylene reaction but proving that our system can form epoxides of longer chain alkenes, such as 1-hexene, 1-pentene or butene, at elevated temperatures would allow for both proof of concept and optimization of reaction parameters. This validation and optimization of our system is vital before pursuing the epoxidation of the more thermodynamically stable propylene.

One of the major problems working with bimetallic systems in MOF-525 is the idea of mixing different linkers that have similar symmetry and connectivity. The ability to use different linkers in the same framework is one of the major advantages of MOFs but specific placement of distinct linkers, relative to each other, requires more thought. A simple way of positioning each catalytic site in a well defined orientation is to first build a 2D framework using one type of linker, then the connect separate layers using a second linker with different connectivity. Similar systems have been seen before in several MOF systems [166] but have yet to be applied to bimetallic porphyrin systems. Our general overview can be seen in Figure 5.7, where we synthesize a 2D layer of Cu-porphyrins and then add Ru-porphyrins to the axial sites on the copper paddlewheel SBU to form a 3D MOF. The different connectivity of the two porphyrins allows for control of the distance and orientation between the two catalytic centers and should give greater pore control within the framework.

## **5.4 Effect of MOF Topology on Oligomerization of Propylene**

While density of catalytic sites can play a role in catalytic yield, it can also influence selectivity of products from catalytic reactions. One recent example of this selectivity was seen in the degree of dimer branching after the oligomerization of propylene over a nickel MOF catalyst. [58] While this system used the same topology in each case, the pore size was varied and this led to different degrees of

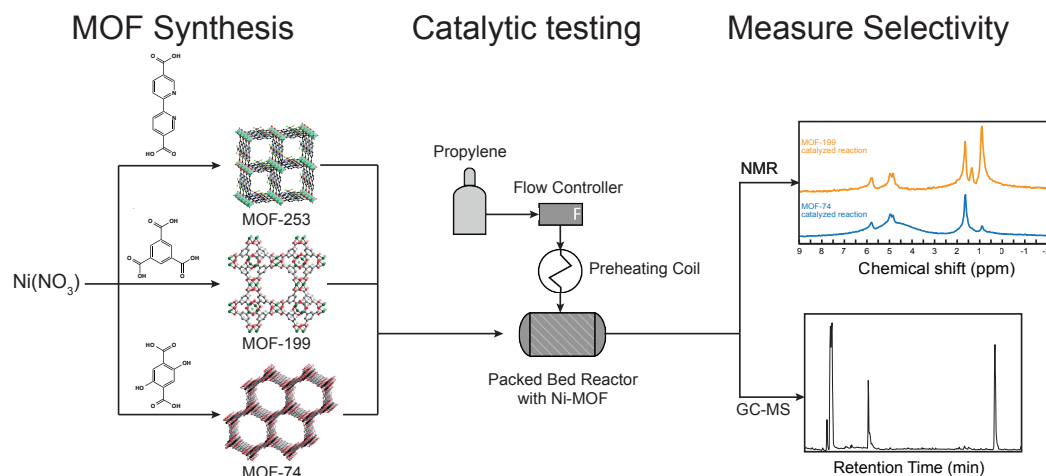


Figure 5.8: Synthesis and catalytic testing for oligomerization of propylene by nickel analogues of MOF-253, MOF-199 and MOF-74.

branching in each case. An alternative method is to totally change the topology of the MOF catalyst from one dimensional pores to three dimensional pores of various apertures and environments and to study the selectivity of product formation resulting from each topology. [167]

A general outline of our experimental set-up can be seen in Figure 5.8 where we synthesize three MOFs of different topology, test their catalytic activity and determine their selectivity using NMR and GC-MS. Nickel analogues of MOF-253, [168] MOF-199 [169] and MOF-74 [58] were selected because they are well known MOFs and can be reliably reproduced in high yield and quantity. In addition, each of these three MOFs has known analogues where pore diameter can be varied by changing the length of the organic link while still maintaining the same topology and catalytically active site of the overall MOF structure.

With these three structures we also can examine the differences between catalysts that are part of the metal SBU of the MOF and catalysts that have been added to the framework through PSM. [36] MOF-253 has a square planar nickel

site [168] on the organic link while the active sites in MOFs 199 [170] and 74 [171] are part of the backbone of the MOF. This illustrates yet another instance where catalytic site density can be varied amongst different MOFs, especially those using PSM to add a catalytically active site to a framework.

The idea of bimetallic MOFs for propylene epoxidation and varying topology for oligomerization are just a two examples of future projects but the field as a whole has many avenues for future research. Some important topics still unsolved are the development of industrially viable MOF catalysts, [172] biomimetic catalysts [134] and the mixing of frameworks and catalysts for cascade and tandem reactions . [173, 174] While MOFs hold several advantages over commonly used industrial supports, zeolites and silicas, there has yet to be an industrially viable MOF mainly due to their lack of chemical and thermal stability. The development of zirconium frameworks [51] has led to new testing in harsher chemical environments and development of new catalysts with Zr backbones, with industrial viability the key focus, should be given high priority in the MOF catalyst community.

In addition to industrially viable MOFs, the development of biomimetic frameworks should also be of great interest for future study. While MOF catalysis is still relatively new, the development of highly selective catalysts is of key importance for future MOF chemists. With the ability to position catalysts in precise locations inside frameworks, inspiration should be taken for enzymes to mimic active sites that are highly selective and show molecular preference during reactions. MOFs have already demonstrated selective gas uptake [64] and there is no reason to believe that similar molecular selectivity cannot be shown for heterogeneous catalysis. With the ability to alter the chemical environment, sterics, and size of the MOF pore; the ability to synthesize complex structures with lock and key or induced fit specificity [175] is an exciting idea for future MOF catalysts.

## 5.5 Cascade Catalysis in MOF Systems

Finally, one major topic that should be developed is the idea of tandem or cascade catalysis [176] utilizing MOFs. This has already been seen in homogeneous catalysis [177] but the development of solid-state catalysts should be of great importance due to their inherent advantages such as lack of necessary filtration and easy recyclability. [178]

The biggest challenge when discussing heterogeneous cascade catalysis is whether to have multiple catalysts in one framework or to sequester each catalyst into its own framework and then physically mix the frameworks. The development of heterogeneity in MOFs is a recent advancement [179] and there are still questions to be answered about the simplest way to obtain heterogeneity while maintaining crystalline order. In my experience, the easiest way to incorporate multiple catalysts is to keep them sequestered in their own framework. This makes the development of each catalyst simpler by having to crystallize out a structure with only one catalyst and keeps each framework relatively uncomplicated. While a single MOF containing multiple catalysts is a very interesting idea, the crystallization step becomes increasingly difficult as the pore environment becomes more complex. In addition, attempting to synthesize a MOF with catalytically active species is difficult due to the suppression of catalytic active site during solvothermal synthesis of the framework. This is one reason why PSM of frameworks has been such an important development for MOF catalysis. I have found it easier to add a catalytically active site after the MOF has already been synthesized. While PSM adds an additional step in the overall MOF synthesis, it allows MOF chemists to ensure that framework integrity is maintained throughout all necessary synthetic steps. One difficulty with PSM is the reaction yield of the PSM step, as it is often not quantitative as was demonstrated in Chapter 4 with our MTV MOF series. As pore space increases the yield of PSM also increases but

this would be something to study in further depth if PSM were to be used on an industrial scale. While it is often not necessary to have all available functionalities modified during the PSM step, inhomogeneity within a MOF structure could cause difficulties when discussing pore and, by extension, catalyst environment. While PSM is a very useful tool for inserting new functionalities and catalysts into a MOF, more work needs to be done to determine the relationship between pore environment and the efficiency of PSM reactions.

While the field of catalytically active MOFs is growing with each passing year, there is still much work to be done, specifically in testing the influence of MOF topology on catalytic yield and selectivity of different reactions. The exploration of topological effects on the yield in alkene epoxidation and the selectivity of dimer branching in propylene oligomerization could open up new avenues and tools for catalytic optimization in MOFs. In addition, the development of specific placement of multiple catalysts, in our case Cu and Ru porphyrins, within a single framework should be of highest priority as it would aid the development of an industrially viable MOF for propylene epoxidation. Selection of MOF topology to optimize specific catalytic reactions could soon be the next tool to join the MTV principle and PSM as commonly used techniques in applying the flexibility of reticular frameworks to industrially relevant projects.

## REFERENCES

- [1] Omar M Yaghi, Michael O’Keeffe, Nathan W Ockwig, Hee K Chae, Mohamed Eddaoudi, and Jaheon Kim. Reticular synthesis and the design of new materials. *Nature*, 423(6941):705–714, 2003.
- [2] Susumu Kitagawa, Ryo Kitaura, and Shin-ichiro Noro. Functional porous coordination polymers. *Angewandte Chemie International Edition*, 43(18):2334–2375, 2004.
- [3] Gérard Férey. Hybrid porous solids: past, present, future. *Chemical Society Reviews*, 37(1):191–214, 2008.
- [4] Alexander U Czaja, Natalia Trukhan, and Ulrich Müller. Industrial applications of metal–organic frameworks. *Chemical Society Reviews*, 38(5):1284–1293, 2009.
- [5] Zheng Lu, Carolyn B Knobler, Hiroyasu Furukawa, Bo Wang, Guannan Liu, and Omar M Yaghi. Synthesis and structure of chemically stable metal-organic polyhedra. *Journal of the American Chemical Society*, 131(35):12532–12533, 2009.
- [6] Kyo Sung Park, Zheng Ni, Adrien P Côté, Jae Yong Choi, Rudan Huang, Fernando J Uribe-Romo, Hee K Chae, Michael O’Keeffe, and Omar M Yaghi. Exceptional chemical and thermal stability of zeolitic imidazolate frameworks. *Proceedings of the National Academy of Sciences*, 103(27):10186–10191, 2006.
- [7] Thierry Loiseau, Christian Serre, Clarisse Huguenard, Gerhard Fink, Francis Taulelle, Marc Henry, Thierry Bataille, and Gérard Férey. A rationale for the large breathing of the porous aluminum terephthalate (mil-53) upon hydration. *Chemistry-A European Journal*, 10(6):1373–1382, 2004.
- [8] Hee K Chae, Diana Y Siberio-Pérez, Jaheon Kim, YongBok Go, Mohamed Eddaoudi, Adam J Matzger, Michael O’Keeffe, and Omar M Yaghi. A route to high surface area, porosity and inclusion of large molecules in crystals. *Nature*, 427(6974):523–527, 2004.
- [9] Hiroyasu Furukawa, Nakeun Ko, Yong Bok Go, Naoki Aratani, Sang Beom Choi, Eunwoo Choi, A Özgür Yazaydin, Randall Q Snurr, Michael O’Keeffe, Jaheon Kim, et al. Ultrahigh porosity in metal-organic frameworks. *Science*, 329(5990):424–428, 2010.
- [10] Abraham M Shultz, Omar K Farha, Joseph T Hupp, and SonBinh T Nguyen. A catalytically active, permanently microporous mof with metalloporphyrin struts. *Journal of the American Chemical Society*, 131(12):4204–4205, 2009.

- [11] Satoshi Horike, Mircea Dinca, Kentaro Tamaki, and Jeffrey R Long. Size-selective lewis acid catalysis in a microporous metal-organic framework with exposed  $\text{Mn}^{2+}$  coordination sites. *Journal of the American Chemical Society*, 130(18):5854–5855, 2008.
- [12] Rahul Banerjee, Anh Phan, Bo Wang, Carolyn Knobler, Hiroyasu Furukawa, Michael O’Keeffe, and Omar M Yaghi. High-throughput synthesis of zeolitic imidazolate frameworks and application to  $\text{CO}_2$  capture. *Science*, 319(5865):939–943, 2008.
- [13] Bo Wang, Adrien P Côté, Hiroyasu Furukawa, Michael O’Keeffe, and Omar M Yaghi. Colossal cages in zeolitic imidazolate frameworks as selective carbon dioxide reservoirs. *Nature*, 453(7192):207–211, 2008.
- [14] Lifang Song, Jian Zhang, Lixian Sun, Fen Xu, Fen Li, Huanzhi Zhang, Xiaoliang Si, Chengli Jiao, Zhibao Li, Shuang Liu, et al. Mesoporous metal-organic frameworks: design and applications. *Energy & Environmental Science*, 5(6):7508–7520, 2012.
- [15] Sabine Achmann, Gunter Hagen, Jaroslaw Kita, Itamar M Malkowsky, Christoph Kiener, and Ralf Moos. Metal-organic frameworks for sensing applications in the gas phase. *Sensors*, 9(3):1574–1589, 2009.
- [16] Yoji Kobayashi, Benjamin Jacobs, Mark D Allendorf, and Jeffrey R Long. Conductivity, doping, and redox chemistry of a microporous dithiolene-based metal-organic framework. *Chemistry of Materials*, 22(14):4120–4122, 2010.
- [17] Shinya Takaishi, Miyuki Hosoda, Takashi Kajiwarra, Hitoshi Miyasaka, Masahiro Yamashita, Yasuyuki Nakanishi, Yasutaka Kitagawa, Kizashi Yamaguchi, Atsushi Kobayashi, and Hiroshi Kitagawa. Electroconductive porous coordination polymer  $\text{Cu}[\text{Cu}(\text{pdt})_2]$  composed of donor and acceptor building units. *Inorganic chemistry*, 48(19):9048–9050, 2008.
- [18] Steven S Kaye and Jeffrey R Long. Hydrogen storage in the dehydrated prussian blue analogues  $\text{M}_3[\text{Co}(\text{CN})_6]_2$  ( $\text{M} = \text{Mn}, \text{Fe}, \text{Co}, \text{Ni}, \text{Cu}, \text{Zn}$ ). *Journal of the American Chemical Society*, 127(18):6506–6507, 2005.
- [19] Steven S Kaye, Hye Jin Choi, and Jeffrey R Long. Generation and  $\text{O}_2$  adsorption studies of the microporous magnets  $\text{CsNi}[\text{Cr}(\text{CN})_6](\text{TC} = 75 \text{ K})$  and  $\text{Cr}_3[\text{Cr}(\text{CN})_6]_2 \cdot 6\text{H}_2\text{O}$  ( $\text{TN} = 219 \text{ K}$ ). *Journal of the American Chemical Society*, 130(50):16921–16925, 2008.
- [20] Bogdan V Harbuzaru, Avelino Corma, Fernando Rey, Pedro Atienzar, Jose L Jordá, Hermenegildo García, Duarte Ananias, Luis D Carlos, and



- João Rocha. Metal–organic nanoporous structures with anisotropic photoluminescence and magnetic properties and their use as sensors. *Angewandte Chemie International Edition*, 47(6):1080–1083, 2008.
- [21] CNR Rao, AK Cheetham, and A Thirumurugan. Hybrid inorganic–organic materials: a new family in condensed matter physics. *Journal of Physics: Condensed Matter*, 20(8):083202, 2008.
  - [22] Shuangbing Han, Yanhu Wei, Cory Valente, István Lagzi, Jeremiah J Gassensmith, Ali Coskun, J Fraser Stoddart, and Bartosz A Grzybowski. Chromatography in a single metal- organic framework (mof) crystal. *Journal of the American Chemical Society*, 132(46):16358–16361, 2010.
  - [23] Chuan-De Wu, Aiguo Hu, Lin Zhang, and Wenbin Lin. A homochiral porous metal-organic framework for highly enantioselective heterogeneous asymmetric catalysis. *Journal of the American Chemical Society*, 127(25):8940–8941, 2005.
  - [24] Liqing Ma, Carter Abney, and Wenbin Lin. Enantioselective catalysis with homochiral metal–organic frameworks. *Chemical Society Reviews*, 38(5):1248–1256, 2009.
  - [25] Kathryn ML Taylor-Pashow, Joseph Della Rocca, Zhigang Xie, Sylvie Tran, and Wenbin Lin. Postsynthetic modifications of iron-carboxylate nanoscale metal- organic frameworks for imaging and drug delivery. *Journal of the American Chemical Society*, 131(40):14261–14263, 2009.
  - [26] Patricia Horcajada, Christian Serre, María Vallet-Regí, Muriel Sebban, Francis Taulelle, and Gérard Férey. Metal–organic frameworks as efficient materials for drug delivery. *Angewandte Chemie*, 118(36):6120–6124, 2006.
  - [27] Hailian Li, Mohamed Eddaoudi, Michael O’Keeffe, and Omar M Yaghi. Design and synthesis of an exceptionally stable and highly porous metal-organic framework. *Nature*, 402(6759):276–279, 1999.
  - [28] Mohamed Eddaoudi, Jaheon Kim, Nathaniel Rosi, David Vodak, Joseph Wachter, Michael O’Keeffe, and Omar M Yaghi. Systematic design of pore size and functionality in isoreticular mofs and their application in methane storage. *Science*, 295(5554):469–472, 2002.
  - [29] David J Tranchemontagne, José L Mendoza-Cortés, Michael O’Keeffe, and Omar M Yaghi. Secondary building units, nets and bonding in the chemistry of metal–organic frameworks. *Chemical Society Reviews*, 38(5):1257–1283, 2009.
  - [30] Hexiang Deng, Christian J Doonan, Hiroyasu Furukawa, Ricardo B Ferreira, John Towne, Carolyn B Knobler, Bo Wang, and Omar M Yaghi. Multiple

- functional groups of varying ratios in metal-organic frameworks. *Science*, 327(5967):846–850, 2010.
- [31] Xueqian Kong, Hexiang Deng, Fangyong Yan, Jihan Kim, Joseph A Swisher, Berend Smit, Omar M Yaghi, and Jeffrey A Reimer. Mapping of functional groups in metal-organic frameworks. *Science*, 341(6148):882–885, 2013.
  - [32] Shuangquan Zang, Yang Su, Chunying Duan, Yizhi Li, Huizhen Zhu, and Qingjin Meng. Coexistence of chiral hydrophilic and achiral hydrophobic channels in one multi-helical-array metal-organic framework incorporating helical water cluster chains. *Chemical communications*, (48):4997–4999, 2006.
  - [33] Luc Alaerts, Etienne Séguin, Hilde Poelman, Frédéric Thibault-Starzyk, Pierre A Jacobs, and Dirk E De Vos. Probing the lewis acidity and catalytic activity of the metal-organic framework [cu<sub>3</sub> (btc)<sub>2</sub>](btc= benzene-1, 3, 5-tricarboxylate). *Chemistry-a European Journal*, 12(28):7353–7363, 2006.
  - [34] Frederik Vermoortele, Rob Ameloot, Alexandre Vimont, Christian Serre, and Dirk De Vos. An amino-modified zr-terephthalate metal-organic framework as an acid-base catalyst for cross-aldol condensation. *Chemical Communications*, 47(5):1521–1523, 2011.
  - [35] Xingling Xu, Mark Nieuwenhuyzen, and Stuart L James. A nanoporous metal-organic framework based on bulky phosphane ligands. *Angewandte Chemie International Edition*, 41(5):764–767, 2002.
  - [36] Zhenqiang Wang and Seth M Cohen. Postsynthetic modification of metal-organic frameworks. *Chemical Society Reviews*, 38(5):1315–1329, 2009.
  - [37] Kristine K Tanabe, Zhenqiang Wang, and Seth M Cohen. Systematic functionalization of a metal-organic framework via a postsynthetic modification approach. *Journal of the American Chemical Society*, 130(26):8508–8517, 2008.
  - [38] Kristine K Tanabe and Seth M Cohen. Engineering a metal-organic framework catalyst by using postsynthetic modification. *Angewandte Chemie*, 121(40):7560–7563, 2009.
  - [39] Zhenqiang Wang and Seth M Cohen. Tandem modification of metal-organic frameworks by a postsynthetic approach. *Angewandte Chemie*, 120(25):4777–4780, 2008.
  - [40] William Morris, Christian J Doonan, Hiroyasu Furukawa, Rahul Banerjee, and Omar M Yaghi. Crystals as molecules: postsynthesis covalent functionalization of zeolitic imidazolate frameworks. *Journal of the American Chemical Society*, 130(38):12626–12627, 2008.

- [41] Kristine K Tanabe and Seth M Cohen. Postsynthetic modification of metal-organic frameworks a progress report. *Chemical Society Reviews*, 40(2):498–519, 2011.
- [42] Yuanbiao Huang, Shuiying Gao, Tianfu Liu, Jian Lü, Xi Lin, Hongfang Li, and Rong Cao. Palladium nanoparticles supported on mixed-linker metal-organic frameworks as highly active catalysts for heck reactions. *ChemPlusChem*, 77(2):106–112, 2012.
- [43] Andrew R Burgoyne and Reinout Meijboom. Knoevenagel condensation reactions catalysed by metal-organic frameworks. *Catalysis letters*, 143(6):563–571, 2013.
- [44] Kenneth S Suslick, P Bhyrappa, J-H Chou, Margaret E Kosal, Shirley Nakagaki, Dennis W Smithenry, and Scott R Wilson. Microporous porphyrin solids. *Accounts of chemical research*, 38(4):283–291, 2005.
- [45] Feijie Song, Cheng Wang, Joseph M Falkowski, Liqing Ma, and Wenbin Lin. Isorecticular chiral metal- organic frameworks for asymmetric alkene epoxidation: Tuning catalytic activity by controlling framework catenation and varying open channel sizes. *Journal of the American Chemical Society*, 132(43):15390–15398, 2010.
- [46] JeongYong Lee, Omar K Farha, John Roberts, Karl A Scheidt, SonBinh T Nguyen, and Joseph T Hupp. Metal-organic framework materials as catalysts. *Chemical Society Reviews*, 38(5):1450–1459, 2009.
- [47] Marco Ranocchiari and Jeroen Anton van Bokhoven. Catalysis by metal-organic frameworks: fundamentals and opportunities. *Physical Chemistry Chemical Physics*, 13(14):6388–6396, 2011.
- [48] Mohamed Eddaoudi, David B Moler, Hailian Li, Banglin Chen, Theresa M Reineke, Michael O’keeffe, and Omar M Yaghi. Modular chemistry: secondary building units as a basis for the design of highly porous and robust metal-organic carboxylate frameworks. *Accounts of Chemical Research*, 34(4):319–330, 2001.
- [49] Mathivathani Kandiah, Merete Hellner Nilsen, Sandro Usseglio, Søren Jakobsen, Unni Olsbye, Mats Tilset, Cherif Larabi, Elsje Alessandra Quadrelli, Francesca Bonino, and Karl Petter Lillerud. Synthesis and stability of tagged uio-66 zr-mofs. *Chemistry of Materials*, 22(24):6632–6640, 2010.
- [50] Aude Demessence, Deanna M DAlessandro, Maw Lin Foo, and Jeffrey R Long. Strong co2 binding in a water-stable, triazolate-bridged metal- organic framework functionalized with ethylenediamine. *Journal of the American Chemical Society*, 131(25):8784–8786, 2009.

- [51] Jasmina Hafizovic Cavka, Søren Jakobsen, Unni Olsbye, Nathalie Guillou, Carlo Lamberti, Silvia Bordiga, and Karl Petter Lillerud. A new zirconium inorganic building brick forming metal organic frameworks with exceptional stability. *Journal of the American Chemical Society*, 130(42):13850–13851, 2008.
- [52] Gerard Férey, Caroline Mellot-Draznieks, Christian Serre, Franck Millange, Julien Dutour, Suzy Surblé, and Irena Margiolaki. A chromium terephthalate-based solid with unusually large pore volumes and surface area. *Science*, 309(5743):2040–2042, 2005.
- [53] Lomig Hamon, Christian Serre, Thomas Devic, Thierry Loiseau, Franck Millange, Gérard Férey, and Guy De Weireld. Comparative study of hydrogen sulfide adsorption in the mil-53 (al, cr, fe), mil-47 (v), mil-100 (cr), and mil-101 (cr) metal-organic frameworks at room temperature. *Journal of the American Chemical Society*, 131(25):8775–8777, 2009.
- [54] So-Hye Cho, Baoqing Ma, SonBinh T Nguyen, Joseph T Hupp, and Thomas E Albrecht-Schmitt. A metal-organic framework material that functions as an enantioselective catalyst for olefin epoxidation. *Chemical communications*, (24):2563–2565, 2006.
- [55] John R Monnier. The direct epoxidation of higher olefins using molecular oxygen. *Applied Catalysis A: General*, 221(1):73–91, 2001.
- [56] T Alexander Nijhuis, Michiel Makkee, Jacob A Moulijn, and Bert M Weckhuysen. The production of propene oxide: Catalytic processes and recent developments. *Industrial & engineering chemistry research*, 45(10):3447–3459, 2006.
- [57] Siegfried Rebsdat and Dieter Mayer. Ethylene oxide. *Ullmann’s Encyclopedia of Industrial Chemistry*, 2001.
- [58] Anton N Mlinar, Benjamin K Keitz, David Gygi, Eric D Bloch, Jeffrey R Long, and Alexis T Bell. Selective propene oligomerization with nickel (ii)-based metal-organic frameworks. *ACS Catalysis*, 4(3):717–721, 2014.
- [59] Stuart L James. Metal-organic frameworks. *Chemical Society Reviews*, 32(5):276–288, 2003.
- [60] Jesse LC Rowsell and Omar M Yaghi. Metal-organic frameworks: a new class of porous materials. *Microporous and Mesoporous Materials*, 73(1):3–14, 2004.
- [61] Hexiang Deng, Sergio Grunder, Kyle E Cordova, Cory Valente, Hiroyasu Furukawa, Mohamad Hmadeh, Felipe Gándara, Adam C Whalley, Zheng Liu, Shunsuke Asahina, et al. Large-pore apertures in a series of metal-organic frameworks. *science*, 336(6084):1018–1023, 2012.

- [62] Banglin Chen, Liangbo Wang, Yunqing Xiao, Frank R Fronczek, Ming Xue, Yuanjing Cui, and Guodong Qian. A luminescent metal–organic framework with lewis basic pyridyl sites for the sensing of metal ions. *Angewandte Chemie International Edition*, 48(3):500–503, 2009.
- [63] Anjian Lan, Kunhao Li, Haohan Wu, David H Olson, Thomas J Emge, Woosok Ki, Maochun Hong, and Jing Li. A luminescent microporous metal–organic framework for the fast and reversible detection of high explosives. *Angewandte Chemie International Edition*, 48(13):2334–2338, 2009.
- [64] Jian-Rong Li, Ryan J Kuppler, and Hong-Cai Zhou. Selective gas adsorption and separation in metal–organic frameworks. *Chemical Society Reviews*, 38(5):1477–1504, 2009.
- [65] Nathaniel L Rosi, Juergen Eckert, Mohamed Eddaoudi, David T Vodak, Jaheon Kim, Michael O’Keeffe, and Omar M Yaghi. Hydrogen storage in microporous metal-organic frameworks. *Science*, 300(5622):1127–1129, 2003.
- [66] Jesse LC Rowsell and Omar M Yaghi. Strategies for hydrogen storage in metal–organic frameworks. *Angewandte Chemie International Edition*, 44(30):4670–4679, 2005.
- [67] David Farrusseng, Sonia Aguado, and Catherine Pinel. Metal–organic frameworks: opportunities for catalysis. *Angewandte Chemie International Edition*, 48(41):7502–7513, 2009.
- [68] Rachel C Huxford, Joseph Della Rocca, and Wenbin Lin. Metal–organic frameworks as potential drug carriers. *Current opinion in chemical biology*, 14(2):262–268, 2010.
- [69] HM Dhammika Bandara and Shawn C Burdette. Photoisomerization in different classes of azobenzene. *Chemical Society Reviews*, 41(5):1809–1825, 2012.
- [70] K Hoffmann, U Resch-Genger, and F Marlow. Photoinduced switching of nanocomposites consisting of azobenzene and molecular sieves: investigation of the switching states. *Microporous and mesoporous materials*, 41(1):99–106, 2000.
- [71] Christina M Stuart, Renee R Frontiera, and Richard A Mathies. Excited-state structure and dynamics of cis-and trans-azobenzene from resonance raman intensity analysis. *The Journal of Physical Chemistry A*, 111(48):12072–12080, 2007.
- [72] Nanguo Liu, Zhu Chen, Darren R Dunphy, Ying-Bing Jiang, Roger A Assink, and C Jeffrey Brinker. Photoresponsive nanocomposite formed by

- self-assembly of an azobenzene-modified silane. *Angewandte Chemie International Edition*, 42(15):1731–1734, 2003.
- [73] Wolfgang Freyer, Daniel Brete, Roland Schmidt, Cornelius Gahl, Robert Carley, and Martin Weinelt. Switching behavior and optical absorbance of azobenzene-functionalized alkanethiols in different environments. *Journal of Photochemistry and Photobiology A: Chemistry*, 204(2):102–109, 2009.
  - [74] Jingbin Han, Dongpeng Yan, Wenying Shi, Jing Ma, Hong Yan, Min Wei, David G Evans, and Xue Duan. Layer-by-layer ultrathin films of azobenzene-containing polymer/layered double hydroxides with reversible photoresponsive behavior. *The Journal of Physical Chemistry B*, 114(17):5678–5685, 2010.
  - [75] Sarah Angelos, Eunshil Choi, Fritz Vögtle, Luisa De Cola, and Jeffrey I Zink. Photo-driven expulsion of molecules from mesostructured silica nanoparticles. *The Journal of Physical Chemistry C*, 111(18):6589–6592, 2007.
  - [76] C Barrett, A Natansohn, and P Rochon. Thermal cis-trans isomerization rates of azobenzenes bound in the side chain of some copolymers and blends. *Macromolecules*, 27(17):4781–4786, 1994.
  - [77] Eric Besson, Ahmad Mehdi, Dan A Lerner, Catherine Rey  , and Robert JP Corriu. Photoresponsive ordered hybrid materials containing a bridged azobenzene group. *Journal of Materials Chemistry*, 15(7):803–809, 2005.
  - [78] Y Einaga, O Sato, T Iyoda, A Fujishima, and K Hashimoto. Photofunctional vesicles containing prussian blue and azobenzene. *Journal of the American Chemical Society*, 121(15):3745–3750, 1999.
  - [79] Erik Johansson, Eunshil Choi, Sarah Angelos, Monty Liong, and Jeffrey I Zink. Light-activated functional mesostructured silica. *Journal of Sol-Gel Science and Technology*, 46(3):313–322, 2008.
  - [80] DY Kim, SK Tripathy, Lian Li, and J Kumar. Laser-induced holographic surface relief gratings on nonlinear optical polymer films. *Applied Physics Letters*, 66(10):1166–1168, 1995.
  - [81] G Sudesh Kumar and DC Neckers. Photochemistry of azobenzene-containing polymers. *Chemical Reviews*, 89(8):1915–1925, 1989.
  - [82] Takuya Naito, Kazuyuki Horie, and Itaru Mita. Photochemistry in polymer solids: 12. effects of main-chain structures and formation of hydrogen bonds on photoisomerization of azobenzene in various polymer films. *Polymer*, 34(19):4140–4145, 1993.

- [83] Makoto Ogawa, Kazuyuki Kuroda, and Jun-ichi Mori. Aluminium-containing mesoporous silica films as nano-vessels for organic photochemical reactions. *Chemical Communications*, (24):2441–2442, 2000.
- [84] Paul Sierocki, Huub Maas, Patrick Dragut, Gabriele Richardt, Fritz Vögtle, Luisa De Cola, Fred Brouwer, and Jeffrey I Zink. Photoisomerization of azobenzene derivatives in nanostructured silica. *The Journal of Physical Chemistry B*, 110(48):24390–24398, 2006.
- [85] Shiki Yagai, Takashi Karatsu, and Akihide Kitamura. Photocontrollable self-assembly. *Chemistry-a European Journal*, 11(14):4054–4063, 2005.
- [86] Yingkui Yang, Xiaotao Wang, Lang Liu, Xiaolin Xie, Zhifang Yang, Robert Kwok Yiu Li, and Yiu-Wing Mai. Structure and photoresponsive behaviors of multiwalled carbon nanotubes grafted by polyurethanes containing azobenzene side chains. *The Journal of Physical Chemistry C*, 111(30):11231–11239, 2007.
- [87] Sarah Angelos, Ying-Wei Yang, Niveen M Khashab, J Fraser Stoddart, and Jeffrey I Zink. Dual-controlled nanoparticles exhibiting and logic. *Journal of the American Chemical Society*, 131(32):11344–11346, 2009.
- [88] Sarah Angelos, Erik Johansson, J Fraser Stoddart, and Jeffrey I Zink. Mesostructured silica supports for functional materials and molecular machines. *Advanced Functional Materials*, 17(14):2261–2271, 2007.
- [89] Hiroshi Sato, Ryotaro Matsuda, Kuniyoshi Sugimoto, Masaki Takata, and Susumu Kitagawa. Photoactivation of a nanoporous crystal for on-demand guest trapping and conversion. *Nature materials*, 9(8):661–666, 2010.
- [90] Alexander J Blake, Neil R Champness, Timothy L Easun, David R Allan, Harriott Nowell, Michael W George, Junhua Jia, and Xue-Zhong Sun. Photoreactivity examined through incorporation in metal-organic frameworks. *Nature chemistry*, 2(8):688–694, 2010.
- [91] Kristine K Tanabe, Corinne A Allen, and Seth M Cohen. Photochemical activation of a metal–organic framework to reveal functionality. *Angewandte Chemie*, 122(50):9924–9927, 2010.
- [92] Corinne A Allen and Seth M Cohen. Near-uv photo-induced modification in isorecticular metal–organic frameworks. *Journal of Materials Chemistry*, 22(20):10188–10194, 2012.
- [93] Rajesh K Deshpande, Geoffrey IN Waterhouse, Geoffrey B Jameson, and Shane G Telfer. Photolabile protecting groups in metal–organic frameworks: preventing interpenetration and masking functional groups. *Chemical Communications*, 48(10):1574–1576, 2012.

- [94] Antje Modrow, Dordaneh Zargarani, Rainer Herges, and Norbert Stock. The first porous mof with photoswitchable linker molecules. *Dalton Transactions*, 40(16):4217–4222, 2011.
- [95] Jinhee Park, Daqiang Yuan, Khanh T Pham, Jian-Rong Li, Andrey Yakovenko, and Hong-Cai Zhou. Reversible alteration of co<sub>2</sub> adsorption upon photochemical or thermal treatment in a metal–organic framework. *Journal of the American Chemical Society*, 134(1):99–102, 2011.
- [96] Sarah Angelos, Monty Liong, Eunshil Choi, and Jeffrey I Zink. Mesoporous silicate materials as substrates for molecular machines and drug delivery. *Chemical Engineering Journal*, 137(1):4–13, 2008.
- [97] Yuen A Lau, Bryana L Henderson, Jie Lu, Daniel P Ferris, Fuyuhiko Tamanoi, and Jeffrey I Zink. Continuous spectroscopic measurements of photo-stimulated release of molecules by nanomachines in a single living cell. *Nanoscale*, 4(11):3482–3489, 2012.
- [98] L Sieminska, M Ferguson, TW Zerda, and E Couch. Diffusion of steroids in porous sol-gel glass: application in slow drug delivery. *Journal of Sol-Gel Science and Technology*, 8(1-3):1105–1109, 1997.
- [99] Luigia Rossi, Giorgio Brandi, Giuditta F Schiavano, Sonia Scarfi, Enrico Millo, Gianluca Damonte, Umberto Benatti, Antonio De Flora, and Mauro Magnani. Heterodimer-loaded erythrocytes as bioreactors for slow delivery of the antiviral drug azidothymidine and the antimycobacterial drug ethambutol. *AIDS research and human retroviruses*, 15(4):345–353, 1999.
- [100] Libo Yang and Reza Fassihi. Modulation of diclofenac release from a totally soluble controlled release drug delivery system. *Journal of controlled release*, 44(2):135–140, 1997.
- [101] Hong-Cai Zhou, Jeffrey R Long, and Omar M Yaghi. Introduction to metal–organic frameworks. *Chemical reviews*, 112(2):673–674, 2012.
- [102] Kyoungmoo Koh, Antek G Wong-Foy, and Adam J Matzger. Mof@ mof: microporous core–shell architectures. *Chemical Communications*, (41):6162–6164, 2009.
- [103] Hyungphil Chun, Danil N Dybtsev, Hyunuk Kim, and Kimoon Kim. Synthesis, x-ray crystal structures, and gas sorption properties of pillared square grid nets based on paddle-wheel motifs: Implications for hydrogen storage in porous materials. *Chemistry-A European Journal*, 11(12):3521–3529, 2005.
- [104] Stefan Marx, Wolfgang Kleist, Jun Huang, Marek Maciejewski, and Alfons Baiker. Tuning functional sites and thermal stability of mixed-linker mofs based on mil-53 (al). *Dalton Transactions*, 39(16):3795–3798, 2010.



- [105] Christian J Doonan, William Morris, Hiroyasu Furukawa, and Omar M Yaghi. Isoreticular metalation of metal- organic frameworks. *Journal of the American Chemical Society*, 131(27):9492–9493, 2009.
- [106] Michael J Ingleson, Jorge Perez Barrio, John Bacsá, Calum Dickinson, Hyunsoo Park, and Matthew J Rosseinsky. Generation of a solid brønsted acid site in a chiral framework. *Chemical Communications*, (11):1287–1289, 2008.
- [107] Andrew D Burrows, Christopher G Frost, Mary F Mahon, and Christopher Richardson. Post-synthetic modification of tagged metal–organic frameworks. *Angewandte Chemie International Edition*, 47(44):8482–8486, 2008.
- [108] Jorge Gascon, Ugur Aktay, Maria D Hernandez-Alonso, Gerard PM van Klink, and Freek Kapteijn. Amino-based metal-organic frameworks as stable, highly active basic catalysts. *Journal of Catalysis*, 261(1):75–87, 2009.
- [109] Wolfgang Kleist, Fabian Jutz, Marek Maciejewski, and Alfons Baiker. Mixed-linker metal-organic frameworks as catalysts for the synthesis of propylene carbonate from propylene oxide and co<sub>2</sub>. *European Journal of Inorganic Chemistry*, 2009(24):3552–3561, 2009.
- [110] Nam TS Phan, Matthew Van Der Sluys, and Christopher W Jones. On the nature of the active species in palladium catalyzed mizoroki–heck and suzuki–miyaura couplings–homogeneous or heterogeneous catalysis, a critical review. *Advanced Synthesis & Catalysis*, 348(6):609–679, 2006.
- [111] Christian Torborg and Matthias Beller. Recent applications of palladium-catalyzed coupling reactions in the pharmaceutical, agrochemical, and fine chemical industries. *Advanced Synthesis & Catalysis*, 351(18):3027–3043, 2009.
- [112] Karine Ferré-Filmon, Lionel Delaude, Albert Demonceau, and Alfred F Noels. Catalytic methods for the synthesis of stilbenes with an emphasis on their phytoalexins. *Coordination chemistry reviews*, 248(21):2323–2336, 2004.
- [113] Young Kyu Hwang, Do-Young Hong, Jong-San Chang, Sung Hwa Jhung, You-Kyong Seo, Jinheung Kim, Alexandre Vimont, Marco Daturi, Christian Serre, and Gérard Férey. Amine grafting on coordinatively unsaturated metal centers of mofs: consequences for catalysis and metal encapsulation. *Angewandte Chemie International Edition*, 47(22):4144–4148, 2008.
- [114] JF Savouret and M Quesne. Resveratrol and cancer: a review. *Biomedicine & pharmacotherapy*, 56(2):84–87, 2002.

- [115] Avelino Corma, Hermenegildo Garcia, Antonio Leyva, and Ana Primo. Basic zeolites containing palladium as bifunctional heterogeneous catalysts for the heck reaction. *Applied Catalysis A: General*, 247(1):41–49, 2003.
- [116] K Kohler, SS Prockl, and W Kleist. Supported palladium catalysts in heck coupling reactions-problems, potential and recent advances. *Current Organic Chemistry*, 10(13):1585–1601, 2006.
- [117] Liang Li, Ling-Xia Zhang, Jian-Lin Shi, Ji-Na Yan, and Jian Liang. New and efficient heterogeneous catalytic system for heck reaction: palladium colloid layer in situ reduced in the channel of mesoporous silica materials. *Applied Catalysis A: General*, 283(1):85–89, 2005.
- [118] Luis Botella and Carmen Nájera. Synthesis of methylated resveratrol and analogues by heck reactions in organic and aqueous solvents. *Tetrahedron*, 60(26):5563–5570, 2004.
- [119] Silvia Bradamante, Livia Barengi, and Alessandro Villa. Cardiovascular protective effects of resveratrol. *Cardiovascular drug reviews*, 22(3):169–188, 2004.
- [120] Jonathan P Knowles and Andrew Whiting. The heck–mizoroki cross-coupling reaction: a mechanistic perspective. *Organic & biomolecular chemistry*, 5(1):31–44, 2007.
- [121] Kazu Okumura, Takuya Tomiyama, Sayaka Moriyama, Ayaka Nakamichi, and Miki Niwa. Enhancement in the catalytic activity of pd/usy in the heck reaction induced by h<sub>2</sub> bubbling. *Molecules*, 16(1):38–51, 2010.
- [122] Ken-ichi Shimizu, Soichi Koizumi, Tsuyoshi Hatamachi, Hisao Yoshida, Shinichi Komai, Tatsuya Kodama, and Yoshie Kitayama. Structural investigations of functionalized mesoporous silica-supported palladium catalyst for heck and suzuki coupling reactions. *Journal of Catalysis*, 228(1):141–151, 2004.
- [123] Robert H Crabtree. Resolving heterogeneity problems and impurity artifacts in operationally homogeneous transition metal catalysts. *Chemical reviews*, 112(3):1536–1554, 2011.
- [124] Aleksey Vishnyakov, Peter I Ravikovitch, Alexander V Neimark, Martin Bülow, and Qing Min Wang. Nanopore structure and sorption properties of cu-btc metal-organic framework. *Nano Letters*, 3(6):713–718, 2003.
- [125] Xiao-Ping Zhou, Zhengtao Xu, Matthias Zeller, and Allen D Hunter. Reversible uptake of hgcl<sub>2</sub> in a porous coordination polymer based on the dual functions of carboxylate and thioether. *Chemical Communications*, (36):5439–5441, 2009.

- [126] Sergio J Garibay, Zhenqiang Wang, and Seth M Cohen. Evaluation of heterogeneous metal-organic framework organocatalysts prepared by postsynthetic modification. *Inorganic chemistry*, 49(17):8086–8091, 2010.
- [127] William Morris, RE Taylor, C Dybowski, Omar M Yaghi, and Miguel A Garcia-Garibay. Framework mobility in the metal–organic framework crystal irmo-3: Evidence for aromatic ring and amine rotation. *Journal of Molecular Structure*, 1004(1):94–101, 2011.
- [128] William Morris, Christian J Doonan, and Omar M Yaghi. Postsynthetic modification of a metal–organic framework for stabilization of a hemiaminal and ammonia uptake. *Inorganic chemistry*, 50(15):6853–6855, 2011.
- [129] Yuxiang Rao, Tom F Kemp, Michel Trudeau, Mark E Smith, and Dave M Antonelli. <sup>17</sup>O and <sup>15</sup>N solid state nmr studies on ligand-assisted templating and oxygen coordination in the walls of mesoporous nb, ta and ti oxides. *Journal of the American Chemical Society*, 130(46):15726–15731, 2008.
- [130] Hiroyasu Furukawa, Kyle E Cordova, Michael O’Keeffe, and Omar M Yaghi. The chemistry and applications of metal-organic frameworks. *Science*, 341(6149):1230444, 2013.
- [131] A Corma, H Garcia, and FX Llabrés i Xamena. Engineering metal organic frameworks for heterogeneous catalysis. *Chemical Reviews*, 110(8):4606–4655, 2010.
- [132] Sabine Opelt, Stefan Türk, Enrico Dietzsch, Antje Henschel, Stefan Kaskel, and Elias Klemm. Preparation of palladium supported on mof-5 and its use as hydrogenation catalyst. *Catalysis Communications*, 9(6):1286–1290, 2008.
- [133] Hai-Long Jiang, Bo Liu, Tomoki Akita, Masatake Haruta, Hiroaki Sakurai, and Qiang Xu. Au@ zif-8: Co oxidation over gold nanoparticles deposited to metal-organic framework. *Journal of the American Chemical Society*, 131(32):11302–11303, 2009.
- [134] Dawei Feng, Zhi-Yuan Gu, Jian-Rong Li, Hai-Long Jiang, Zhangwen Wei, and Hong-Cai Zhou. Zirconium-metalloporphyrin pcn-222: Mesoporous metal–organic frameworks with ultrahigh stability as biomimetic catalysts. *Angewandte Chemie*, 124(41):10453–10456, 2012.
- [135] Ming-Hua Xie, Xiu-Li Yang, Chao Zou, and Chuan-De Wu. A sniv–porphyrin-based metal–organic framework for the selective photo-oxygenation of phenol and sulfides. *Inorganic chemistry*, 50(12):5318–5320, 2011.

- [136] Omar K Farha, Abraham M Shultz, Amy A Sarjeant, SonBinh T Nguyen, and Joseph T Hupp. Active-site-accessible, porphyrinic metal-organic framework materials. *Journal of the American Chemical Society*, 133(15):5652–5655, 2011.
- [137] NV Maksimchuk, MN Timofeeva, MS Melgunov, AN Shmakov, Yu A Chesalov, DN Dybtsev, VP Fedin, and OA Kholdeeva. Heterogeneous selective oxidation catalysts based on coordination polymer mil-101 and transition metal-substituted polyoxometalates. *Journal of Catalysis*, 257(2):315–323, 2008.
- [138] Steven S Kaye, Anne Dailly, Omar M Yaghi, and Jeffrey R Long. Impact of preparation and handling on the hydrogen storage properties of  $\text{Zn}_4\text{O}(\text{1,4-benzenedicarboxylate})_3$  (mof-5). *Journal of the American Chemical Society*, 129(46):14176–14177, 2007.
- [139] Jeffery A Greathouse and Mark D Allendorf. The interaction of water with mof-5 simulated by molecular dynamics. *Journal of the American Chemical Society*, 128(33):10678–10679, 2006.
- [140] Holger Baer, Massimo Bergamo, Anna Forlin, Lynn H Pottenger, and Joerg Lindner. Propylene oxide. *Ullmann's Encyclopedia of Industrial Chemistry*, 1993.
- [141] T Punniyamurthy, Subbarayan Velusamy, and Javed Iqbal. Recent advances in transition metal catalyzed oxidation of organic substrates with molecular oxygen. *Chemical reviews*, 105(6):2329–2364, 2005.
- [142] Karen Leus, Gauthier Vanhaelewyn, Thomas Bogaerts, Ying-Ya Liu, Dolores Esquivel, Freddy Callens, Guy B Marin, Veronique Van Speybroeck, Henk Vrielinck, and Pascal Van Der Voort. Ti-functionalized  $\text{nh}_2$   $\text{sub}_2$ /mil-47: An effective and stable epoxidation catalyst. *Catalysis Today*, 208:97–105, 2013.
- [143] Shirley Nakagaki, Gabriel Kaetan Baio Ferreira, Geani Maria Ucoski, and Kelly Aparecida Dias de Freitas Castro. Chemical reactions catalyzed by metalloporphyrin-based metal-organic frameworks. *Molecules*, 18(6):7279–7308, 2013.
- [144] Xiu-Li Yang and Chuan-De Wu. Metalloporphyrinic framework containing multiple pores for highly efficient and selective epoxidation. *Inorganic chemistry*, 2014.
- [145] William Morris, Boris Voloskiy, Selcuk Demir, Felipe Gandara, Psaras L McGrier, Hiroyasu Furukawa, Duilio Cascio, J Fraser Stoddart, and Omar M

- Yaghi. Synthesis, structure, and metalation of two new highly porous zirconium metal-organic frameworks. *Inorganic chemistry*, 51(12):6443–6445, 2012.
- [146] Xian-Tai Zhou, Hong-Bing Ji, Jian-Chang Xu, Li-Xia Pei, Le-Fu Wang, and Xing-Dong Yao. Enzymatic-like mediated olefins epoxidation by molecular oxygen under mild conditions. *Tetrahedron letters*, 48(15):2691–2695, 2007.
- [147] James A Bond and Hermann M Bolt. Review of the toxicology of styrene. *CRC critical reviews in toxicology*, 19(3):227–249, 1989.
- [148] S Ted Oyama. *Mechanisms in homogeneous and heterogeneous epoxidation catalysis*, volume 45. Elsevier, 2011.
- [149] James P Collman, John I Brauman, Bernard Meunier, Teruyuki Hayashi, Thomas Kodadek, and Scott A Raybuck. Epoxidation of olefins by cytochrome p-450 model compounds: kinetics and stereochemistry of oxygen atom transfer and origin of shape selectivity. *Journal of the American Chemical Society*, 107(7):2000–2005, 1985.
- [150] Ramesh D Arasasingham, Gong Xin He, and Thomas C Bruice. Mechanism of manganese porphyrin-catalyzed oxidation of alkenes. role of manganese (iv)-oxo species. *Journal of the American Chemical Society*, 115(18):7985–7991, 1993.
- [151] Robert W Lee, Paul C Nakagaki, PN Balasubramanian, and Thomas C Bruice. Observations and comments on the mechanism of epoxidation of alkenes by manganese (iii) porphyrins with hypochlorite. *Proceedings of the National Academy of Sciences*, 85(3):641–644, 1988.
- [152] Flávio Luiz Benedito, Shirley Nakagaki, Adelir A Saczk, Patricio Guillermo Peralta-Zamora, and Creuza Maieru Macedo Costa. Study of metalloporphyrin covalently bound to silica as catalyst in the *ortho*/*para*-dianisidine oxidation. *Applied Catalysis A: General*, 250(1):1–11, 2003.
- [153] Michael J Cowley, Ralph W Adams, Kevin D Atkinson, Martin CR Cockett, Simon B Duckett, Gary GR Green, Joost AB Lohman, Rainer Kerssebaum, David Kilgour, and Ryan E Mewis. Iridium  $\eta$ -heterocyclic carbene complexes as efficient catalysts for magnetization transfer from para-hydrogen. *Journal of the American Chemical Society*, 133(16):6134–6137, 2011.
- [154] Ralph W Adams, Juan A Aguilar, Kevin D Atkinson, Michael J Cowley, Paul IP Elliott, Simon B Duckett, Gary GR Green, Iman G Khazal, Joaquín López-Serrano, and David C Williamson. Reversible interactions with para-hydrogen enhance nmr sensitivity by polarization transfer. *Science*, 323(5922):1708–1711, 2009.

- [155] Johannes Natterer and Joachim Bargon. Parahydrogen induced polarization. *Progress in Nuclear Magnetic Resonance Spectroscopy*, 31(4):293–315, 1997.
- [156] Douglas T Genna, Antek G Wong-Foy, Adam J Matzger, and Melanie S Sanford. Heterogenization of homogeneous catalysts in metal–organic frameworks via cation exchange. *Journal of the American Chemical Society*, 135(29):10586–10589, 2013.
- [157] Hao Wang, Jian Xu, Da-Shuai Zhang, Qiang Chen, Rong-Mei Wen, Ze Chang, and Xian-He Bu. Crystalline capsules: Metal–organic frameworks locked by size-matching ligand bolts. *Angewandte Chemie International Edition*, 2015.
- [158] Kounosuke Oisaki, Qiaowei Li, Hiroyasu Furukawa, Alexander U Czaja, and Omar M Yaghi. A metal- organic framework with covalently bound organometallic complexes. *Journal of the American Chemical Society*, 132(27):9262–9264, 2010.
- [159] Robert Crabtree. Iridium compounds in catalysis. *Accounts of Chemical Research*, 12(9):331–337, 1979.
- [160] Teng Zhang and Wenbin Lin. Metal–organic frameworks for artificial photosynthesis and photocatalysis. *Chemical Society Reviews*, 43(16):5982–5993, 2014.
- [161] Mercedes Pintado-Sierra, Antonia M Rasero-Almansa, Avelino Corma, Marta Iglesias, and Félix Sánchez. Bifunctional iridium-(2-aminoterephthalate)–zr-mof chemoselective catalyst for the synthesis of secondary amines by one-pot three-step cascade reaction. *Journal of Catalysis*, 299:137–145, 2013.
- [162] Zheng Ni, Abderrahim Yassar, Tarek Antoun, and Omar M Yaghi. Porous metal-organic truncated octahedron constructed from paddle-wheel squares and terthiophene links. *Journal of the American Chemical Society*, 127(37):12752–12753, 2005.
- [163] Omar K Farha, A Özgür Yazaydın, Ibrahim Eryazici, Christos D Malliakas, Brad G Hauser, Mercouri G Kanatzidis, SonBinh T Nguyen, Randall Q Snurr, and Joseph T Hupp. De novo synthesis of a metal–organic framework material featuring ultrahigh surface area and gas storage capacities. *Nature chemistry*, 2(11):944–948, 2010.
- [164] Anusorn Seubsai, Michael Kahn, and Selim Senkan. New catalytic materials for the direct epoxidation of propylene by molecular oxygen. *ChemCatChem*, 3(1):174–179, 2011.

- [165] Isik Onal, Derya Düzenli, Anusorn Seubsai, Michael Kahn, Erol Seker, and Selim Senkan. Propylene epoxidation: High-throughput screening of supported metal catalysts combinatorially prepared by rapid sol-gel method. *Topics in Catalysis*, 53(1-2):92–99, 2010.
- [166] Karl Petter Lillerud, Unni Olsbye, and Mats Tilset. Designing heterogeneous catalysts by incorporating enzyme-like functionalities into mofs. *Topics in Catalysis*, 53(13-14):859–868, 2010.
- [167] Norbert Stock and Shyam Biswas. Synthesis of metal-organic frameworks (mofs): routes to various mof topologies, morphologies, and composites. *Chemical reviews*, 112(2):933–969, 2011.
- [168] Eric D Bloch, David Britt, Chain Lee, Christian J Doonan, Fernando J Uribe-Romo, Hiroyasu Furukawa, Jeffrey R Long, and Omar M Yaghi. Metal insertion in a microporous metal-organic framework lined with 2, 2'-bipyridine. *Journal of the American Chemical Society*, 132(41):14382–14384, 2010.
- [169] Yun Wu, Ling-Guang Qiu, Wei Wang, Zong-Qun Li, Tao Xu, Zhen-Yu Wu, and Xia Jiang. Kinetics of oxidation of hydroquinone to p-benzoquinone catalyzed by microporous metal-organic frameworks m3 (btc) 2 [m= copper (ii), cobalt (ii), or nickel (ii); btc= benzene-1, 3, 5-tricarboxylate] using molecular oxygen. *Transition metal chemistry*, 34(3):263–268, 2009.
- [170] Stephen S-Y Chui, Samuel M-F Lo, Jonathan PH Charmant, A Guy Orpen, and Ian D Williams. A chemically functionalizable nanoporous material [cu3 (tma) 2 (h2o) 3] n. *Science*, 283(5405):1148–1150, 1999.
- [171] T Grant Glover, Gregory W Peterson, Bryan J Schindler, David Britt, and Omar Yaghi. Mof-74 building unit has a direct impact on toxic gas adsorption. *Chemical Engineering Science*, 66(2):163–170, 2011.
- [172] U Mueller, M Schubert, F Teich, H Puetter, K Schierle-Arndt, and J Pastre. Metal-organic frameworks prospective industrial applications. *Journal of Materials Chemistry*, 16(7):626–636, 2006.
- [173] Renganathan Srirambalaji, Soonsang Hong, Ramalingam Natarajan, Minyoung Yoon, Raghunandan Hota, Yonghwi Kim, Young Ho Ko, and Kimoon Kim. Tandem catalysis with a bifunctional site-isolated lewis acid-brønsted base metal-organic framework, nh 2-mil-101 (al). *Chemical Communications*, 48(95):11650–11652, 2012.
- [174] Jinhee Park, Jian-Rong Li, Ying-Pin Chen, Jiamei Yu, Andrey A Yakovenko, Zhiyong U Wang, Lin-Bing Sun, Perla B Balbuena, and Hong-Cai Zhou. A versatile metal-organic framework for carbon dioxide capture

- and cooperative catalysis. *Chemical Communications*, 48(80):9995–9997, 2012.
- [175] Daniel E Koshland. The key–lock theory and the induced fit theory. *Angewandte Chemie International Edition in English*, 33(23-24):2375–2378, 1995.
- [176] Alle Bruggink, Rob Schoevaart, and Tom Kieboom. Concepts of nature in organic synthesis: cascade catalysis and multistep conversions in concert. *Organic process research & development*, 7(5):622–640, 2003.
- [177] Yong Huang, Abbas M Walji, Catharine H Larsen, and David WC MacMillan. Enantioselective organo-cascade catalysis. *Journal of the American Chemical Society*, 127(43):15051–15053, 2005.
- [178] Noritaka Mizuno and Makoto Misono. Heterogeneous catalysis. *Chemical Reviews*, 98(1):199–218, 1998.
- [179] Hiroyasu Furukawa, Ulrich Müller, and Omar M Yaghi. heterogeneity within order in metal–organic frameworks. *Angewandte Chemie International Edition*, 2015.